

University of Southampton Research Repository

Copyright © and Moral Rights for this thesis and, where applicable, any accompanying data are retained by the author and/or other copyright owners. A copy can be downloaded for personal non-commercial research or study, without prior permission or charge. This thesis and the accompanying data cannot be reproduced or quoted extensively from without first obtaining permission in writing from the copyright holder/s. The content of the thesis and accompanying research data (where applicable) must not be changed in any way or sold commercially in any format or medium without the formal permission of the copyright holder/s.

When referring to this thesis and any accompanying data, full bibliographic details must be given, e.g.

Thesis: Chuang Sun (2024) "All-dielectric metasurface for optical manipulation and advanced imaging application ", University of Southampton, School of Electronics & Computer Science, PhD Thesis, pagination.

University of Southampton

Faculty of Engineering and Physical Sciences

School of Electronics and Computer Science

All-dielectric metasurface for optical manipulation and advanced imaging application

by

Chuang Sun

ORCID ID 0000-0001-7024-1916

Thesis for the degree of Doctor of Philosophy

August 2024

University of Southampton

Abstract

Faculty of Engineering and Physical Sciences
School of Electronics and Computer Science

Doctor of Philosophy

All-dielectric metasurface for optical manipulation and advanced imaging application

by

Chuang Sun

Metasurface which is made up of an array of sub-wavelength meta-atoms on a flat substrate is powerful of engineering light beam's amplitude, phase, polarization, and frequency. It attracts increasing attentions in optical manipulation, communication, imaging, and metrology fields.

To boost the metasurface's applications in classical regime, the working principle, general design process, and fabrication flow of an all-dielectric metasurface are firstly studied in this thesis. Three working regimes of the metasurface are clearly classified. Except for the two conventional working regimes (polarization-independent regime and classical spin-multiplexing regime), a non-classical spin-multiplexing regime is explored to achieve multifunctional imaging system via a low refraction index metalens.

In polarization-independent working regime, a near infrared (NIR) metalens is achieved to levitate and trap a nanorod in a vacuum. In experiment, both the translation and rotation motion of levitated nanorod can be precisely controlled by the laser beam's polarization and power as well as the vacuum pressure. To construct an optically coupled dynamics system, a NIR dual foci metalens is achieved in the classical spin-multiplexing working regime for levitating two particles. Experiment results illustrate that the two optical potential wells can be precisely tuned, and two nanoparticles can be stably levitated at a close distance. Based on above experimental results, the world first prototype of metalens-based levitated optomechanical sensor is invented.

In classical spin-multiplexing working regime, two dual-mode microscopes with a high magnification of 58X, a $600\mu\text{m} \times 800\mu\text{m}$ field of view (FOV), and a diffraction-limited resolution are obtained via a NIR metalens where the focal point can be tuned to vortex ring from a Gaussian spot. In addition, a unified design frame is proposed to polarization-controlled generate arbitrary vector vortex beams on a HOPS and a HyOPS. In the proof of concept experiment in NIR, non-focused and tightly focused 5th order HOPS beams are firstly demonstrated. Then, tightly focused 0-1-order and 0-2-order HyOPS beams are controlled generated to comparatively study the focusing property of integer-order and fractional-order vector vortex beams.

In non-classical spin-multiplexing working regime, it is the world first to achieve tri-foci metalens based on low-refraction-index material (i.e., Si_3N_4). An infinity-corrected microscope with three large magnifications and resolutions is firstly integrated into a centimetre-scale device via a longitudinal tri-foci Si_3N_4 metalens. Then, a compact simultaneously achiral and chiral microscope with a magnification of 53X is experimentally demonstrated to realize all-optics fast identification of biological and chemical sample's chirality via a lateral Si_3N_4 tri-foci metalens.

Table of Contents

Table of Contents	3
Table of Tables	7
Table of Figures	8
Research Thesis: Declaration of Authorship.....	12
Acknowledgements.....	13
Definitions and Abbreviations.....	15
Chapter 1 Introduction	17
1.1 Research background and motivation	17
1.2 Thesis structure	19
Chapter 2 Principle and design procedure	21
2.1 Phase delay principle	21
2.1.1 Propagation phase of meta-atoms	21
2.1.2 Geometric phase of meta-atoms.....	23
2.2 A general working mechanism.....	24
2.2.1 $\phi d = 0$, polarization-independent regime	25
2.2.2 $\phi d = \pi$, classical spin-multiplexing regime	25
2.2.3 $0 < \phi d < \pi$, non-classical spin-multiplexing regime.....	26
2.3 Design procedure	26
2.4 Conclusion.....	28
Chapter 3 High-NA metalens for optical levitation and rotation	29
3.1 Introduction of optical levitation system	29
3.2 Aberration-free and high-NA focusing.....	31
3.3 Fabrication and characterization.....	32
3.4 Optical levitation and rotation.....	34
3.5 Conclusion.....	37
Chapter 4 Tunable on-chip optical traps for levitating particles	38

Table of Contents

4.1	Introduction of optical traps array	38
4.2	Design of the metasurface sample	40
4.3	Metasurface preparation and characterization	43
4.4	Dual-traps and levitation	47
4.4.1	Trapping stiffness and potential well	47
4.4.2	Optical levitation experiment	48
4.5	Optical coupling dynamics.....	50
4.6	Conclusion.....	53
Chapter 5 Near-infrared metalens empowered dual-mode microscope.		55
5.1	Introduction of dual-mode imaging.....	55
5.2	Metalens design and characterization	57
5.3	Compact dual-mode imaging experiments	59
5.3.1	High-resolution and large magnification microscope	59
5.3.2	Diffraction-limited resolution and large FOV microscope	60
5.3.3	Singlet dual-mode microscope for all-optical edge-detection	61
5.4	Conclusion.....	62
Chapter 6 Metasurface for arbitrary HOPS and HyOPS beams		64
6.1	Introduction of HOPS and HyOPS beams	64
6.2	General design frame	67
6.3	Manipulation of ongoing optical field	68
6.4	Proof-of-concept experiments	70
6.4.1	Non-focused 5 th -order HOPS beams.....	70
6.4.2	Tightly-focused 5 th -order HOPS beams	72
6.4.3	Tightly-focused 0-2 order HyOPS beams	73
6.4.4	Tightly-focused 0-1 order HyOPS beams	75
6.5	Conclusion.....	77
Chapter 7 Longitudinal tri-foci metalens for integrated microscope		78
7.1	Introduction	78

Table of Contents

7.2 Desing of longitudinal tri-foci metalens	79
7.3 t-MS characterization	81
7.4 Compact imaging experiment	82
7.4.1 Combining with Nikon microscope	82
7.4.2 Integrated tri-magnification microscope	83
7.5 Design of <i>q</i>-MS and fabrication.....	85
7.6 Conclusion.....	86
Chapter 8 Simultaneously chiral and achiral microscope.....	88
8.1 Introduction	88
8.2 Metalens design and characterization	89
8.3 Demonstration of tri-channel microscope	92
8.3.1 Simultaneously achiral and chiral imaging	92
8.3.2 All-optics chirality identification of chemical sample.....	95
8.4 Conclusion.....	96
Chapter 9 Hybrid calculation model and prototype of LOMS.....	97
9.1 Hybrid calculation model.....	97
9.1.1 Introduction.....	97
9.1.2 Hybrid FDTD and DDA method	97
9.1.3 Accuracy validation.....	100
9.2 Invention of a metalens-based LOMS prototype	100
9.2.1 Introduction.....	100
9.2.2 Details on the prototype	101
9.2.3 Demonstration of generating arbitrary optical field	106
9.3 Conclusion.....	107
Chapter 10 Summary and outlook.....	108
10.1 Summary	108
10.2 Outlook.....	110
10.2.1 Working efficiency vs high NA and broadband achromatic	110

Table of Contents

10.2.2 Inverse design of metasurface	111
10.2.3 Large aperture metasurface.....	112
10.2.4 Mass production for commercialization.....	112
10.2.5 Monolithic integration for structured illumination and manipulation	113
Appendix A Dielectric material selection	114
Appendix B Fabrication details and notes.....	116
B.1 Temperature's influence on PECVD a-Si	116
B.2 Optical property of PECVD Si₃N₄.....	116
B.3 RIE parameters for Si₃N₄	116
B.4 E-spacer's influence on EBL.....	117
Appendix C Working mechanism in linear polarization basis.	118
Glossary of Terms	120
List of References	121

Table of Tables

Table 5.1 Nanofins library for dual mode focusing metalens.....	57
Table 6.1 Parameters and target of metasurface samples.....	70

Table of Figures

Figure 2.1 Metasurface and meta-atom.....	21
Figure 2.2 Meta-atom's library for the NIR a-Si metalens.....	22
Figure 2.3 Designing procedure of a metasurface.	27
Figure 3.1 A typical optical levitation system [77].....	30
Figure 3.2 Optical trapping configurations for optical levitation system [78].....	30
Figure 3.3 Metalens for optical levitation experiment.	31
Figure 3.4 Fabrication flow of the a-Si metalens.....	32
Figure 3.5 Optical configuration for characterizing a-Si metalens samples.	33
Figure 3.6 Optical configuration of the metalens-based optical levitation system.	34
Figure 3.7 COM motions of levitated nanorod.	35
Figure 3.8 Rotation dynamics of levitated nanorod.....	36
Figure 4.1 Conceptual figure of the on-chip optical levitation system.	39
Figure 4.2 (a) Geometrical parameters of two focal points; (b) Nanofins library; (c) SEM..	40
Figure 4.3 Simulated focal points and potential wells.	42
Figure 4.4 Characterization of the metasurface sample.	43
Figure 4.5 Optical intensity and potential wells of the metalens sample 1.....	44
Figure 4.6 Optical intensity and potential wells of the metalens sample 2.....	45
Figure 4.7 Polarization state over the fundamental Poincaré sphere.	46
Figure 4.8 Simulated trapping stiffness and force.	47
Figure 4.9 Optical levitation of two nanoparticles.	49
Figure 4.10 Optical coupling model and dynamics.....	51
Figure 5.1 Conceptual figure of dual-mode imaging.	56
Figure 5.2 Characterization of metalens samples.	58

Table of Figures

Figure 5.3 Imaging results of 58X microscope.....	59
Figure 5.4 Resolution test of infinity-corrected microscope.....	60
Figure 5.5 Imaging results of biological sample.....	61
Figure 5.6 All-optics edge-detection experiment and results.	62
Figure 6.1 Conceptual figure of HOPS and HyOPS.	64
Figure 6.2 Proposed general design frame.	67
Figure 6.3 Manipulating ongoing optical field over a HOPS and HyOPS.	68
Figure 6.4 Experimental results: non-focused 5 th -order HOPS beams.	71
Figure 6.5 Experiment results: tightly focused 5 th -order HOPS beams.....	73
Figure 6.6 Simulation results: tightly focused 0-2-order HyOPS beams.....	74
Figure 6.7 Experiment results: tightly focused 0-2-order HyOPS beams.....	75
Figure 6.8 Simulation results: tightly focused 0-1-order HyOPS beams.....	75
Figure 6.9 Experiment results: tightly focused 0-1-order HyOPS beams.....	76
Figure 7.1 Conceptual figure of integrated microscope with three magnifications.....	78
Figure 7.2 Design and optical characterization of the metalens sample.....	79
Figure 7.3 Cell library for Si ₃ N ₄ metalens in chapters 7 and 8.	80
Figure 7.4 Optical configuration for measuring Si ₃ N ₄ metalens samples.	81
Figure 7.5 Singlet imaging for extending Nikon microscope.	82
Figure 7.6 Experiment on integrated tri-magnification microscope.	84
Figure 7.7 (a) meta-atom library for q-MS; (b) Index of PECVD Si ₃ N ₄	86
Figure 7.8 Fabrication flow of Si ₃ N ₄ metalens.....	86
Figure 8.1 Conceptual figure of simultaneously achiral and chiral imaging.	89
Figure 8.2 Working (a) and results (b - d) of tri-channel metalens.....	90
Figure 8.3 Phase profiles for tri-channel metalens.	91
Figure 8.4 Focusing process of the LCP (a), achiral (b), and RCP (c) channels.	92

Table of Figures

Figure 8.5 Simultaneously achiral and chiral microscope.....	93
Figure 8.6 Imaging results of the microscope shown in Figure 8.5.....	94
Figure 8.7 All-optics chirality identification of liquid crystal sample.....	95
Figure 9.1 Schematic illustrating of a metalens-based LOMS.	98
Figure 9.2 Optical torques vs $\text{Im}(\varepsilon_s)$ calculated by Mie-theory and the HFDM.....	100
Figure 9.3 Prototype of the LOMS based on a dry particle launching method.....	102
Figure 9.4 External components of the LOMS.	103
Figure 9.5 Prototype of the LOMS based on LIAD method.....	104
Figure 9.6 Design flow of a metasurface for generating arbitrary optical field.	105
Figure 9.7 Space-multiplexing metasurface for generating arbitrary optical field.....	106
Figure 9.8 X-shaped meta-atoms for arbitrary optical field.	106
Figure 9.9 Demonstration of generating arbitrary optical field.....	107

Table of Figures

Research Thesis: Declaration of Authorship

Print name: Chuang Sun

Title of thesis: All-dielectric metasurface for optical manipulation and advanced imaging application

I declare that this thesis and the work presented in it are my own and has been generated by me as the result of my own original research.

I confirm that:

1. This work was done wholly or mainly while in candidature for a research degree at this University;
2. Where any part of this thesis has previously been submitted for a degree or any other qualification at this University or any other institution, this has been clearly stated;
3. Where I have consulted the published work of others, this is always clearly attributed;
4. Where I have quoted from the work of others, the source is always given. With the exception of such quotations, this thesis is entirely my own work;
5. I have acknowledged all main sources of help;
6. Where the thesis is based on work done by myself jointly with others, I have made clear exactly what was done by others and what I have contributed myself;
7. Parts of this work have been published as:

[1] Sun, Chuang, and Jize Yan. "A hybrid method to calculate optical torque: Application to a nano-dumbbell trapped by a metalens." *AIP Advances* 12.7 (2022).

[2] Sun, Chuang, et al. "Tunable on-chip optical traps for levitating particles based on single-layer metasurface." *Nanophotonics* 13.15 (2024).

[3] Sun, Chuang, et al. "Near-Infrared Metalens Empowered Dual-Mode High Resolution and Large FOV Microscope." *Advanced Optical Materials* 12.21 (2024): 2400512.

[4] Sun, Chuang, et al. "Field Sensor and Field Sensing Method." *patent filed* (2023).

8. Parts of this work are still under review of academic journals.

Signature: Date:.....

Acknowledgements

I am thrilled to write this acknowledgment as I reflect on the exceptional support I have received on this journey. First and foremost, I owe immense gratitude to three esteemed mentors: Prof. Jize Yan, Dr. Jun-Yu Ou, and Prof. Hendrik Ulbricht, as well as to our skilled fabrication technicians, Dr. Kian Shen Kiang, Libe Arzubiaga Totorika, and Anushka Gangnaik, each bringing a wealth of experience in cleanroom practices. Additionally, I am deeply appreciative of the camaraderie and support from many wonderful colleagues.

My foremost acknowledgment goes to my primary supervisor, Prof. Jize Yan. Prof. Yan's profound understanding of physics, mechanics, and optics across classical and quantum domains, coupled with his expansive scientific vision and sharp academic insight, have been instrumental in guiding my research. During our weekly meetings, Prof. Yan not only reviews my progress but also encourages deeper theoretical explorations behind numerical and experimental findings. For example, when confronted with the achievement of the tri-foci metalens in numerical simulations without a corresponding theoretical framework, Prof. Yan adeptly directed me to analyze the phenomena through the light propagation and energy conservation. This led to the discovery of the non-classical spin-multiplexing regime in my project, providing a conceptual framework for subsequent endeavors. Prof. Yan's guidance has been indispensable to my thesis, and his generous support of experimental components has been crucial to achieving reliable results. I am deeply grateful for his mentorship and assistance over the past 42 months.

I also extend my heartfelt appreciation to Dr. Jun-Yu Ou and Prof. Hendrik Ulbricht, who provided access to the research lab and imparted invaluable experimental skills. Dr. Ou's exacting standards for group meeting presentations and slide formats have not only enhanced my presentation abilities but also improved the quality of my figures. His meticulous approach to experiments and papers has inspired me to pay closer attention to detail. Though not my official supervisor, Dr. Ou has been an invaluable mentor, and I acknowledge his influence with gratitude.

Furthermore, I express my gratitude to Dr. Kian Shen Kiang for his dedication to e-beam lithography, Dr. Libe Arzubiaga Totorika for developing deposition and dry etching recipes, and Dr. Anushka Gangnaik for her numerous acts of assistance in the cleanroom.

Beyond the academic realm, I must acknowledge the supportive colleagues within the research groups of Prof. Jize Yan and Prof. Hendrik Ulbricht, including Dr. Hailong Pi, Dr. Wangke Yu, Dr. Shumeng Wang, Dr. Christopher Timberlake, Dr. Tiberius-Stefan Georgescu, Zhicheng Shen, Weilin Jin, Zixuan Wang, and Jack Homans. Their unwavering support has been instrumental in helping me balance work and life commitments.

Acknowledgements

Finally, I am deeply indebted to my family. The challenges posed by the COVID-19 pandemic intensified the difficulties of my PhD research, restricting access to labs until mid-2022 and limiting experimental characterization opportunities until spring 2023. Throughout this period, my family provided steadfast companionship, encouragement, and support, enabling me to navigate these challenges and successfully complete my research.

Definitions and Abbreviations

SAM	Spin angular momentum
OAM	Orbital angular momentum
LCP	Left-handed circular polarization
RCP	Right-handed circular polarization
LP	Linear polarization
NA	Numerical aperture
NIR	Near infrared
CMOS	Complementary metal-oxide-semiconductor
FWHM	Full width of half maximum
QWP	Quarter waveplate
FOV	Field of view
FPS	Fundamental Poincaré sphere
HOPS	Higher order Poincaré sphere
HyOPS	Hybrid order Poincaré sphere
SOP	State of Polarization
COM	Centre of mass
PSD	Power spectra density
NMP	an organic solvent, N-Methyl-2-pyrrolidone
IPA	Isopropyl Alcohol
PECVD	Plasma-enhanced chemical vapor deposition
RIE	Reactive ion etching.
EBL	E-beam lithography
VVB	Vector vortex beam
CVVB	Cylindrical vector vortex beam
LCS	Liquid crystal sample
SLM	Spatial light modulator

Definitions and Abbreviations

AOD.....	Acoustic optics deflector
t-MS.....	Longitudinal tri-foci metalens
q-MS.....	Metalens with a quadratic phase profile

Chapter 1 Introduction

1.1 Research background and motivation

Since Capasso's group reported the abrupt phase change over wavelength-scale and the generalized Snell law in the year of 2011 [1], the research on metasurface have experienced explosive growth around the world because the metasurface's powerful engineering ability of electromagnetic wave's amplitude [2, 3] phase [4, 5], polarization [6, 7], and even frequency [[2, 8]. Comparing with plasmonic metasurface, all-dielectric metasurface is attracting intensive attention because it can avoid ohmic losses and realize higher working efficiency [9]. The working mechanism of an all-dielectric metasurface is based on resonance effects (e.g., Mie-resonance, Fano resonance, bound states in the continuum, et al.) or non-resonance effects (e.g., propagation phase, geometric phase, and their combination) [9-12]. The application of resonance-based metalens (i.e., a metasurface with a focusing phase profile) would be restricted by its narrow working bandwidth and the strong resonance coupling between adjacent meta-atoms [13]. In contrast, non-resonance metalens can work in a wide spectrum and work for tightly focusing with a high numerical aperture (NA). As a result, the metalens has a huge application potential in optical manipulation, laser communication, and optical imaging. Therefore, all metasurfaces studied in this thesis is based on non-resonance mechanism and all-dielectric material. In following, I'll directly use metasurface/metalens to denote the non-resonance and all-dielectric metasurface/metalens.

Optical tweezer as an effective tool of optical manipulation was awarded the Nobel physics prize in the year of 2018 because its wide applications in biological, chemistry, physical, and astronomy research as well as in nanotechnology and sensing field [14-17]. Conventionally, an optical tweezer is built by tightly focusing a laser beam via a high NA objective lens[18] or a reflective metal parabolic mirror [19], which leads the optical tweezer system to be bulky, difficult in alignment, not suitable for scale-up, and high cost. Benefiting from the development of metalens, a laser beam can be tightly and aberration-free focused into a tiny focal point with a high efficiency, which makes it possible to build an optical tweezer via a thin, lightweight, and flat element [20-22]. As a result, the optical tweezer system is simplified, miniaturized, and scaled up, which would contribute to the mass-production of optical levitation sensors. In the year of 2021, Tong Cang Li's group demonstrated the first metalens-based optical levitation system [23]. In a conventional optical levitation system, the levitated nanoparticle can be driven to spin at a speed of GHz by transferring the spin angular momentum (SAM) [24-26]. However, it has not been realized in a metalens-based optical levitation system. Therefore, the first research motivation of

this thesis is to build a metalens-based optical levitation system and achieve the fast spin of a levitated nanoparticle.

Moreover, optical levitation of multiple particles has become technically possible for studying particle-particle interactions such as optical, light-matter interactions, coupled dynamics, and mode-localization [27-31]. The ability to simultaneously trap and manipulate multiple particles or even an array of particles in a vacuum will be of vital importance [28, 32, 33]. Conventionally, there are two ways of trapping more than one particle at a time. The first way is using the standing wave generated by two counter-propagating beams [34, 35], and the other way is introducing a modulator [e.g., spatial light modulator (SLM), acoustic-optics deflector (AOD), digital micromirror device] to the optical levitation system [36, 37]. However, the overall efficiency of a SLM-based/AOD-based two optical traps would be only around 5%. In addition, limited by the modulation principle of a SLM and AOD, there would be continuous fluctuation in the intensity of the two focal point. Both the low efficiency and intensity fluctuation highly suppress the interactions between trapped particles. Therefore, the second research motivation of this thesis is to propose a compact metalens-based optical traps for levitating multi-particles with high efficiency and tunable potential wells.

It is known that the SAM transferred to optically levitated nanoparticle arises from the trapping laser beam's polarization state, and the orbital angular momentum (OAM) carried by the vortex beam arises from the laser beam's phase distribution [26, 38]. While the SAM can lead to a GHz spin of the levitated nanoparticle [24], the OAM can result in the orbital rotation of a trapped particle [39]. Therefore, it is important to generate vector vortex beams for providing more degree of freedom of optical manipulation [20, 22]. Generally, a vector vortex beam owns spatial-varied distribution in both polarization and phase, which could be used for multi-dimensional optical manipulations. In theory, a higher-order Poincaré sphere (HOPS) and hybrid-order Poincaré sphere (HyOPS) are developed to systematically describe arbitrary vector vortex beams [40, 41]. In engineering, some metasurfaces are demonstrated to generated vector vortex beams [4, 42-47]. However, there is not a general design frame of a metasurface to generate arbitrary non-focused/focused vector vortex beams on a HOPS and HyOPS, and the tightly focusing property of HyOPS beams is not systematically studied. Therefore, the third motivation of this thesis is to propose the general design and experimentally investigated the tightly focusing property of HyOPS beams. It should be figured out that the HOPS and HyOPS beams have huge potential applications in optical communication, manufacture, precision metrology, and imaging [22, 48-51].

As to the imaging application, the metalens could effectively reduce the volume and weight of a conventional imaging system (e.g., telescope, camera, and microscope), because multiple bulky

lens can be compressed into a single metalens without reducing the imaging quality at the designed wavelength [52, 53]. While it is still a world challenge to realize wide-spectrum and large-aperture achromatic imaging via a single metalens, metalens has demonstrated its advantages in monolithically multi-functional imaging applications [54-57]. For example, a metalens can be used for phase contrast imaging [58], polarization imaging [59], 3D depth imaging [60], and complex amplitude imaging [60]. However, many advanced imaging functions have not been realized via the metalens. Therefore, the fourth motivation of this thesis is to furtherly extend the functions of a metalens-based imaging system, to extend the imaging application scenarios, and boost the commercialization of meta-scope.

1.2 Thesis structure

Based on above research background and motivations, this thesis is organized as follows.

Chapter 2 summarizes the commonly adopted phase modulation principle, derives the realization conditions of three working mechanisms, and demonstrates a general design procedure of an all-dielectric metalens. Importantly, the inherent coherence of the four research motivations is pointed out through analyzing the three working mechanisms.

In chapter 3, a single-foci metalens with a high NA (0.91) and high working efficiency (31%) is firstly designed, fabricated, and characterized in experiment. Then, an optical levitation experiment system where the light beam is tightly focused by the metalens is operated for optically levitating a nanoparticle and realizing fast spin of the particle in a vacuum.

In chapter 4, a laterally dual-foci metalens is demonstrated in both simulation and experiment to realize a on-chip tunable optical traps for levitating two nanoparticles at a close distance. Then, an optical levitation experiment of two nanoparticles is operated and demonstrated. At the last of this chapter, a theoretical analysis of optical trapping force, binding force, trapping stiffness, as well as the dynamics of two levitated particles is done to show the potential applications of the proposed dual-foci metalens-based optical levitation platform.

Chapter 5 demonstrates a near-infrared (NIR) metalens empowered dual-mode high resolution and large field of view (FOV) microscope. To realize the dual-mode microscope, a NIR metalens with polarization-controlled and high-NA focal point is designed, fabricated, and measured in experiment.

In chapter 6, to generate arbitrary non-focused/focused vector vortex beams on a HOPS or HyOPS via an all-dielectric metasurface, a general design frame of the metasurface is proposed at first. Then, four metasurface surfaces are designed, fabricated, and characterized to show the

Chapter 1

validation of the proposed design frame and to study the tightly focusing property of the HyOPS beams.

Chapter 7 proposes a longitudinal tri-foci metalens via the low-refraction-index material Si₃N₄. Then, the metalens sample is introduced to a commercial microscope to realize three magnifications and resolutions via a single objective lens. Finally, a fully integrated microscope with three magnifications and resolutions is built based on the metalens sample.

Following a similar working principle of the metalens demonstrated in chapter 7, chapter 8 demonstrates a lateral tri-foci Si₃N₄ metalens and builds a diffraction-limited microscope for simultaneously chiral and achiral imaging.

In chapter 9, a numerical simulation model is proposed to calculate the optical forces and torques exerted on an aspherical particle levitated by a complexing optical field. Then, the prototype of metalens-based levitated optomechanics system (LOMS) is invented for boost the commercialization of optical levitation sensor.

Finally, all work in this thesis is summarized in chapter 10 where some prospectives for the future work are proposed in five directions.

Chapter 2 Principle and design procedure

2.1 Phase delay principle

As shown in Figure 2.1(a), the metasurface is made up of an array of periodically placed meta-atoms on a flat silica substrate. The meta-atoms in a dielectric metasurface generally have a subwavelength-scale. The phase modulation ability of a metasurface is achieved by the local phase delay induced by each meta-atom. The local phase delay could arise from the resonance phase [61], propagation phase, and geometric phase (i.e., the PB phase) [4].

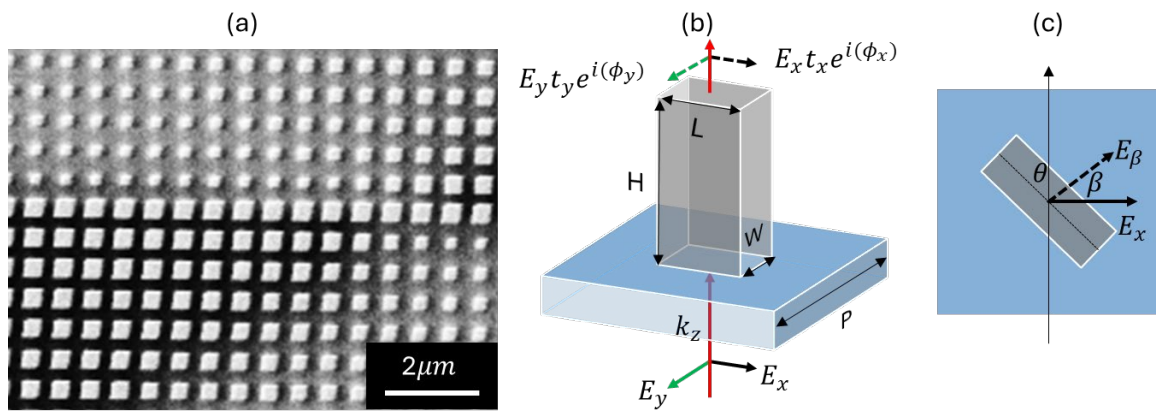


Figure 2.1 Metasurface and meta-atom.

(a) SEM image of a fabricated metasurface sample, (b) and (c) scheme of subwavelength meta-atom with a rectangle cross section.

When the dielectric meta-atoms have a height (H) much smaller than working wavelength (λ), metasurface's phase manipulation is achieved based on resonance phase, like the Mie resonance, FP resonance, Fano resonance, and BIC [62, 63]. However, metasurfaces based on resonance phase can only work in a narrow bandwidth [13]. Moreover, resonance-based metasurfaces cannot focus incoming light with a high numerical aperture (NA), because the resonance mode coupling between adjacent meta-atoms would lead to significant errors in the case of large phase gradients [13]. In following, the phase delay and working mechanism of non-resonance all-dielectric metasurface will be studied in detail.

2.1.1 Propagation phase of meta-atoms

The dielectric meta-atoms with a height H comparable to the working wavelength λ would introduce polarization-independent propagation phase and the polarization-dependent propagation phase. When the meta-atoms have a rotationally symmetrical cross-section (e.g.,

square, circle), the propagation phase is polarization independent. Otherwise, polarization-dependent propagation phase would be introduced.

As shown in Figure 2.1(b), the dielectric meta-atom can be treated as a truncated waveguide that has an effective refraction index n_{eff} . As the optical wave is confined inside the meta-atom, the propagation phase ϕ of the light wave propagating through the meta-atom can be defined as Eq. (2.1) [64],

$$\phi = \frac{2\pi}{\lambda} n_{eff} H \quad (2.1)$$

As the n_{eff} is determined by the meta-atom's structural parameters (e.g., period P , width W , length L , and height H), material properties (e.g., refraction index n), the propagation phase ϕ can be tailored by the varying the structural dimensions [Figure 2.2(a)] and material selection. 2π phase coverage is necessary to achieve effective focusing of light wave. To achieve 2π phase coverage between the meta-atoms with smallest dimensions and largest dimensions, the height H should meet Eq. (2.2) [9].

$$H > \frac{\lambda}{n-1} \quad (2.2)$$

As the larger H would lead to a higher aspect ratio of the meta-atoms and increase the fabrication difficulty, I'd like to select the material with larger refraction index n . The period P should be small enough to satisfy the Nyquist sampling criterion and reduce high order diffraction [Eq. (2.3)] for a target numerical aperture NA [65].

$$P < \frac{\lambda}{2*NA} \quad (2.3)$$

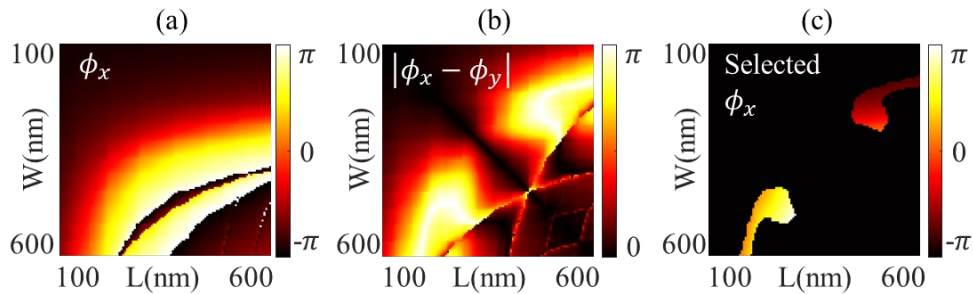


Figure 2.2 Meta-atom's library for the NIR a-Si metalens.

(a) Propagation phase ϕ_x varies with meta-atom's dimension, (b) Phase delay $|\phi_x - \phi_y|$ varies with meta-atom's dimension, (c) Selected meta-atoms library for achieving 2π phase coverage of ϕ_x and meeting the requirements of $|\phi_x - \phi_y| = \pi$ and $t_x = t_y = 1$. (Period = 650nm, Height = 800nm, wavelength = 1550nm)

Because the maximum filling factor, feature size, and highest aspect ratio of the meta-atoms are restricted by the fabrication ability, the fabrication of a large NA metalens is quite challenging. Because of the large refraction index ($n = 3.45$), low absorption ($k \approx 0$) at the wavelength of 1550nm, and mutual fabrication technique, the silicon is selected as the meta-atom material for the NIR metalens.

2.1.2 Geometric phase of meta-atoms

As shown in Figure 2.1(b) and Figure 2.2(b), there is a phase difference $|\phi_x - \phi_y|$ between the propagation phases induced to the X-polarized light beam and Y-polarised light beam when the cross-section is rectangle ($W \neq L$), because the X-polarized and Y-polarised light beams experience different structural dimensions. Therefore, the meta-atom works like a waveplate, and its function can be represented by a Jones matrix [66].

$$\begin{bmatrix} E_x^o \\ E_y^o \end{bmatrix} = \begin{bmatrix} \cos(\theta) & -\sin(\theta) \\ \sin(\theta) & \cos(\theta) \end{bmatrix} \begin{bmatrix} t_x e^{i\phi_x} & 0 \\ 0 & t_y e^{i\phi_y} \end{bmatrix} \begin{bmatrix} \cos(\theta) & \sin(\theta) \\ -\sin(\theta) & \cos(\theta) \end{bmatrix} \times \begin{bmatrix} E_x \\ E_y \end{bmatrix} \quad (2.4)$$

As Eq. (2.4) shown, the transmitted light can be directly obtained at each lattice. In Eq. (4), θ is the angle between the meta-atom's length side and Y-axe, t_x (t_y) and ϕ_x (ϕ_y) are the transmission and propagation phase of the X-polarized (Y-polarized) light beam for $\theta = 0$, respectively. By optimizing the meta-atom dimensions, both t_x and t_y can be meticulously crafted to achieve a unity (=1), and $|\phi_x - \phi_y| = \pi$. As a result, Equation (2.4) can be simplified to Eq. (2.5).

$$\begin{bmatrix} E_x^o \\ E_y^o \end{bmatrix} = e^{i\phi_x} \begin{bmatrix} \cos(2\theta) & \sin(2\theta) \\ \sin(2\theta) & -\cos(2\theta) \end{bmatrix} \times \begin{bmatrix} E_x \\ E_y \end{bmatrix} \quad (2.5)$$

When the incident light beam is left-handed circular polarization (LCP, $|L\rangle = \begin{bmatrix} 1 \\ i \end{bmatrix}$), the transmitted light beam can be obtained as Eq. (2.6), which means that the transmitted light beam is transferred to be right-handed circular polarization (RCP, $|R\rangle = \begin{bmatrix} 1 \\ -i \end{bmatrix}$) with a propagation phase of ϕ_x and a geometric phase of 2θ .

$$\begin{bmatrix} E_x^o \\ E_y^o \end{bmatrix} = i e^{i(\phi_x+2\theta)} |R\rangle \quad (2.6)$$

When the incident light beam is RCP (i.e., $\begin{bmatrix} E_x \\ E_y \end{bmatrix} = |R\rangle$), the transmitted light beam can be obtained as Eq. (2.7), which means that the transmitted light beam is transferred to be LCP with a propagation phase of ϕ_x and a geometric phase of -2θ .

$$\begin{bmatrix} E_x^o \\ E_y^o \end{bmatrix} = ie^{i(\phi_x - 2\theta)} |L\rangle \quad (2.7)$$

According to Eqs. (2.6) and (2.7), the geometric phase $\pm 2\theta$ imposed on incoming LCP and RCP light beam is opposite, therefore, the geometric phase is a polarization-dependent phase.

For a given meta-atom, the induced propagation phase ϕ_x is a constant value, which means that the phase carried by the transmitted light is only determined by the geometric phase $\pm 2\theta$. As shown in Figure 2.2(c), with keeping $|\phi_x - \phi_y| = \pi$ and $t_x = t_y = 1$, we can vary meta-atom's dimension (i.e., L and W in Figure 2.1) to realize 2π phase coverage of the propagation phase ϕ_x . Based on the selected meta-atom library [Figure 2.2 (c)], polarization-dependent geometric phase $\pm 2\theta$ and polarization-independent propagation phase ϕ_x can be simultaneously utilized for manipulating the phase of the transmitted light wave. Finally, a multi-functional spin-multiplexing metasurface can be designed.

2.2 A general working mechanism

While the geometric phase is achieved by using anisotropic meta-atoms, the propagation phase introduced by a meta-atom generally requires a wavelength-scale height and a material having high refraction index and low absorption index [9, 11]. Silicon is generally used in NIR and short-wavelength mid-infrared spectrum, the TiO_2 , GaN , and Si_3N_4 are widely used in visible spectrum [67]. Comparing with CMOS-compatible fabrication process of Si_3N_4 metalens, the fabrication of TiO_2 and GaN metalens is not compatible with CMOS process and require a complex process of low-temperature atomic layer deposition and high aspect ratio two-step dry etching [11]. However, the refraction index of Si_3N_4 is around 2 and smaller than that (~ 2.4) of TiO_2 and GaN , which would lead to a high aspect ratio for achieving 2π phase coverage and to higher fabrication difficulty. More details on selecting material can be found in Appendix A. As a result, multi-functional imaging applications of a Si_3N_4 metalens is restricted. Because the low-cost and CMOS-compatible fabrication process are two key factors of boosting the industrial applications of dielectric metalens, it is meaningful to explore the potential of a Si_3N_4 metalens for advanced multi-functional imaging applications. To achieve multi-functional imaging applications of Si_3N_4 metalens (i.e., low refraction metalens), a more general working mechanism of a metasurface is thoroughly studied in this section [68].

$$|E_o\rangle = \sqrt{\eta_i} e^{i(\phi_p)} |E_i\rangle + \sqrt{\eta_L} e^{i(\phi_p - 2\theta)} |L\rangle + \sqrt{\eta_R} e^{i(\phi_p + 2\theta)} |R\rangle \quad (2.8)$$

It is believed that the ongoing light $|E_o\rangle$ of a truncated waveguide meta-atom has three polarization terms [Eq. (2.8)] [68]. The first term $|E_i\rangle$ has an identical polarization of the incident light beam, and the second and third terms denote the left-circularly polarized and right-circularly

polarized light. In Eq. (2.8), the $\eta_i = \left| \frac{1}{2}(t_x + t_y e^{i\phi_d}) \right|^2$, $\eta_L = \left| \frac{1}{2}(t_x - t_y e^{i\phi_d}) \langle R | E_i \rangle \right|^2$, $\eta_R = \left| \frac{1}{2}(t_x - t_y e^{i\phi_d}) \langle L | E_i \rangle \right|^2$ are the efficiency coupled to each polarization term, and phase delay $\phi_d = |\phi_y - \phi_x|$. Generally, the t_x and t_y can be optimized to be higher than 90% by designing the height and period of the meta-atom. As a result, the three efficiencies are dependent on the phase delay $\eta_i = \left| \frac{1}{2}(1 + e^{i\phi_d}) \right|^2$, $\eta_L = \left| \frac{1}{2}(1 - e^{i\phi_d}) \langle R | E_i \rangle \right|^2$, $\eta_R = \left| \frac{1}{2}(1 - e^{i\phi_d}) \langle L | E_i \rangle \right|^2$. In following, three special regimes would be investigated.

2.2.1 $\phi_d = 0$, polarization-independent regime

For a symmetrical meta-atom, we can realize $\phi_y = \phi_x$ and $\phi_d = 0$. As a result, $\eta_i = \left| \frac{1}{2}(1 + e^{i\phi_d}) \right|^2 = 1$, and $\eta_L = \eta_R = 0$, which indicates that the ongoing light beam is fully coupled into a polarization-independent term and imposed a phase profile of $\phi_p = \frac{\varphi_y + \varphi_x}{2} = \varphi_x$. This means that the metasurface/metalens based on symmetrical meta-atoms only has one modulation channel. As a result, the metalens can only have one polarization-independent focal point [64]. In this regime, to build up an optical levitation system and achieve high-speed spin of the levitated particle, a single-foci metalens with a high NA of 0.91 and high efficiency of 31% is demonstrated in chapter 3.

2.2.2 $\phi_d = \pi$, classical spin-multiplexing regime

Conventionally, all researchers committed to achieving a phase difference $\phi_d = \pi$ via an anisotropic meta-atom. As a result, $\eta_i = 0$, $\eta_L = \langle R | E_i \rangle$, and $\eta_R = \langle L | E_i \rangle$, which indicates that ongoing light beam is coupled to the polarization-dependent $|L\rangle/|R\rangle$ channels and the phase profile carried by the ongoing light beam relies on the polarization of incident light beam. Specifically, when the incident light beam is $|L\rangle$, $\eta_L = 0$, $\eta_R = 1$, the ongoing light beam would be $|R\rangle$ and has a phase profile of $2\theta + \phi_p$. In contrast, when the incident light beam is $|R\rangle$, $\eta_L = 1$, $\eta_R = 0$, the ongoing light beam would be $|L\rangle$ and has a phase profile of $-2\theta + \phi_p$. When the incident light beam is non-perfect circular polarized, the $|R\rangle$ and $|L\rangle$ orthogonal components would be respectively imposed the phase profile of $2\theta + \phi_p$ and $-2\theta + \phi_p$. If we can build a meta-atom library where each cell has a ϕ_d of π and the propagation phase ϕ_p can realize 2π phase coverage, arbitrary phase profiles can be separately achieved by $2\theta + \phi_p$ and $-2\theta + \phi_p$. Therefore, a polarization-dependent dual-functional metasurface/metalens can be built. As the circular polarization state of a laser beam is corresponding to the SAM, the polarization-dependent dual-functional metasurface/metalens is also named spin-multiplexing metasurface/metalens [69, 70]. Because this is a classical and widely-adopted polarization-

dependent mechanism in designing metasurface, I'd like to call this regime as a classical spin-multiplexing regime.

Based on the classical spin-multiplexing phase, a lateral dual-foci metalens is firstly demonstrated in chapter 4 to build up an on-chip tunable optical levitation system for simultaneously trapping two particles at a close distance. Then, a metalens with polarization-controlled focal field is demonstrated in chapter 5 to build up a dual-mode imaging system. Finally, in chapter 6, a general design frame of a spin-multiplexing metasurface is proposed to generate arbitrary non-focused/focused HOPS and HyOPS beams via a single-layer metasurface.

However, because of the low refraction index and fabrication limitation on aspect ratio, the required library cannot be built up via the low refraction index material (e.g., Si_3N_4). Therefore, it is necessary to release the requirement on building up a library for multi-channel metasurface.

2.2.3 $0 < \phi_d < \pi$, non-classical spin-multiplexing regime

When the ϕ_d is not equal to zero and π , three efficiencies η_i , η_L , and η_R are not equal to zero. It means that the ongoing light beam would be coupled to three channels $|E_i\rangle$, $|L\rangle$ and $|R\rangle$ when the incident light beam is not perfect LCP and RCP. Each channel can be imposed three phase profiles of ϕ_p , $2\theta + \phi_p$, and $-2\theta + \phi_p$, respectively. It is obviously that, we can realize two arbitrary phase profiles once building up a library where the propagation phase ϕ_p have 2π coverage and the phase difference ϕ_d of each meta-atom is identical. As the requirement on the phase difference ϕ_d is reduced to arbitrary non-zero and non- π value, the low refraction index material (e.g., Si_3N_4) can be used for building up a meta-atom library. Because this working mechanism is not experimentally explored previously around the world, I call it as a non-classical spin-multiplexing regime. Based on this non-classical spin-multiplexing regime, a longitudinal and lateral tri-foci Si_3N_4 metalens is experimentally achieved in chapters 7 and 8, respectively. Based on the two Si_3N_4 metalens samples, a fully integrated microscope with three magnifications and resolutions is demonstrated in chapter 7, and chapter 8 demonstrates a tri-channel microscope for simultaneously chiral and achiral imaging.

2.3 Design procedure

While three working mechanisms could be adopted to design a metasurface for varies of applications, a metasurface can be designed following a standard procedure including three steps (Figure 2.3) [9, 71, 72].

The design flow starts from the determination of target phase profile as shown in Figure 2.3(a) at the expected working wavelength λ . The target phase profile is dependent on the application

requirements. For example, the hyperbolic phase profile Figure 2.3(a) is generally required for achieving diffraction-limited focusing, and the vortex phase profile is needed for generating vector vortex beams.

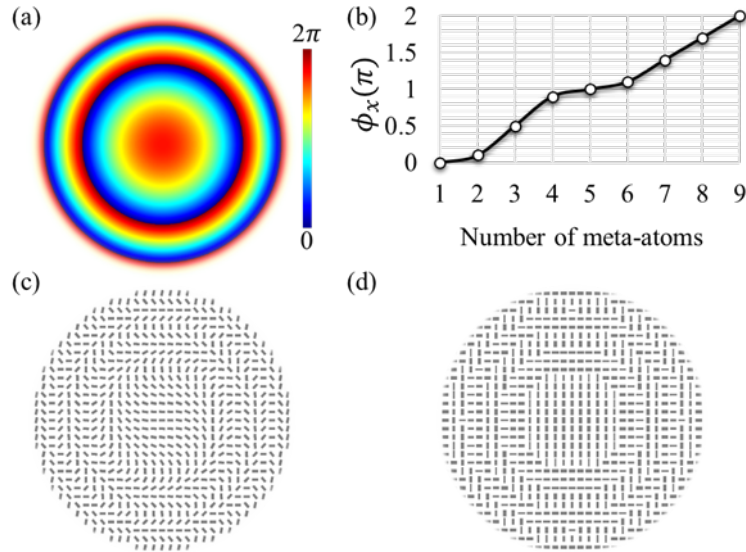


Figure 2.3 Designing procedure of a metasurface.

(a) target phase profile, (b) phase library, (c) and (d) distribution of meta-atoms.

The second step is to build up the library of meta-atoms using numerical simulation tools (e.g., Lumerical FDTD solver, COMSOL, and CST). In this step, the first thing should be considered is metasurface's polarization-dependence. If we want to manipulate the light in a polarization-independent way, circular pillars and square pillars can be chosen for imposing propagation phase. To realize polarization-dependent manipulation, the common choice of the meta-atoms is elliptical and rectangle nanofins. Moreover, elliptical and rectangle nanofins can be used for the classical and non-classical spin-multiplexing metasurface. As shown in Figure 2.2, once the structure of the meta-atoms is confirmed, we can sweep the dimensions (e.g., H, P, W, L) to build up a meta-atom's library with high transmission.

If we target at designing a metasurface working for a specific circular polarization state based on pure geometrical phase [Eqs. (2.6) and (2.7)], we only need select a meta-atom unit which can fulfill two requirements of $|\phi_x - \phi_y| = \pi$ and $t_x = t_y = 1$ [e.g., an arbitrary point in Figure 2.2(c)]. If we want to design a metasurface based on propagation phase or spin-multiplexing phase, the meta-atoms library can be built up by choosing 9 meta-atoms from Figure 2.2 for achieving 2π phase coverage of propagation phase [Figure 2.3(b)]. The selection rule relies on the condition of adopted working regime.

The last step of designing a metasurface is digitalizing the target phase profile Ψ based on the period P of meta-atom and determine the meta-atom's distribution on the flat substrate. For designing a polarization-dependent metasurface based on geometrical phase, the key target is to confirm the rotation angle θ of the selected meta-atom at each lattice via diving the local phase Ψ_Ω by 2 (Ω denotes the lattice position). This process needs to be repeated for all lattices until a whole metasurface is designed. Figure 2.3(c) shows the meta-atom's distribution in a geometrical phase metasurface.

While the propagation phase is required for achieving the target phase profile Ψ , a searching algorithm should be adopted to select a right meta-atom from the library [e.g., the Figure 2.3(b)] for imparting the required propagation phase ϕ . After repeating this process for all lattices, the whole metasurface is designed. Figure 2.3(d) shows the layout of a spin-multiplexing metasurface, which illustrates that the spatial-dependent phase profile Ψ is obtained via the spatial-dependent distribution (e.g., θ, W, L) of meta-atoms in a spin-multiplexing metasurface.

2.4 Conclusion

This chapter starts from the commonly used propagation and geometric phase in designing a non-resonance all-dielectric metasurface. Based on a general working mechanism, the design of a metasurface is classified to three regimes. Compared with the widely adopted classical spin-multiplexing regimes, the novel non-classical spin-multiplexing regime has a lower requirement on designing a spin-multiplexing metasurface, which makes it is possible to obtain multi-channel metasurface via low refraction index material (e.g., Si_3N_4). Through the theoretical analysis, it is figured out that all experimental results obtained in chapters 3 -8 are respectively corresponding to the three working regimes, which illustrates the inherent coherence of following chapters. In the last section of this chapter, a standard design procedure of the metasurface is demonstrated in detail.

Chapter 3 High-NA metalens for optical levitation and rotation

3.1 Introduction of optical levitation system

Nanoscale or microscale particles optically levitated in a vacuum are well isolated from the environment (e.g., the damping from thermal bath and molecules collision). Due to the absence of direct dissipation and any physical contact in vacuum conditions, the thermal-mechanical noise of this optically levitated system is very low, and it has been predicted that this system could obtain a mechanical quality factor (Q-factor) as high as 10^{12} for the centre of mass (COM) mode [17]. Hence, optically levitated particles could be used for sensing weak forces and torques with high sensitivity [73-75].

The other significant advantage of an optical levitation system in a vacuum is its high tunability, making it possible to study some unobservable physical phenomenon in the air or other viscous medium. Firstly, the motion of the optically levitated particles could be changed in-situ by simply adjusting the trapping light [24]. For example, rotation of the optically levitated particles could be accelerated to ultrahigh frequency exceeding gigahertz simply by changing the polarisation of the laser from linear to circular. It has been verified that the highest rotation speed is only limited by the tensile strength of the material of the levitated particles, which means that the properties of material and friction at ultrahigh rotation frequency could be studied. Secondly, the interaction of the optically levitated particles could be simply tuned by changing the gas pressure in the vacuum chamber, which means that the optically levitated particles could be employed to study stochastic thermodynamics [29]. Because of the tunability of the system parameters, optically levitated particles are also suitable for the study of nonlinear nanomechanical phenomena [76], which are important for the miniaturization development of future mechanics and photonic sensors. Because of optical levitation system's advantages, this chapter focuses on the optical levitation application of a metalens.

As shown in Figure 3.1, a typical setup for optical levitation in a vacuum is made up of four main sub-systems, including an optical trapping system, an optical detection system, a feedback control system, and a vacuum system [77]. The optical detection system is adopted to detect scattered light in-time and analyse particle motion. The feedback control system is for stabilizing the particle in a high vacuum. The vacuum system is utilized to control the air pressure around the optical trap and obtain the high-vacuum condition. The optical trapping system is the key part of an optical levitation system, and there have been many optical configurations for levitating

particles in a vacuum. As the metalens will be used for miniaturizing and scaling up the optical trapping system, current optical traps configurations and their problems will be analysed.

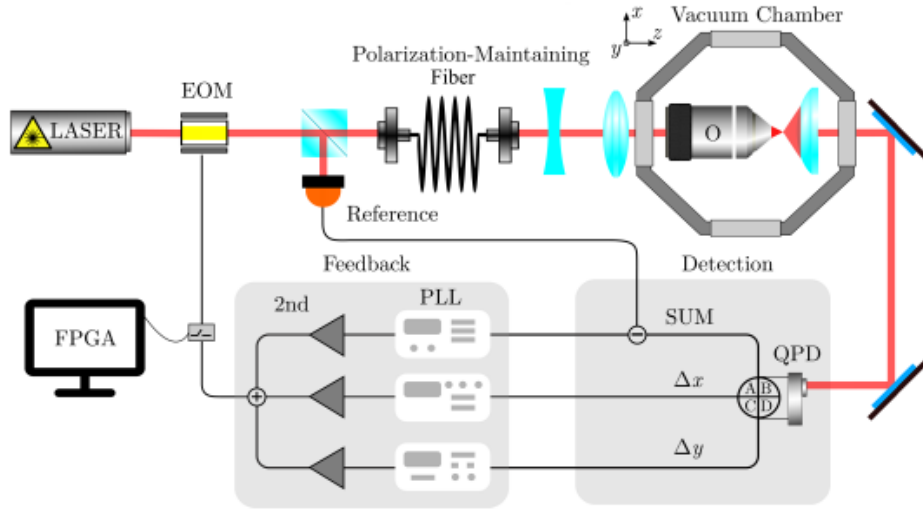


Figure 3.1 A typical optical levitation system [77].

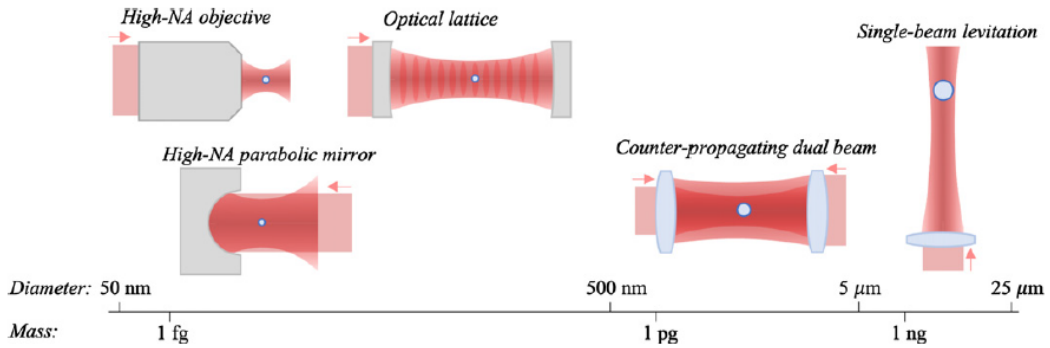


Figure 3.2 Optical trapping configurations for optical levitation system [78].

Figure 3.2 shows the optical configurations adopted for levitating particles in a vacuum. Three configurations, including the high-NA objective, high-NA parabolic mirror, and the optical lattice, are utilized to trap objects of subwavelength size [78]. However, it has been pointed out that the aberrations of a refracted optical trapping configurations, including defocus, spherical aberration, and chromatic aberrations, would decrease the Strehl ratio and degrade the levitation performance [77]. It is well-known that the aberrations arising from the refractive elements could be compensated by the utilization of several other lenses or an adaptive optics system. However, the residual aberration after compensation still affects the optical levitation performance, and the system complexity is heavily increased by the utilization of the other elements. This problem motivates the introduction of the reflective optics element in optical levitation systems.

As shown in Figure 3.2, a commonly utilized reflective element is the high-NA parabolic mirror made in metal. In theory, the parabolic mirror can provide several advantages. Firstly, it eliminates the aberrations and makes the focal point be at the expected position. Secondly, it is

easier to implement and use in high-vacuum conditions compared with the refractive high-NA objective. However, the machine errors containing the surface deviation and roughness will introduce phase error and decrease optical levitation performance. In addition, a high-performance metal parabolic mirror is bulky, heavy, and expensive.

The metalens which can achieve aberration-free focusing with high NA opens a door of miniaturizing an optical levitation system with lightweight and low cost [79]. A pioneering work using metalens with an NA of 0.88 demonstrates optical levitation in a vacuum [23]. However, the spin motion mode of an optical levitated particle is not demonstrated in the pioneering work limited by the particle's spherical shape. In this chapter, to realize optical levitation and rotation in a vacuum, we'll firstly demonstrate a polarization-independent metalens with a high NA of 0.91 and an aberration-free focusing ability.

3.2 Aberration-free and high-NA focusing

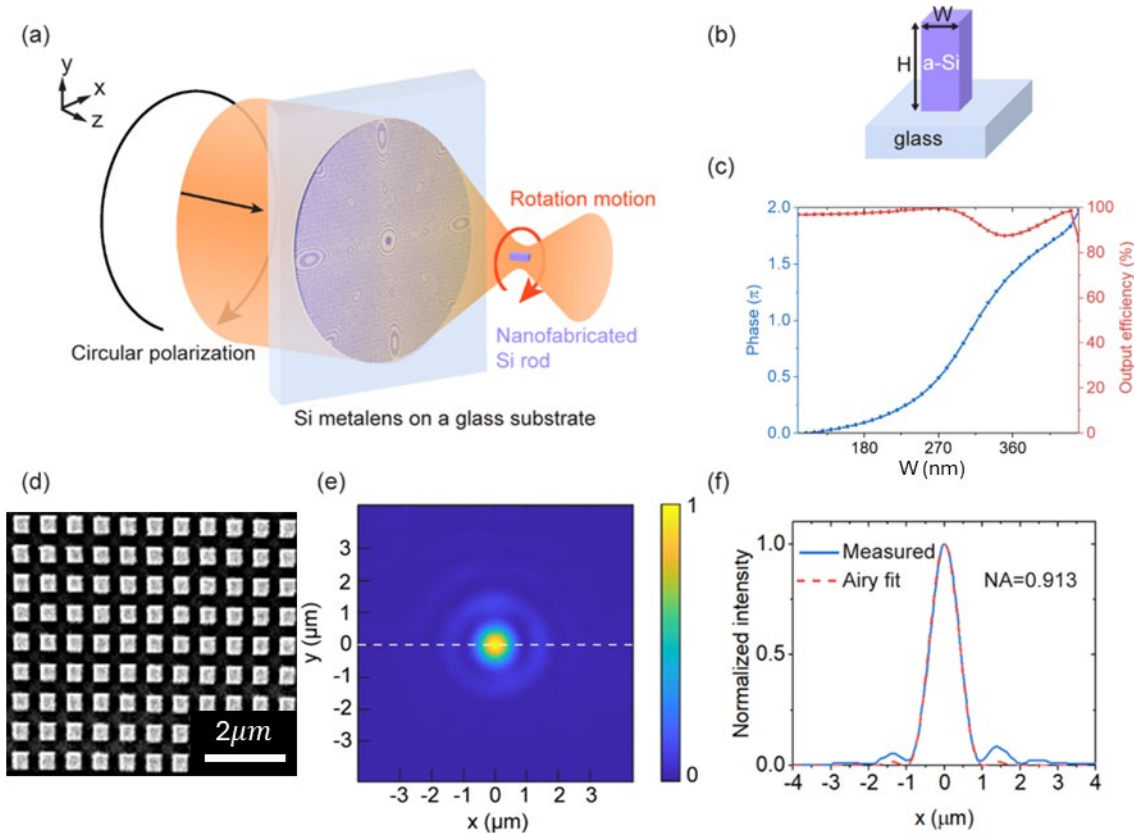


Figure 3.3 Metalens for optical levitation experiment.

(a) Schematic of the optical levitation in vacuum combining the nanofabricated metalens and a nanofabricated rectangular nanorod. (b) Schematic of the metalens building block: a single a-Si rectangular nanopillar on a glass substrate. The pillar height and period are 800 nm and 600 nm respectively. (c) Simulated propagation phase (blue and left axis) and transmission (orange and right axis) as a function of the nanopillar's width W

(110nm to 440nm). (d) Top-view SEM of the centre of the fabricated metalens. (e) Normalized measured intensity distribution in the focal plane. (f) The intensity profile along the x-axis passes through the focus, together with the fitting to the Airy profile.

To manipulate the motion mode and realize optical levitation of the levitated particles in the wavelength of 1550nm [Figure 3.3(a)], a polarization-independent metalens is designed based on isotropic a-Si nanopillars [Figure 3.3(b)]. To realize a high working efficiency and avoid high-order diffraction for high-NA focusing, the period and height of the a-Si nanopillars are optimized to be 600nm and 800nm, respectively based on a commercial FDTD (finite-difference time-domain) solver (Lumerical FDTD Solutions). Then, the nanopillars library is built by sweeping the nanopillar's width W from 110nm to 440nm as shown in Figure 3.3(a). It could be seen that the nanopillars library achieves a 2π phase coverage and a high transmission (>90%).

To realize an aberration-free and diffraction-limited focusing effect, the hyperbolic phase profile [Figure 2.3(a) and Eq. (3.1)] is adopted in designing the metalens. In Eq. (3.1), $\lambda = 1550\text{nm}$ is the working wavelength, $f = 200\mu\text{m}$ is the target focal length, and ρ is the radial coordinate in a polar coordinate system. To match our laser beam's diameter, the designed metalens has a diameter of 1.2mm.

$$\Phi(\rho) = \frac{2\pi}{\lambda} (f - \sqrt{f^2 + \rho^2}) \quad (3.1)$$

3.3 Fabrication and characterization

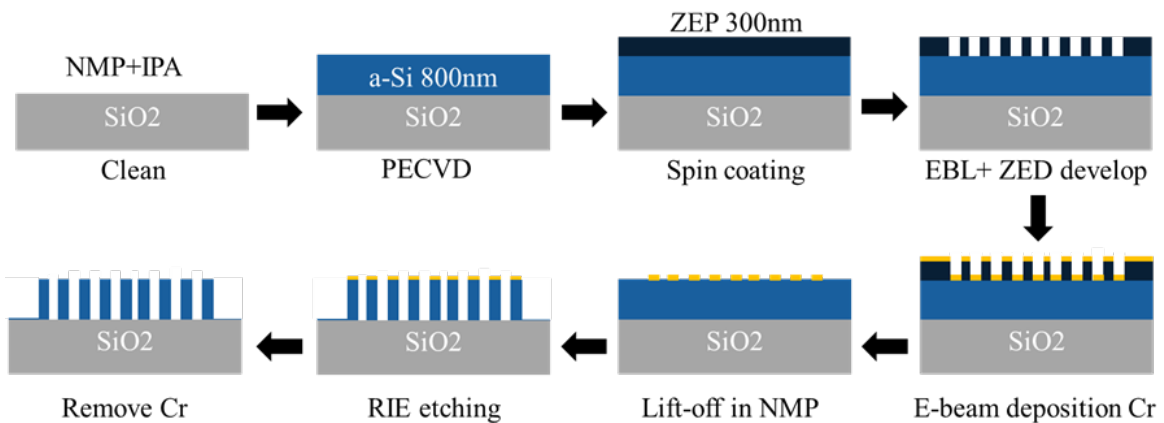


Figure 3.4 Fabrication flow of the a-Si metalens.

The designed metalens are fabricated in our University Cleanroom following a CMOS-compatible process as shown in Figure 3.4. The metalens samples are fabricated on a double-side polished SiO₂ wafer. The wafer is firstly cleaned in NMP for 10mins and IPA for 10min. Then, a layer of amorphous silicon (800nm in thickness) is deposited in a rate of 16nm/min via PECVD at 250°C.

ZEP520A resist is spin coated on the wafer and baked on a hot plate for 3mins at 180°C.

Subsequently, the metalens pattern is defined by the e-beam lithography (EBL) and develop process in ZED solution. As the hard mask, a 35nm-thick Cr layer is coated on the substrate by e-beam evaporation and followed by a lift-off in NMP. Consequently, the designed patterns are transferred to the Cr layer. Then, the wafer with patterned Cr layer is dry etched via reactive ion etching (RIE) in a rate of 20nm/min. Finally, metalens samples are obtained after removing Cr layer via wet etching in Cr etchant. Figure 3.3(d) shows the SEM image of the fabricated metalens sample. More details on fabrication can be found in Appendix B.

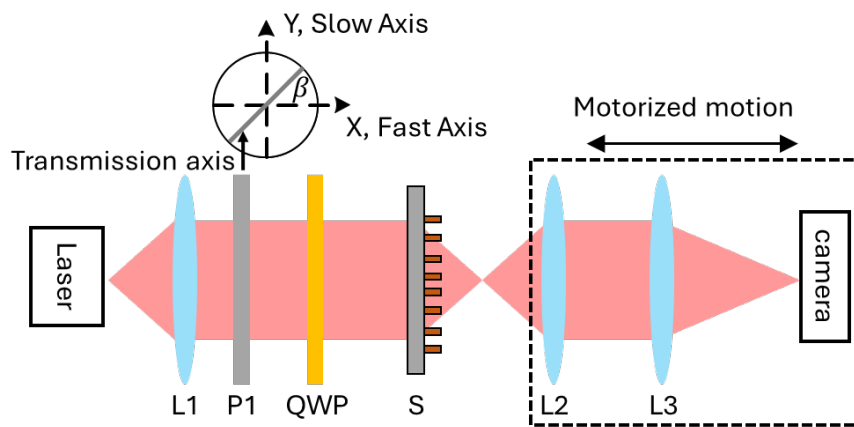


Figure 3.5 Optical configuration for characterizing a-Si metalens samples.

To characterize the metalens sample's focusing performance, a microscope (Figure 3.5) with a high NA of 0.9 and a high magnification of 100X working in the wavelength of 1550nm is customized in our lab. In the microscope, the 1550nm laser beam is collimated via collimator (L1) and incident to the rear surface of the metalens sample (S). Then, the focal point of the metalens is collected by a high-NA objective lens (100X, NA 0.9, L2) and imaged to an InGaAs camera by a tube lens (L3). A polarizer (P1) and quarter-waveplate (QWP) are adopted to manipulate the laser beam's polarization state. β denotes the angle between the QWP's fast axis and the transmission axis of the polarizer P1. The imaging section from L2 to camera is motorized for precisely measuring its focal length.

For measuring the focal length and focal point's intensity distribution, the objective lens L2 is firstly focused on the metalens sample. Then, the imaging system is driven to move away from the metalens' surface for finding the focal plane and measuring the focal points' intensity distribution. Figure 3.3(e) shows the measured optical intensity distribution in the focal plane, revealing a clear and well-defined focal spot. Figure 3.3(f) presents a cut across the x-axis passing

through the focus [dotted line in Figure 3.3(e)], along with the fitting to the Airy pattern. The Airy radius which is defined as the radius from the central peak of the Airy function to its first minimum, is measured to be $1.036\mu m$. Finally, the effective NA of the metalens sample can be calculated to be 0.91, which is slight smaller than the target NA of 0.95. Both the fabrication error and the 0.9 NA of objective lens L2 can contribute to the difference in NA.

3.4 Optical levitation and rotation

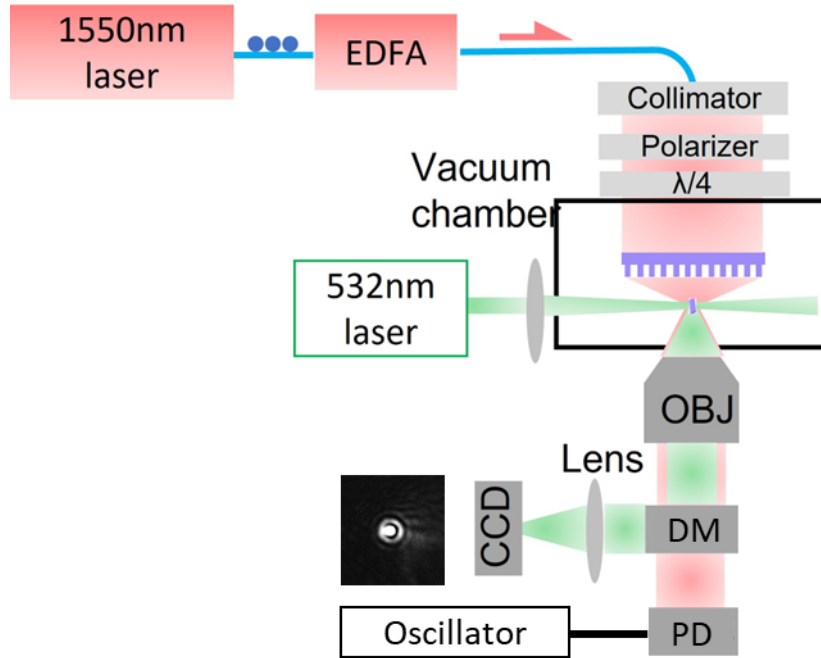


Figure 3.6 Optical configuration of the metalens-based optical levitation system.

The experimental setup for levitating a nanorod using the fabricated metalens sample is shown in Figure 3.6. A 1550 nm laser, amplified by an erbium-doped fiber amplifier (EDFA), is collimated to a polarizer for obtaining linearly polarized light. A QWP is utilized to control the light's polarization state. To detect the nanorod's motion modes, the scattering light from the nanorod is collected by an objective lens and guided to a photodetector (PD) via the dichroic mirror (DM). As the scattering light is modulated by the nanorod's motion, the nanorod's motion can be detected by the PD and oscillator. To capture the video of the levitated nanorod, a 532nm imaging path (the green path in Figure 3.6) is built as well. The 532 nm laser is firstly focused on the levitated nanorod and the scattered by the nanorod. The scattered 532nm laser beam is collected by the objective lens and imaged to a visible camera via tube lens. The inset in Figure 3.6 shows the optical image of the levitated nanorod. Nanorods having a dimension of $214nm \times 220nm \times 753nm$ are fabricated in our cleanroom and loaded into the optical trap using an ultrasonic nebulizer.

Once a nanorod is trapped, the vacuum chamber's pressure is pumped down to 4 mbar to measure the frequencies of COM's three translation motion modes (X, Y, and Z). Figure 3.7(a) shows the power spectral density (PSD) of the nanorod's translation motion when the trapping light is linearly polarized. It can be seen that the oscillation frequencies in the x, y, and z directions are 43.6 kHz, 78.3 kHz and 122.8 kHz, respectively. The translation frequency in the z-direction is lower than the other frequencies because the optical focus is elongated along the direction of the propagating beam. A second harmonic signal (i.e., 2Z) along the z-direction is observed in the PSD spectrum due to the non-perfectly harmonic trapping potential.

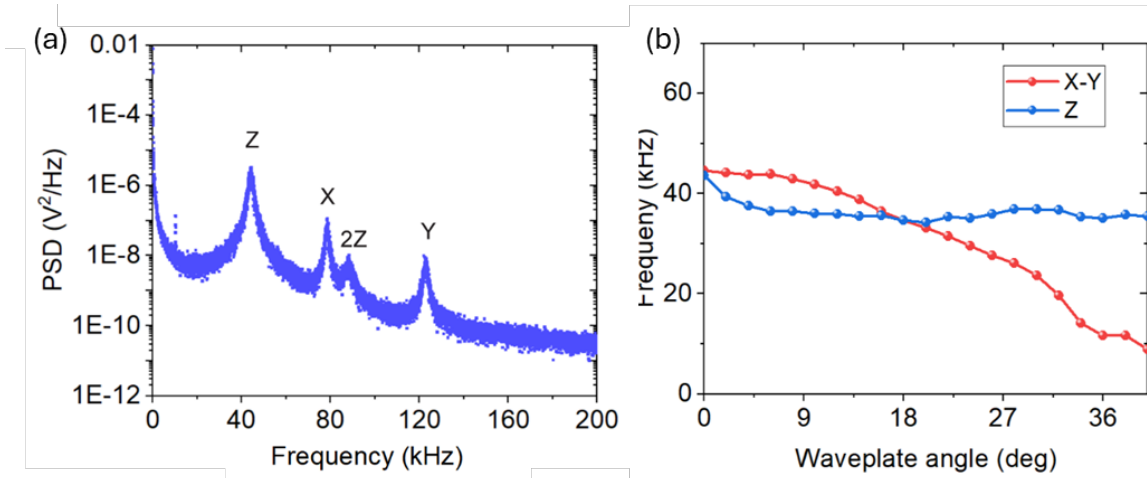


Figure 3.7 COM motions of levitated nanorod.

(a) Power spectral density (PSD) of the COM translation motions X, Y, and Z when the trapping laser beam is linearly polarized (i.e., the QWP has an angle of zero degree). (b) The measured COM oscillation frequencies as a function of the laser's polarization state (i.e., the QWP angle).

Then, this chapter manipulated the COM motion's frequency via tuning the trapping laser beam's polarization state. It is well known that a focal point's intensity distribution would be elongated along the laser beam's polarization direction, the circularly symmetric focal point can only be obtained when the laser is circularly polarized. As a result, the intensity gradient along the laser's polarization direction would be smallest in the focal plane when the laser beam is not circularly polarized, which would reduce the motion frequencies. Therefore, the X and Y frequencies of the COM motions in the focal plane can be tuned by the laser beam's polarization state. In experiment, as shown in Figure 3.7(b), it is measured that the frequencies of the COM motions along X and Y directions are a function of the waveplate angle (i.e., the laser beam's polarization state). The waveplate angle in Figure 3.7(b) refers to the angle between the fast axis of QWP and the polarizing axis of the polarizer. The ellipticity of the laser beam as well as the intensity gradient difference in the X- and Y-directions increases with the increasing waveplate angle. In Figure 3.7(b), the frequency difference (i.e., $\Delta f_{x-y} = f_x - f_y$ plotted in red line) is adopted as a merit to

evaluate the manipulation of the in-plane COM motions via tuning the laser beam's polarization state. In Figure 3.7(b), Δf_{x-y} gradually reduces with increasing the waveplate angle, which indicates the motion frequencies in the x and y directions are becoming closer with the laser beam being tuned to be circularly polarized from linearly polarized. Meanwhile, the motion frequency in the z direction remains constant [the blue curve in Figure 3.7(b)], as the field distribution in the z direction is not affected by the laser beam's polarization state. The frequency's fluctuations in the Z direction mainly result from the variation of laser power.

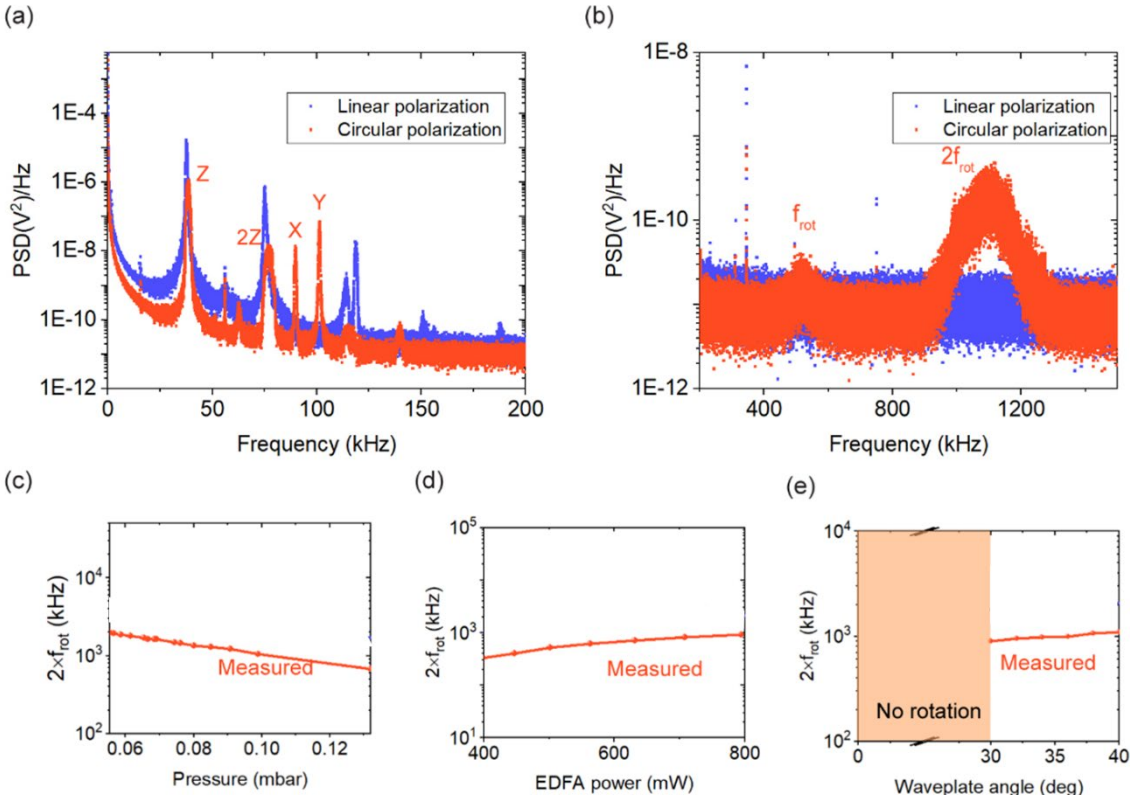


Figure 3.8 Rotation dynamics of levitated nanorod.

(a) Power spectral density (PSD) of the motions of the levitated particle at 0.11 mbar, with linear (blue line) and circular (red line) polarization states, respectively. The frequency ranges from (a) 0 to 200 kHz and (b) 200 to 1500 kHz. The rotation frequency (c) decreases with the increasing pressure, and (d) increases with the increasing trapping. (e) The rotation frequency is a function of the QWP angle. When the plate angle is larger than 30°, the particle starts to rotate and the rotating frequency increases with the plate angle.

Finally, to mitigate the damping effect caused by gas molecules and observe a clear rotational signal, pressure inside the vacuum chamber is furtherly pumped down to 0.11mbar. Figure 3.8(a-b) shows the PSD spectrum from 0 to 1500KHz measured for circularly polarized (orange curve) and linearly polarized (blue curve) laser beam. Comparing the blue curve in Figure 3.8(a) and the curve in Figure 3.7(a), when the laser beam is linearly polarized, the PSD spectrum obtained at

the pressure of 0.11mabr is similar to that [Figure 3.7(a)] at 4 mbar, but the linewidth of each peaks is significantly reduced. This is because the levitated nanorod's translation motions in X, Y, and Z directions are simply harmonic oscillations, where the oscillation frequency is independent of the environment damping (i.e., the pressure) but the mechanical quality factor can be improved with reducing the environment damping/pressure.

Figure 3.8(b) clearly shows that two high frequencies peaks f_{rot} and $2f_{rot}$ appears in the PSD spectrum with tuning the laser beam to be circularly polarized from linearly polarized. Figure 3.8(c) demonstrates that the frequency $2f_{rot}$ linearly scales with reducing the pressure, which is a typical feature of a levitated particle's rotation mode. In the PSD spectrum, the amplitude of $2f_{rot}$ is much larger than that of f_{rot} because of the symmetry of the levitated nanorod.

This thesis also studied the dependence of the rotation frequency and the laser's power [Figure 3.8(d)] and polarization state [Figure 3.8(e)]. From the Figure 3.8(d), the rotational frequency is almost linearly proportional to the laser power. From the Figure 3.8(e), there is no rotational PSD signal in the frequency spectrum when the QWP angle is smaller than 30° . With the QWP angle becoming larger than 30° , the levitated nanorod is driven to rotate, and the rotational frequency scales with the QWP angle. Because, with rotating the QWP from 0° to 45° , the laser beam is tuned to be circularly polarized, and more SAM can be transferred to the levitated nanorod.

In addition, a hybrid numerical calculation method is proposed in this thesis to calculate the optical forces and torques exerted on optically levitated particles with arbitrary geometric shape, which will be demonstrated in chapter 9. Furthermore, in chapter 9, a prototype of metalens-based levitated optomechanics sensor (LMOS) is designed for boost the commercialization of optical levitation sensors.

3.5 Conclusion

In the polarization-independent regime, a metalens sample with a high NA of 0.91 and aberration-free focusing ability is experimental demonstrated in this chapter. Then, this chapter builds up an optical levitation system including the metalens-based optical traps, motion detection subsystem, motion imaging subsystem, and vacuum chamber system. Based on this optical levitation system, a nanorod is optically levitated and rotated to a high speed of around 1MHz. The translational and rotational motions' dependence on the trapping laser's polarization state, power, and the vacuum pressure are experimentally investigated in detail. The experimental results meet well with theoretical expectation.

Chapter 4 Tunable on-chip optical traps for levitating particles

4.1 Introduction of optical traps array

While the optically levitated single particle could be used for sensing forces and torques with high sensitivity, the coupling effect of multiple levitated particles at a close distance could furtherly improve the sensing sensitivity. The weak coupling between multiple oscillators (i.e., the levitated particles) could be modulated to realize nonlinear dynamics, nonreciprocal dynamics, and mode localization, which can provide higher sensitivity than a single oscillator. Therefore, the ability to trap and manipulate simultaneously multiple particles or even an array of particles in a vacuum will be of vital importance [28, 32, 33, 80]. In general, there are two ways of trapping more than one particle at a time. The first way is using the standing wave generated by two counter-propagating beams [34], and the other way is introducing a modulator [e.g., spatial light modulator (SLM), acoustic-optics deflector (AOD), digital micromirror device (DMD)] to a conventional optical trapping system [27, 36, 81]

Because a 2-level blazed grating phase profile is required to split the incident laser beam into two symmetric diffraction orders in a SLM-based optical traps system, the light utilization efficiency of the SLM would be lower than 30% at the wavelength of 1550nm [82]. While the transmission of an objective lens with a high numerical aperture can be corrected to be around 85% in the visible spectrum, that would be only around 50% in near-infrared spectrum [27]. As a result, the overall efficiency of a SLM-based optical traps would be only around 5% because there is some insertion loss arising from the other bulky optical components. In addition, limited by the modulation principle of a SLM, there would be continuous fluctuation in the intensity of the two focal points. In an AOD-based optical traps, because of the diffraction loss and the objective loss, light utilization efficiency is low as well. In addition, the optical intensity of each trap would be continuously fluctuated due to the instability of RF frequency and power. Moreover, the optical frequency of each trap is different. Both the intensity fluctuation and optical frequency difference highly suppress the interactions between trapped particles [83].

Remarkably, it has been shown that transferring spin angular momentum (SAM) carried by a circularly polarized (CP) trapping beam [38] to a trapped particle can be used to rotate the nanoparticle at high speed [24, 25]. It has been further shown a high-speed rotation effectively removes particle's structural anisotropies arising from fabrication limitations and prevents motion instabilities [27]. This then requires tuning both focal points to be circularly polarized (CP)

by inserting polarization modulation elements between the focal plane and the modulator. As a result, the optical levitation system becomes bulky, complicated, and difficult to align, making modulator-based systems inconvenient for practical applications [28, 33, 84] and the scaling of the number of devices [21]. The low efficiency and intensity instability are further disadvantages of using a modulator-based optical traps.

To pave the way for scaling the number of levitated optomechanical devices or realising of paralleled levitated sensors as well as improving the efficiency, it is essential to miniaturize and simplify the levitation system and one option appears to be the realisation of levitated sensors on the chip. As shown in Figure 4.1, based on a single-layer dielectric metasurface, this chapter proposes a scalable single chip with tunable optical traps for realizing bistable potential well and double potential wells with high NA, high efficiency, and no intensity fluctuation at focal points, which can be extended to multiple-particle traps benefiting from the breakthrough in the limitation of polarization-multiplexing metasurface.

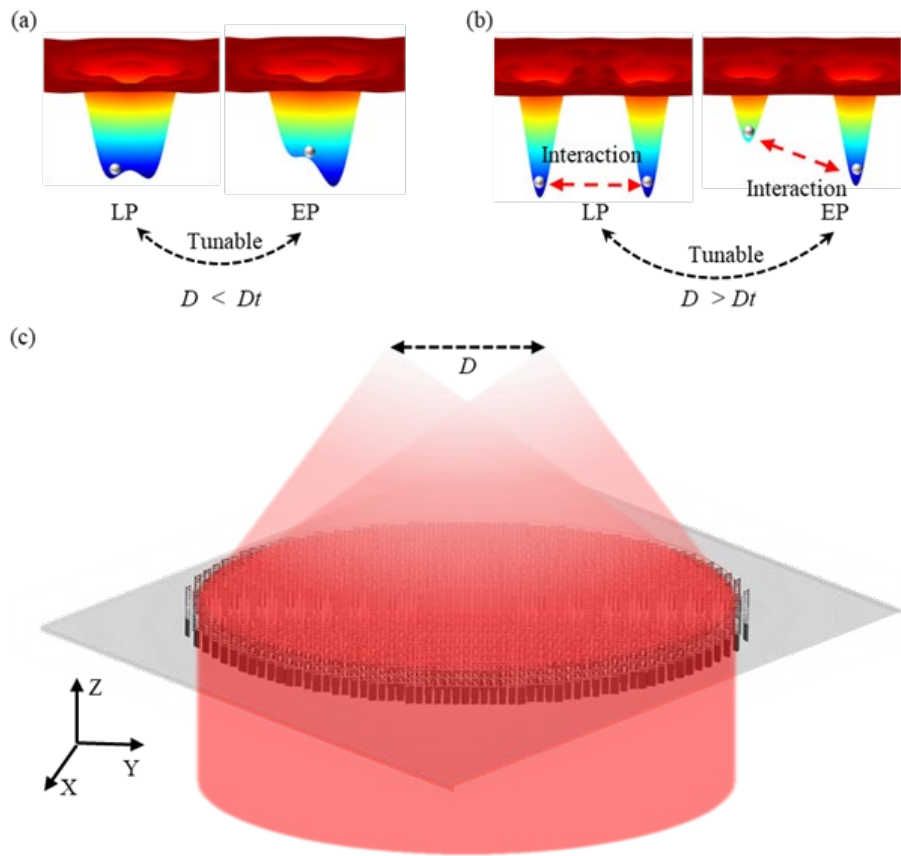


Figure 4.1 Conceptual figure of the on-chip optical levitation system.

(a) A tunable bistable potential well when the distance D is smaller than a threshold D_t for non-equilibrium thermodynamics or nonlinear dynamics. (b) A tunable two potential wells when the distance D is larger than a threshold D_t for optical coupling application. (c) One-chip optical levitation system based on a single-layer metasurface.

Importantly, the focal points (Figure 4.1) are inherently circularly polarized and support trapping particles with high-speed spin modes. This chapter experimentally obtains two near-diffraction-limited focal points at the wavelength of 1550nm with a high numerical aperture of 0.9, and high light utilization efficiency of 31%, and experiments demonstrate that the distance between two focal points can be accurately tailored, and relative intensity between two traps can be dynamically and continuously tuned by changing the polarization state of the incident laser beam. Therefore, the particles levitated in each focal point would experience tunable optical trapping potential. While the distance between two focal points is close enough, the focal points will combine and can provide a bistable potential well. Finally, this chapter experimentally and theoretically shows the metasurface's ability to construct an on-chip optical levitation system with tunable potential wells.

4.2 Design of the metasurface sample

The metasurface for controlled double focal points is designed based on an out-of-plane focusing phase profile and works in the classical spin-multiplexing regime. In the metasurface, one incident laser beam could be directly focused to two or more circularly polarized focal points with high NA, as shown in Figure 4.1, which would effectively reduce the loss and instability arising from the optical components in an SLM-based optical binding system. By tailoring the distance D between two focal points, the potential well could be shaped from the bistable potential well [Figure 4.1(a)] for a single particle to separately double potential wells [Figure 4.1(b)] for the optical coupling of two particles. As the two focal points respectively correspond to the LCP and RCP components, the relative intensity between two focal points can be tuned by manipulating the laser beam's polarization state.

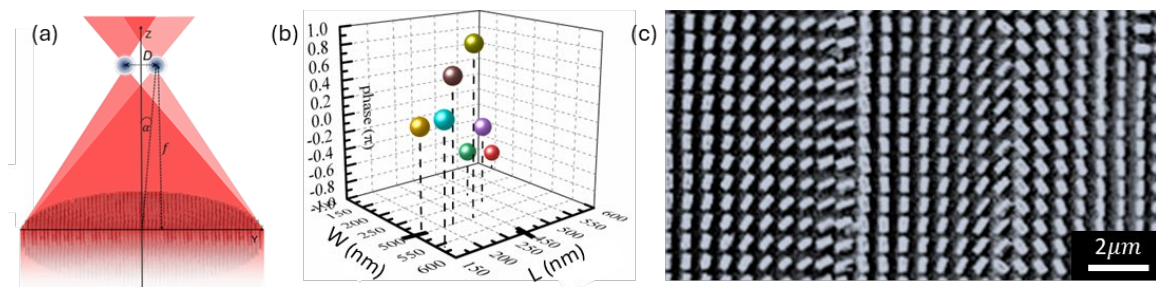


Figure 4.2 (a) Geometrical parameters of two focal points; (b) Nanofins library; (c) SEM.

As the metasurface working the classical spin-multiplexing regime, the incident laser beam could be coupled to the orthogonal $|R\rangle$ and $|L\rangle$ channels which can be separately imposed the phase profile of $\Phi_R = 2\theta + \phi_p$ and $\Phi_L = -2\theta + \phi_p$. For focusing the $|R\rangle$ and $|L\rangle$ components into two focal points at a close distance in the same focal plane, the off-axis focusing phase profiles [Eq. (4.1)] are adopted for Φ_R and Φ_L , where (ρ, φ) is the polar coordinate of each nanofin located, f

and α are the target focal length and tilt angle, as shown in Figure 4.2(a). As a result, the distance D between two focal points could be expressed as $D = 2f\tan(\alpha)$ and be tailored by tuning the target α for a given f or NA, where $NA = R/\sqrt{R^2 + f^2}$ and R is the radius of the whole metasurface [57].

$$\begin{cases} \Phi_L(\rho, \varphi) = \frac{2\pi}{\lambda} [f - \sqrt{f^2 + \rho^2 - 2\rho f \sin(\alpha) \cos(\varphi)}] \\ \Phi_R(\rho, \varphi) = \frac{2\pi}{\lambda} [f - \sqrt{f^2 + \rho^2 + 2\rho f \sin(\alpha) \cos(\varphi)}] \end{cases} \quad (4.1)$$

To impose the target phase profiles on the ongoing light beam, a nanofin library [Figure 4.2(b)] including eight cells is built up based on the large library shown in Figure 2.2 where a group of nanofins with different W and L are selected to achieve a 2π phase coverage of ϕ_p and keep $|\phi_x - \phi_y| = \pi$. The period and height are respectively optimized to be 650nm and 800nm in advance.

The tailoring ability of distance D and potential wells is verified in numerical simulation. As shown in Figure 4.3(a1)–Figure 4.3(c1), for a given $f = 5\mu\text{m}$ and $NA=0.9$, the distance D along Y direction varies from $0.7\mu\text{m}$ to $3.15\mu\text{m}$. Note that, as shown in Figure 4.3(a), the two focal points emerge into one when $\alpha = 2^\circ$ and $D = 0.7\mu\text{m}$, because the distance D of $0.7\mu\text{m}$ is smaller than the diffraction limitation ($1.18\mu\text{m}$) of each focal point. The diameter and focal length f used in the simulation are $20\mu\text{m}$ and $5\mu\text{m}$, respectively, which are much smaller than those of fabricated samples and is limited by our computer memory.

For each distance D , the potential wells $U(y)$ experienced by a trapped SiO_2 spherical particle are calculated as well to show that the potential wells $U(y)$ can be tailored for studying optical coupling effect using Eq. (4.2) and Eq. (4.3) [77].

$$U(y) = -\frac{2\pi n_s r^3}{c} \left(\frac{n_r^2 - 1}{n_r^2 + 2}\right) I(y) \quad (4.2)$$

$$I(y) = \frac{c n_s \epsilon_0}{2} |E(y)|^2 \quad (4.3)$$

Where $n_s = 1$ is the refraction index of the surrounding environment, r is the radius of the trapped particle and assumed to be 100nm, $n_r = 1.48$ is the relative refraction index between the SiO_2 particle and the n_s , c is the speed of light in vacuum, and the ϵ_0 is the dielectric constant in vacuum. E is the electrical field amplitude of the focal plane which is simulated via Lumerical FDTD as shown in Figure 4.3(a1)–Figure 4.3(c1). Note that the incident laser power is normalized to be 200mW in simulation.

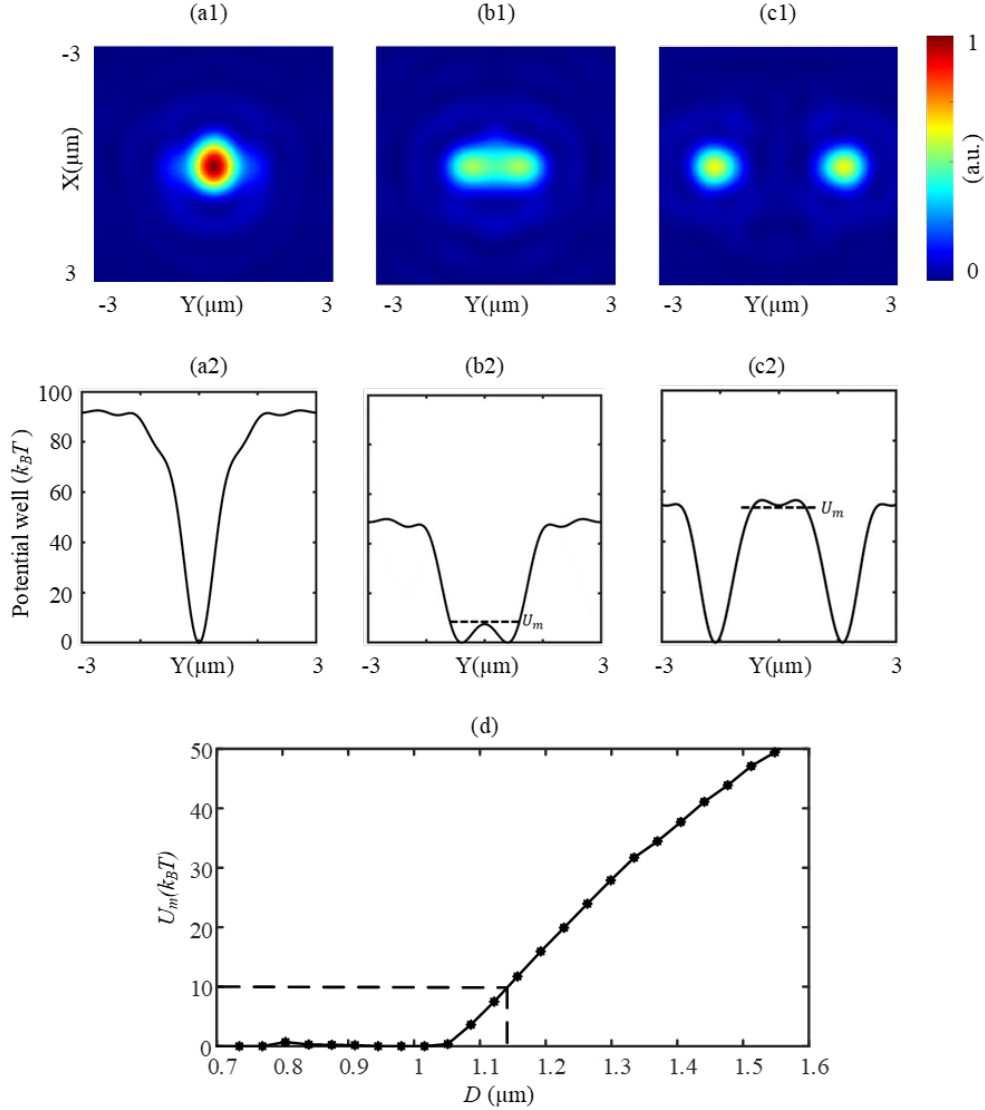


Figure 4.3 Simulated focal points and potential wells.

(a) –(c) are the simulated optical intensity (1st row) and potential well (2nd row) in the focal plane with the distance D changing from $0.7\mu\text{m}$ to $3.15\mu\text{m}$ when the incident laser beam is linearly polarized. (d) central depth of potential well vs the distance D .

As shown in Figure 4.3(a2) – Figure 4.3(c2), the central depth U_m of the potential wells goes up with increasing the distance D . According to Ashkin's criterion, the depth of the potential well should be higher than $10k_B T$ for stably trapping a particle in the focal point [85, 86]. k_B is the Boltzmann constant, and T is the environment temperature assumed to be 300K in our calculation. Therefore, the distance D should be large enough to obtain two coupled optical traps. Figure 4.3 (d) shows the relationship between the central depth U_m and the distance D , which demonstrates that two optical traps with a $U_m > 10k_B T$ can be achieved, when the distance $D > 1.14\mu\text{m}$. Therefore, $1.14\mu\text{m}$ is regarded as a distance threshold a D_t

As shown in Figure 4.3(b) and Figure 4.3(d), the potential well generated by the focal points with a distance D of $1.12\mu\text{m}$ (smaller than D_t) has a central depth U_m of $7k_B T$ which cannot stably trap two particles at each focal point at the same time. As a result, the potential well shown in Figure 4.3(b2) can be seen as a double-well potential or bistable optical potential well which could stably trap one single particle. Therefore, it can be used for studying the nonlinear dynamics of one levitated particle.

4.3 Metasurface preparation and characterization

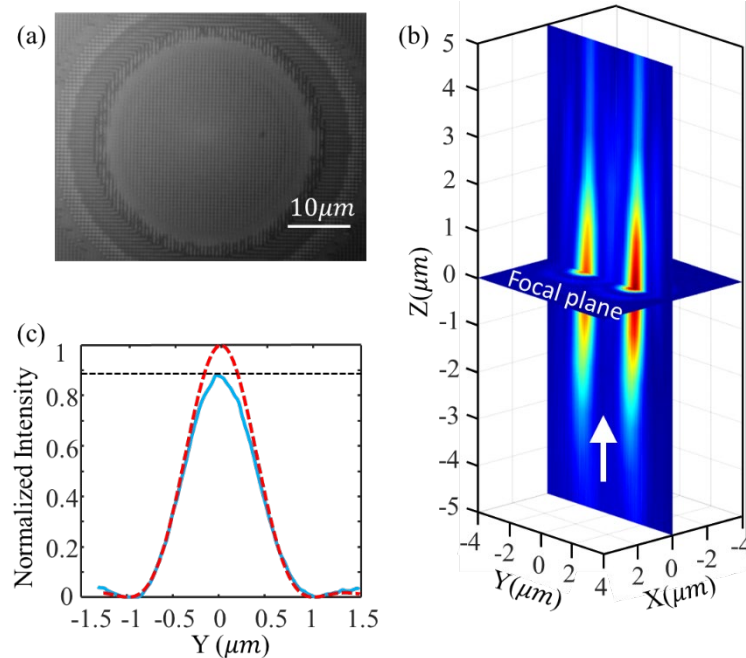


Figure 4.4 Characterization of the metasurface sample.

(a) Central image of the metasurface; (b) Strehl ratio of samples. Red dashed curve: diffraction limitation corresponding to 0.9; Blue line: measured intensity at focal plane; (c) focusing process near the focal plane.

In the experiment, a series of metasurface samples with the same radius ($600\mu\text{m}$) and focal length ($300\mu\text{m}$) (i.e., $\text{NA}=0.9$) are fabricated following the steps in Figure 3.4 and measured via the home-customized microscope in Figure 3.5. Figure 4.2(c) shows the SEM image of fabricated metasurface sample. For measuring the focal length and focal point's intensity distribution, the objective lens L2 is firstly focused on the metasurface [Figure 4.4(a)]. Then, the imaging system is driven to move away from the metasurface's surface to find the focal plane and measure the focal points' intensity distribution. In the experiment, the distance (i.e., the focal length) from the metasurface to the focal plane is measured to be $300\mu\text{m}$ which precisely matches with our design value of $300\mu\text{m}$. Figure 4.4(b) shows the focusing process from the $5\mu\text{m}$ (Z in negative value) in front of the focal plane to the $5\mu\text{m}$ (Z in positive value) behind the focal plane.

For measuring the light utilization efficiency of our metasurface, the incident laser power P_0 is firstly measured at the rear surface of the metasurface, and then the laser power P_1 arrived at the focal plane is measured. The light utilization efficiency of P_1/P_0 is measured to be 31%. Note that the laser beam width is adjusted to match the diameter (1.2mm) of our metasurface, and the CCD is changed to be a power meter for measuring the powers. Notably, the overall light utilization efficiency (laser power at the focal point/incident laser power) of a metasurface-based optical levitation system is the metasurface's light utilization efficiency as there are no other components in the optical path. Therefore, by using the metasurface, the overall light utilization efficiency of an optical levitation system with tunable two optical traps could be improved to 31% from a SLM based system of 5%. In addition, the light utilization efficiency of the metasurface could be further improved by optimising the structural parameters of each cell, the materials, and the fabrication processing [43].

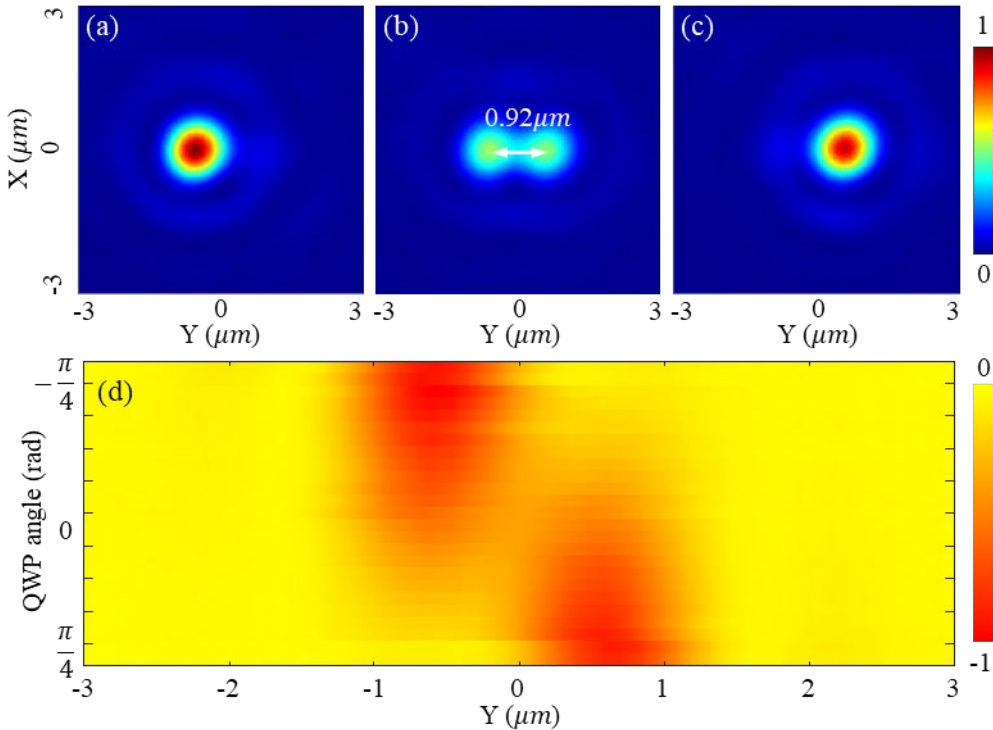


Figure 4.5 Optical intensity and potential wells of the metasurface sample 1.

Relative optical intensity (1st row) in the focal plane of the metasurface with a target distance D of $0.92\mu\text{m}$ when the incident laser beam is LCP (a), LP (b), and RCP (c). (d) shows the potential well's tunability with rotating a QWP over a Poincaré sphere.

To further evaluate the focusing performance of our metasurface, the Strehl ratio (S) of the sample is measured. As shown in Figure 4.4(c), the Strehl ratio of our sample is 0.89. According to the relationship $S = \exp [-(k\sigma)^2]$ between the Strehl ratio and the RMS wavefront error σ , where the $k=2\pi/\lambda$ is the wavenumber and wavelength $\lambda= 1550\text{nm}$, the RMS wavefront error is calculated to be 0.054λ , which meets the diffraction limitation criterion [87].

Figure 4.5 and Figure 4.6 show the optical intensity and relatively optical potential distributions of two samples (Figure 4.5(b): $D = 0.92\mu\text{m}$, and Figure 4.6(b): $D = 3.2\mu\text{m}$) when the incident laser beam is linearly polarized. Note that as the incident laser beam is not perfectly LP, the relative intensity of the two focal points is not precisely identical. As shown in Figure 4.5(b) and Figure 4.6(b), the real distance of the two samples is measured to be $0.92\mu\text{m}$ and $3.2\mu\text{m}$, which are almost equal to the designed values $0.9\mu\text{m}$ and $3.15\mu\text{m}$. According to the intensity distribution shown in Figure 4.5(a), the full width of half maximum (FWHM) of the focal points are measured to be 930nm, which corresponds to a NA of 0.9. Comparing Figure 4.5(d) and Figure 4.6(d), the central depth of the $0.92\mu\text{m}$ sample is shallow, while that of the $3.2\mu\text{m}$ sample is high enough for isolating the potential into two wells and trapping 2 particles for simultaneously levitating two particles at each focal point.

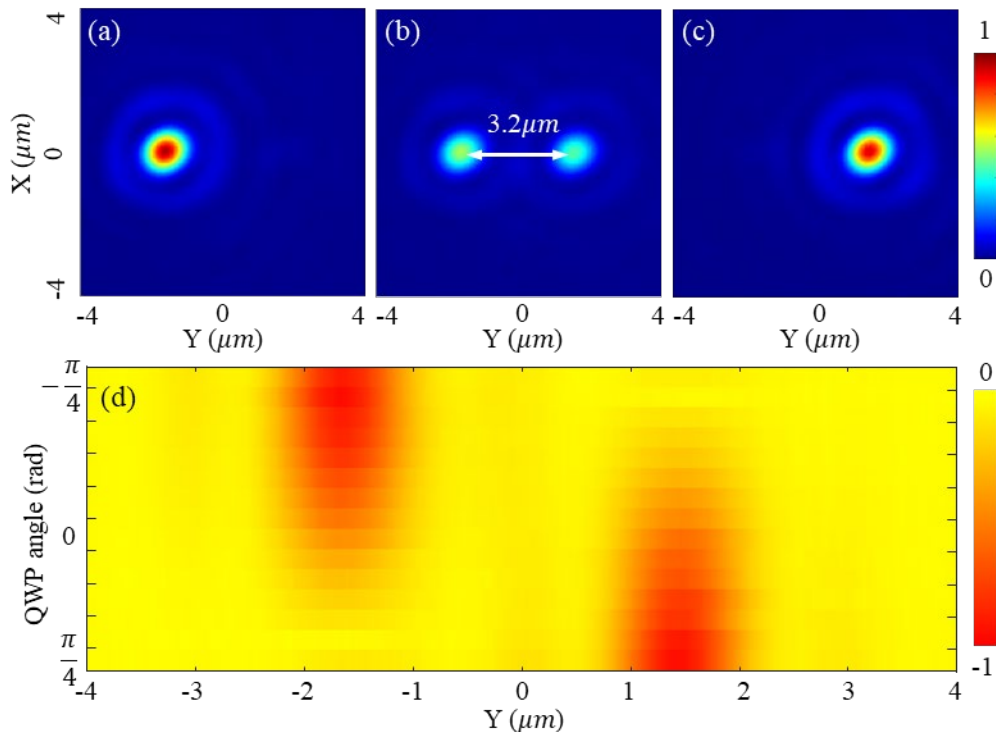


Figure 4.6 Optical intensity and potential wells of the metasurface sample 2.

Relative optical intensity (1st row) in the focal plane of the metasurface with a target distance D of $3.2\mu\text{m}$ when the incident laser beam is LCP (a), LP (b), and RCP (c). (d) shows the potential well's tunability with rotating a QWP over a Poincaré sphere.

The incident laser beam is tuned to be LCP and RCP for determining the focusing performance of the metasurface and demonstrating the tunability of two focal points' relative intensity and potential wells. The polarization is manipulated by changing the QWP angle in the experiment (Figure 3.5). When the QWP angle equals to $-\frac{\pi}{4}$, 0, and $\frac{\pi}{4}$, focal field's intensity distributions of the $0.9\mu\text{m}$ and $3.2\mu\text{m}$ samples are measured and shown in Figure 4.5(a-c) and Figure 4.6(a-c),

respectively. By changing the QWP angle from $-\frac{\pi}{4}$ to $\frac{\pi}{4}$, the left focal point's intensity goes down, and the right one's intensity goes up. When the QWP angle equals 0, two focal points with identical intensity are obtained. It indicates that the relative intensity could be well controlled by the QWP angle. As the optical trapping potential well's depth is linearly scaled with the intensity of the focal point [Eq. (4.2)], two tunable trapping potential wells are obtained in the experiment. As shown in Figure 4.5(d) and Figure 4.6(d), the optical potential well gradually evolves with rotating the QWP. As the QWP is rotated from $-\frac{\pi}{4}$ to $\frac{\pi}{4}$, the potential wells are a function of polarization state over the fundamental Poincaré sphere, which will be theoretically explained in following.

Based on the coordinate system shown in Figure 3.5, the Jones matrix of the incident laser beam can be expressed as $\begin{bmatrix} \cos\beta \\ -i\sin\beta \end{bmatrix}$, where β is the QWP angle. As a result, the amplitudes of LCP and RCP components are $[(\cos\beta - \sin\beta)/\sqrt{2}]$ and $[(\cos\beta + \sin\beta)/\sqrt{2}]$. Correspondingly, the intensities of LCP and RCP components can be expressed as $[1 - \sin(2\beta)]I_0/2$ and $[1 + \sin(2\beta)]I_0/2$, where I_0 means the total intensity of the incident laser beam. Therefore, the intensity of the LCP component (i.e., the left focal point) would go down from I_0 to zero with the angle β changing from -45° to 45° , while the intensity of the RCP component ((i.e., the right focal point)) goes up to a maximum value I_0 from zero. According to Eq. (4.2), the potential well linearly scales with the intensity distribution. Therefore, the potential wells generated by the metasurface can be tuned correspondingly.

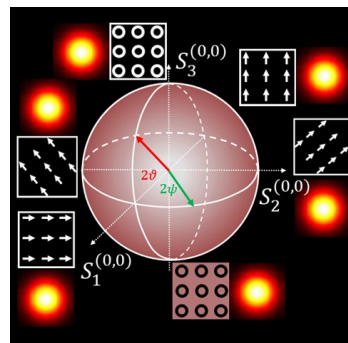


Figure 4.7 Polarization state over the fundamental Poincaré sphere.

The tune process of the laser beam's polarization state can be demonstrated by the fundamental Poincaré sphere (Figure 4.7) [40]. The three axes of the sphere denote the Stroke parameters S_1 , S_2 , and S_3 of the light beam's polarization state, which will be explained in Chapter 6. Especially, with the light beam's polarization being tuned from LCP to RCP, the beam's position on the Poincaré sphere varies to the Northern pole from the Southern pole. Correspondingly, the $S_3 = A_R^2 - A_L^2 = \sin(2\theta)$ evolves from -1 to 1. In experiment, the intensity A_R^2 of the RCP component is $[1 + \sin(2\beta)]I_0/2$, and the intensity A_L^2 of the LCP component is $[1 - \sin(2\beta)]I_0/2$. Therefore,

$2\vartheta = 2\beta$ can be obtained, which means that the relative intensity and potential well depth can be seen as a function of the polarization state and be tuned over a Poincaré sphere with rotating a QWP from $-\frac{\pi}{2}$ to $\frac{\pi}{2}$.

4.4 Dual-traps and levitation

4.4.1 Trapping stiffness and potential well

To theoretically evaluate the focal point's trapping stability and obtain the trapping stiffness, the optical force applied on a silica nanosphere with a radius of 100 nm is calculated based on the Maxwell stress tensor method using Lumerical FDTD software [88-90]. In simulation, the incident laser beam is set to be circularly polarized and all light energy is focused to the one focal point as shown in Figure 4.8(a). The incident laser power is set to be 180mW to match the simulation results with experiment data. Figure 4.8(b) shows the calculated optical force (black solid curve, left axe) and potential well (yellow solid curve, right axe). The horizontal axe y_A of Figure 4.8(b) denotes the deviation of the trapped particle's position to the focal point's centre [i.e., the y_{10} in Figure 4.8(a)].

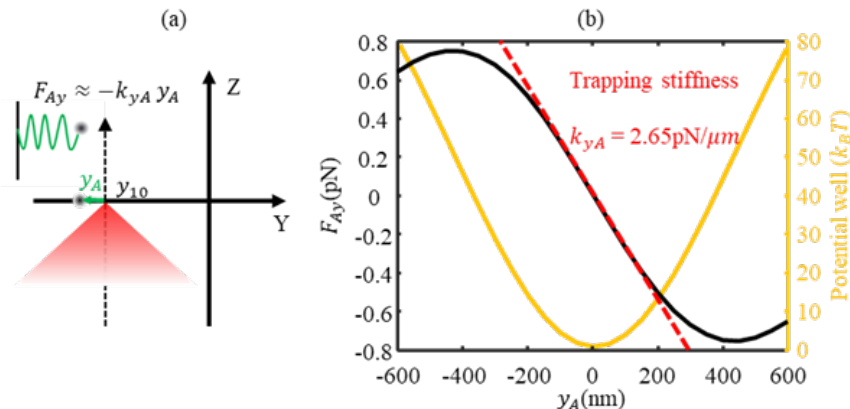


Figure 4.8 Simulated trapping stiffness and force.

(a) Optical trapping model of single focal point; (b) trapping force and potential well.

When the deviation y_A is within ± 150 nm, the radial trapping force F_{Ay} can be approximated by a linear function of the deviation y_A (i.e., $F_{Ay} \approx -k_{yA} y_A$), which means that the trapped particle experiences a spring force [red dashed line in Figure 4.8(b)]. Therefore, the motion of the trapped particle can be regarded as an optically driven spring-mass type of optomechanical oscillator, where the spring constant $k_{yA} = 2.65 \text{ pN}/\mu\text{m}$ is the slope of the trapping force over the linear region. The spring constant k_{yA} is also called trapping stiffness, which is a key factor for evaluating the trapping stability.

In addition to the trapping stiffness, the trapping well potential energy should be beyond $10 k_B T$ (k_B is the Boltzmann constant, and T is ambient temperature 300K) for stable trapping [1, 2]. Therefore, the trapping potential well of the focal point is calculated and demonstrated in yellow solid curve in Figure 4.8(b), which demonstrates that the focal point could provide a trapping well with a depth of $80k_B T$. While $80k_B T$ is smaller than the potential well depth of $89k_B T$ obtained in Figure 4.3(a), the theoretical values of potential well depth in Figure 4.3 coincide well with the numerically simulated values in Figure 4.8(b) because the potential well depth is linearly scaled down with reducing the incident laser power. With tuning the incident light beam to be linearly polarized, the light energy would be equally split to two focal points. As a result, the trapping potential well depth of each focal point would be reduced to $40k_B T$, and the trapping stiffness k_{Ay} / k_{By} of each focal point would be reduced to $1.325 \text{pN}/\mu\text{m}$. Therefore, the focal points generated by the metasurface can be used for stably trapping a nanoparticle.

4.4.2 Optical levitation experiment

In following, a setup is built to verify the metasurface sample's optical levitation ability in free space. As the red dashed line shown [Figure 4.9(a)], the collimated 1550nm laser beam is introduced into the rear surface of the fabricated metasurface and then is collected by an objective lens (NA=0.9) for alignment and imaging of the focal points by a 1500-1600nm NIR CCD (fluorescence based). The 1550nm laser beam is for trapping particles. In addition, a fibre-based polarization controller is introduced to manipulate the beam's polarization. For imaging the levitated particles, as the green dashed line shown in Figure 4.9(a), a green laser beam (520nm) is introduced to the focal plane of the metasurface, and the green laser beam is scattered by the levitated particles, collected by the objective lens, and imaged by a visible CMOS camera. A long-pass dichroic mirror (550nm cut-on wavelength) is placed behind the objective lens to split the 1550nm trapping laser and the 520nm detection laser beams.

In the experiment, the optical path of the 1550nm laser is first aligned by checking the focal point's images via the 1550nm imaging system. The brightest image with a circular profile (shown in Figure 4.9(b1 and c1)] can be obtained when the optical path is aligned well enough. At this time, the focal planes of the metasurface and the objective lens are coincided at the same plane at 1550nm. Otherwise, the image would be blurred by the misalignment (e.g., coma and defocus aberrations). Then, the metasurface is moved forward to the objective lens by $300\mu\text{m}$ (i.e., the focal length of the metasurface) via a precision translation stage, and the functional surface (i.e., the former surface) of the metasurface is moved to the focal plane of the objective lens, which plays an important role for aligning the optical path of 520nm laser.

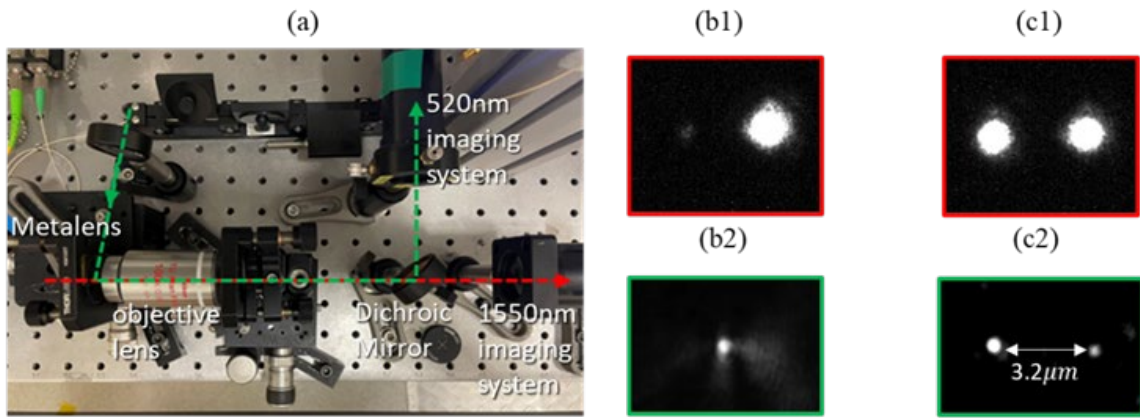


Figure 4.9 Optical levitation of two nanoparticles.

(a) Optical levitation setup. (b) and (c) are the images of the metasurface's focal points (1st row) and levitated particles (2nd row) when the incident laser beam is RCP and LP, respectively.

The 520nm laser beam is introduced (i.e., the incident angle is almost equal to 90 degrees) to the functional surface of the metasurface, and the nanostructure of the functional surface can be imaged by the Thorlabs CMOS camera because of the scattering effect. Next, the position of the metasurface is slightly translated from the 1550nm focal plane to obtain the best image from the chromatic aberration of the objective lens. The functional surface of the metasurface is located at the focal plane of the objective lens at 520nm. Finally, the metasurface is moved backwards from the objective lens by $300\mu\text{m}$, and the 1550nm focal plane of the metasurface is moved to the 520nm focal plane of the objective lens, which is essential for imaging the levitate particles [Figure 4.9(b2 and c2)].

The 1550nm trapping laser beam (180mW) is firstly manipulated to be RCP, and a single focal point is measured by the 1550nm imaging system. Then, the solution with 100nm nanoparticles is sprayed to the region between the metasurface and the objective lens via a nebulizer. Before a particle is trapped by the focal point, the image captured by the 520nm imaging system is fully dark, and then a bright spot [Figure 4.9(b2)] appears on the image demonstrating that a particle is trapped by the focal point. As this experiment is done in free space, it means that the particle is stably levitated by the focal point. In another experiment, a particle is stably levitated in air for more than three hours.

To verify the levitation ability of 2 particles at the same time, the 1550nm trapping laser beam (180mW) is tuned to be LP, and two focal points [Figure 4.9(c1)] are captured by the 1550nm imaging system correspondingly. As the particles are loading via a nebulizer, it takes some time for particles to be trapped by the focal points since they are sprayed out. Figure 4.9(c2) shows that two particles are trapped at the same time, which demonstrates that our metasurface-based

optical levitation system could be used for simultaneously levitating two particles and studying optical coupling effect in the experiment.

It is difficult to simultaneously trap two particles at the focal plane as shown in Figure 4.9(c2). In general, only one particle can be trapped by one of the two focal points at one time. In addition, the trapped particles in Figure 4.9(c2) are not identical in shape and size which makes it difficult to directly studying the dynamics of levitated particles. It is well known that these two problems are caused by the nebulizer-based loading method. In future, we'll focus on optimising the particle loading method and moving the setup into a vacuum chamber to explore the optical levitation dynamics ranging from nonlinear duffing equation to coupled oscillators.

4.5 Optical coupling dynamics

It is demonstrated that the metasurface-based optical traps can simultaneously levitate two particles in free space in experiment. Meanwhile, the two particles behave like two oscillators with spring constants k_{Ay} and k_{By} , respectively, as shown in Figure 4.10(a). In following, the optically coupled dynamics of the two levitated particles will be analysed in simulation. In simulation, the incident laser beam is linearly polarized and has a power of 180mW. As the spring constant of the optical force is proportional to the focal point's intensity [3,20]. Therefore, the ratio between $k_{Ay} \propto [1 - \sin(2\beta)]I_0$ and $k_{By} \propto [1 + \sin(2\beta)]I_0$ can be tuned via controlling the QWP angle β . k_{Ay} will be close to k_{By} when the two focal points have the same intensity distribution under the assumption that the two particles are similar.

Because the light scattered by particle A would exert a force on particle B and vice versa, the two particles A and B levitated at a close distance would be coupled [Figure 4.10(a)], which is generally called optical binding [16, 18]. The mutual force and coupled motion are termed as an optical binding force and optical binding dynamics. As the distance D could be precisely tailored and varied from zero to several micrometres in experiment, the metasurface can be utilized to explore different lateral optical binding dynamics.

In the following, we concentrate on the ideal case where two focal points (i.e., trapping centres) have an equal intensity distribution. As a result, the driven and damped dynamics of the coupled oscillators A and B can be described by a Langevin equation Eq. (4.4) including the stochastic effect of collisions with residual gas particles in the environment of the trapped particles [27],

$$mA_{11} \frac{d^2}{dt^2} \begin{pmatrix} y_A \\ y_B \end{pmatrix} + \frac{d}{dt} \begin{pmatrix} y_A \\ y_B \end{pmatrix} = \begin{pmatrix} A_{11} & A_{12} \\ A_{12} & A_{11} \end{pmatrix} \begin{pmatrix} F_A(t) - k_{Ay}y_A + F_{ob}(y_B) \\ F_B(t) - k_{By}y_B + F_{ob}(y_A) \end{pmatrix} \quad (4.4)$$

where y_A (or y_B) is the deviation of the particle A (or B) from its equilibrium position y_{10} (y_{20}) (Figure 4.10), $A_{11} = 1/(6\pi\mu a)$ and $A_{12} = 1/(4\pi\mu D)$ are the longitudinal mobility factors with μ the residual gas viscosity. $f_A(t)$ and $f_B(t)$ are the force noise terms, the term $k_{Ay}y_A$ (or $k_{By}y_B$) represent the restoring spring force on particle A (or B) when particle A (or B) is displaced away from its equilibrium trapping position, and the other particle B (or A) is kept at a fixed position. The term $F_{ob}(y_B)$ [or $F_{ob}(y_A)$] is the optical binding force acting on particle A (or B) at its equilibrium position when particle B (or A) is displaced.

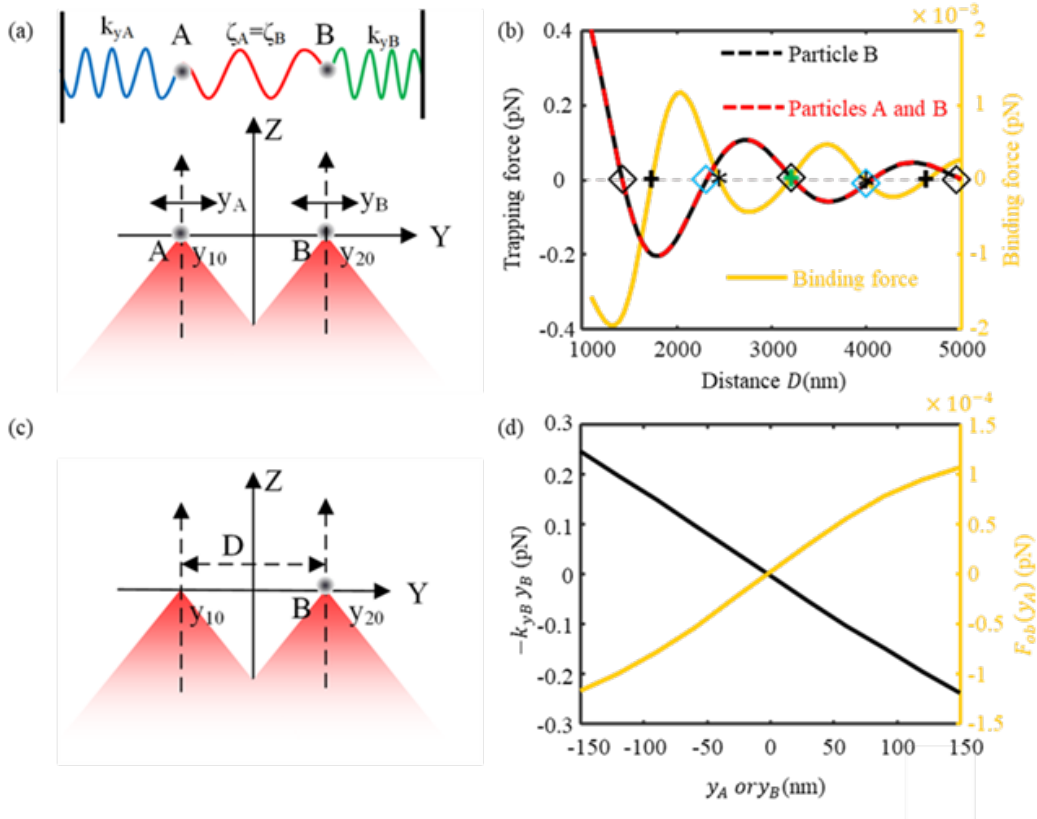


Figure 4.10 Optical coupling model and dynamics.

(a) and (c) models for calculating optical binding forces; (b) optical force and binding force vs distance D ; (d) Spring optical force ($k_{By}y_B$) and optical binding force [$f_{ob}(y_A)$] on particle B.

The optical binding force on particle B can be obtained by subtracting the optical force applied to particle B when there is no particle trapped in another trapping centre [Figure 4.10(c)] from the total optical force exerted on particle B when particle A is trapped in the trapping centre [Figure 4.10(a)]. Eq. (4.4) shows that the dynamical behaviour relies on the restoring force $k_{Ay}y_A$ and $k_{By}y_B$ as well as the optical binding force F_{ob} . It has been proven that, in a coupled oscillation system, non-reciprocal dynamics and localization of the oscillation mode can be realized by modulating the conservative - restoring force - and nonconservative - optical binding force - terms, which could be used for enhancing sensitivity in detecting weak force or torque [33, 75, 91]. The tunability of the nonconservative coupling force, the optical binding force, would be

discussed in the following to show our metasurface' potential application in constructing an on-chip optical binding system with non-reciprocal dynamics or localization of the oscillation mode.

The red dashed curve (left axis) in Figure 4.10(b) shows the total force applied to particle B when both particles A and B are placed at the trapping centres [Figure 4.10(a)], and the black dashed curve shows the optical force when no particle is trapped in trapping centre A [Figure 4.10(c)]. As the two curves shown, the optical force applied to particle B shows spatial periodicity. In addition, the black curve is nearly identical to the red one, which means that the optical binding force is small, and the motion of the trapped particle is dominated by the total trapping force. The diamond shapes in [Figure 4.10(b)] marks the distance D where the total trapping forces are null. Considering the optical force's direction and the relative position between particles A and B, particle B would be pushed back to the trapping centres (i.e., the focal point) by perturbing the distance D at the points marked by black diamond shapes. Therefore, they are stable trapping centres. In contrast, particle B would be pushed away from the trapping centres for the distance D marked by blue diamond shapes. Therefore, they are not stable trapping centres.

As the yellow curve (right axis) shown in Figure 4.10(b), the optical binding force also shows the spatial periodicity, which is generally called long-range oscillation of optical binding force and arises from the combination of the scattering field from particle A and the focal field around particle B and. In magnitude, the optical binding force is much smaller than the total trapping force and would decay with the increase of D , which means that two trapped particles are weakly coupled by the optical binding force.

In addition, 5 zero points are marked on the red curves in Figure 4.10(b). It means that the optical binding force at these points is null. At the points marked by an asterisk, the optical binding force is linearly proportional to the perturbation of distance D but with a negative slope, which indicates that particle A exerts an attractive optical-binding force on particle B. In contrast, the optical binding force is linearly proportional to the perturbation of distance D with a positive slope, at the points marked by the cross, which indicates that the optical binding force is repulsive. Around the peaks of yellow curve, the optical binding force would be nonlinear when perturbing the distance D . Therefore, tailoring the distance D could realize different coupling characteristics, like linear and nonlinear coupling [27, 31, 92].

When two trapped particles are trapped and optically coupled, their motion is a small oscillation around their trapping centres. Therefore, to analyse the coupled dynamics, the dependency of the optical binding force [i.e., coupling forces $F_{ob}(y_A)$, $F_{ob}(y_B)$] on small deviations y_A and y_B should be studied in detail.

Considering that the total optical trapping force and the optical binding force are linearly proportional to the perturbation of distance D at $D = 3231.8\text{nm}$ [marked by the green cross and black diamond in Figure 4.10(b)], the distance D is fixed at 3231.8nm to realize the linearly coupled dynamics [i.e., $f_{ob}(y_A) \propto \zeta_A y_A$, $f_{ob}(y_B) \propto \zeta_B y_B$]. This is the reason why the metasurface sample with a distance D of $3.2\mu\text{m}$ is experimentally characterised in detail ranging from optical focusing performance to levitation ability of two particles in free space. In addition, considering the symmetry ($\zeta_A = \zeta_B$, $k_{Ay} = k_{By}$) of this system under the assumptions that two focal points' intensity distribution and trapped particles are identical, only the forces exerted on particle B [i.e., $-k_{By}y_B$ and $F_{ob}(y_A)$] are calculated and shown in Figure 4.10(d).

As the black curve (left axe) shown in Figure 4.10(d), when particle A is fixed, the optical force exerted on particle B linearly goes down with its displacement y_B . Therefore, the optical force could be simply expressed by the term $-k_{By}y_B$ ($k_{By} > 0$) in Eq. (4.4). The minus sign means that the optical force is a restoring force. As the yellow curve (right axe) shown in Figure 4.10(d), when particle B is fixed at its equilibrium position, the optical binding force $F_{ob}(y_A)$ is positively proportional to the small displacement y_A of particle A. Therefore, $F_{ob}(y_A)$ in Eq. (4.4) could be simplified to $\zeta_B y_A$ ($\zeta_B > 0$). As a result, two particles are linearly coupled and could be seen as two coupled oscillators via three springs, as shown in Figure 4.10(a).

In addition, as the intensity of two focal points could be modulated, the symmetry between the two particles' motion is broken when the intensity distributions of the two focal points are not identical. As a result, ζ_A is not equal to ζ_B , and spring constant k_{Ay} is not equal to k_{By} . Then, more complicated dynamical behavior could be realized based on the proposed metasurface.

4.6 Conclusion

This chapter proposed a scalable on-chip platform for realizing tunable optical potential wells of two trapped particles via a metasurface working in the classical spin-multiplexing regime. Based on the metasurface, one incident laser beam can be directly focused to two diffracted-limitation focal points with high light utilization efficiency (31%) and high NA (0.9). Benefiting from the application of this metasurface, there are no other optical components in the whole system, which results in the overall light utilization efficiency of one metasurface-based optical levitation system being improved to 31%. It is illustrated that the distance and relative intensity as well as the relative potential wells could be well tailored and finely controlled in both simulation and experiment. It is experimentally demonstrated the fabricated metasurface sample could be used for stably levitating one or two particles for several hours.

Chapter 4

Based on the general Langevin equations and the numerically obtained optical binding force, it is analysed that the metasurface sample could provide different dynamical behaviours of two coupled particles. Specifically, different optical trapping force and binding force profiles could be potentially realized by tailoring the distance between two focal points because of the long-range oscillation. As a result, the proposed metasurface-based levitated optomechanical system could be used for constructing levitated force and torque sensors with ultra-high sensitivity and accuracy by using varieties of coupling dynamics.

Chapter 5 Near-infrared metasurface empowered dual-mode microscope

5.1 Introduction of dual-mode imaging

Bright field microscope is widely used for imaging the overall morphologies of amplitude objects. However, the bright field microscope cannot provide clearly distinguished morphological information of the transparent objects (i.e., low index contrast objects) [5, 93]. To realize high-contrast and edge-enhanced imaging of phase objects, a phase contrast microscope is initially introduced by the Dutch physicist Frits Zernike in the 1930s [93]. Compared with algorithm-based edge enhancement in image processing, a phase contrast microscope is an all-optical processing and could provide direct edge detection functionality [55]. This technique is employed to generate high-contrast images of transparent specimens, including living cells (typically in culture), unstained biological samples, and microorganisms and is widely used for low optical contrast specimens [94].

Essentially, a phase contrast microscope is based on filtering image information in its Fourier plane (i.e., frequency domain). As the spiral phase filtering function can lead to a 2-dimensional (2D) isotropic edge-enhancement effect of observed amplitude and phase objects, the spiral phase contrast microscope has been implemented in many ways. Conventionally, the spiral phase contrast microscope is implemented by generating a spiral phase profile in the Fourier plane of a 4f filtering system via a spatial light modulator (SLM), which makes the microscope system too bulky and limits the resolution and FOV [58, 95].

In recent years, metasurface being made of an array of subwavelength nanofins has attracted a lot of attention in the imaging community because of its powerful ability to manipulate amplitude, phase, and polarization of incident light [11, 13, 53, 96]. A transmissive dielectric metasurface working as a polarization-controlled phase filter is placed in the Fourier plane of a 4f system for realizing switchable spiral phase contrast imaging [69]. Additionally, some reflection configurations based on reflective metasurface are proposed as well [97, 98]. However, the multiple lenses used in both 4f filtering system or reflection configuration result in a complex and bulky optical system, which fails to exploit the multi-functional merit of a metasurface and hinders the miniaturization of the spiral phase contrast imaging system.

A single-lens spiral phase contrast imaging configuration was achieved by compressing the imaging and edge-enhancement functionalities into transmissive metasurface in the visible spectrum [5]. However, the metasurface can only work in the phase-contrast imaging mode, which

limits its application in bright field imaging mode. Recently, a dielectric metasurface has been proposed for synchronous spiral phase contrast and bright field imaging [99], and an electrically tunable dual-mode metalens is reported for switchable spiral phase contrast and bright field imaging [54]. However, the former one has one small imaging FOV ($\sim 50\mu m \times 50\mu m$), and the latter one has a low resolution ($\sim 3\lambda$) and low edge-enhancement quality. There is no report on the switchable dual-mode (i.e., bright field and phase contrast) microscope with high resolution, large magnification, and large FOV. While the above metalenses work in the visible spectrum, the near-infrared (NIR) spectrum is attracting increasing attention in biological research, machine vision and semiconductor inspection because of several advantages. Firstly, the NIR light wave can penetrate through the biological tissue deeper than visible light. Secondly, the visible auto-fluorescence of cells and tissues is considered as the main source of background noise in biological imaging, imaging in NIR can achieve a higher signal-to-noise ratio [100,101]. Finally, the NIR microscopy provides defect information on the silicon chips compared to visible light for semiconductor inspection.

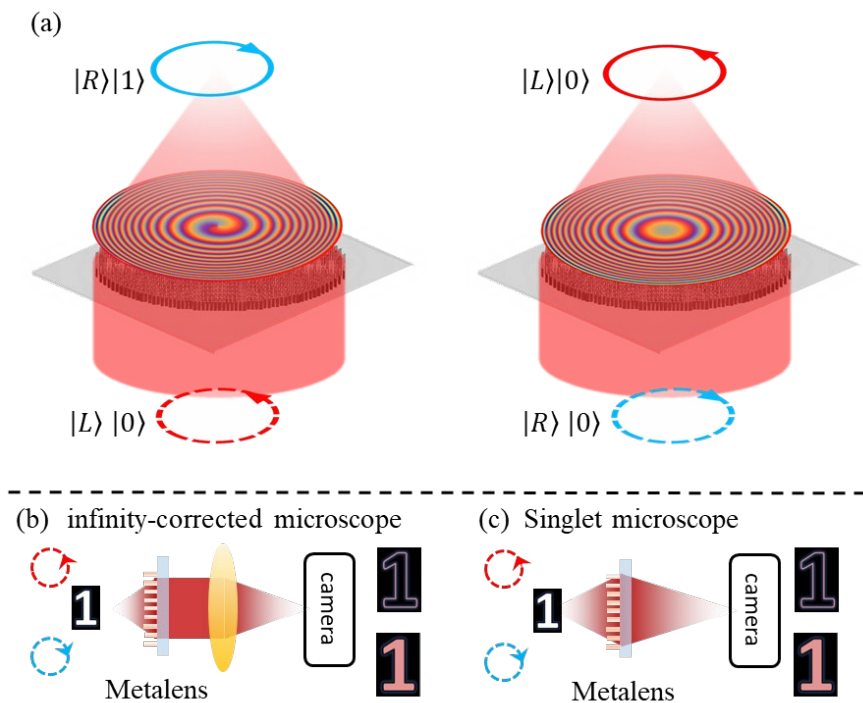


Figure 5.1 Conceptual figure of dual-mode imaging.

(a) Conceptual scheme of polarization-controlled focusing mode. Metalens-based infinity-corrected microscope (b) and singlet microscope (c) for polarization-controlled phase contrast imaging and bright field imaging.

This chapter proposes a NIR single-layer dielectric metalens where the phase profile can be tuned from a hyperbolic phase to a sum of a hyperbolic phase and a spiral phase with a topologic charge of 1, as shown in Figure 5.1. In the wavelength of 1550nm, the metalens can focus the LCP light

beam to a donut ring with a topologic charge of 1 for phase contrast imaging mode and focus the RCP light beam to a Gaussian focal point for bright field imaging. Taking these advantages, two polarization-controlled dual-mode imaging systems are demonstrated in the NIR imaging window.

5.2 Metalens design and characterization

To realize dual-mode focusing and imaging, the metalens sample is designed in the classical spin-multiplexing regime again. Therefore, a nanofins library including 8 cells (Table 5.1) is built up based on the sweeping results shown in Figure 2.2.

Table 5.1 Nanofins library for dual mode focusing metalens.

L (nm)	W (nm)	ϕ_x (π)	ϕ_d (π)
140	600	-0.79	1
200	440	-0.67	1
220	480	-0.47	1
260	480	-0.11	0.94
500	160	0.16	0.93
560	160	0.32	1
500	220	0.62	1.1
500	260	0.92	0.99

As shown in Figure 5.1(a), to realize phase contrast imaging mode, the metalens impart a sum phase profile [Eq. (5.1)] of the hyperbolic phase and the spiral phase with a topological charge of 1 on the LCP light beam. A hyperbolic phase profile [Eq. (5.2)] is imparted onto the RCP light beam to realize bright field imaging mode. Therefore, the metalens in a microscope system can serve as an imaging lens and a polarization-controlled phase plate as shown in Figure 5.1(b) and Figure 5.1 (c).

$$\Phi_L(\rho, \varphi) = \frac{2\pi}{\lambda} \left(f - \sqrt{f^2 + \rho^2} \right) + \varphi \quad (5.1)$$

$$\Phi_R(\rho, \varphi) = \frac{2\pi}{\lambda} \left(f - \sqrt{f^2 + \rho^2} \right) \quad (5.2)$$

Following the design procedure in section 2.3 and the fabrication flow in Figure 3.4, two a-Si metalens samples are designed and fabricated. The first metalens [Figure 5.2(a)] has a diameter of 4mm, a NA of 0.89, and a focal length f of 1mm. The second metalens [Figure 5.2(d)] has a diameter of 4mm, a NA of 0.25, and a focal length f of 8mm. Figure 5.2(g) demonstrates the SEM image of metalens sample 1.

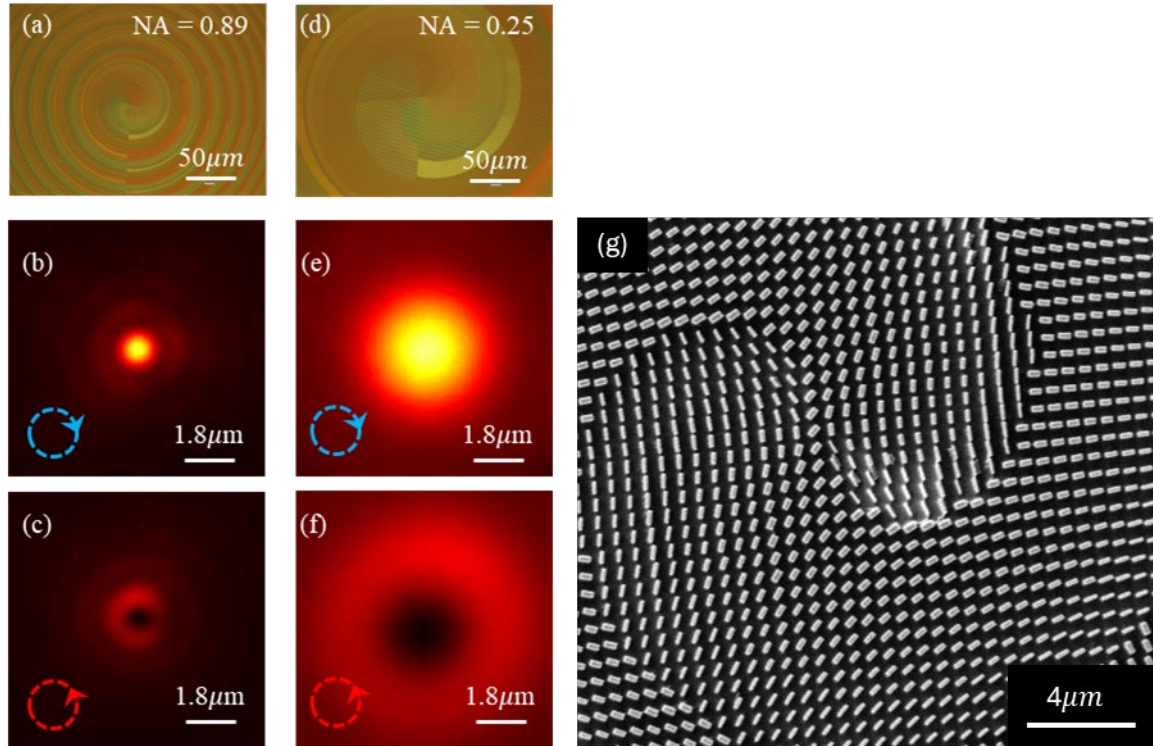


Figure 5.2 Characterization of metalens samples.

The (a) – (c) are the optical image, Gaussian focal point, and donut-shaped focal point of the metalens sample 1 (NA = 0.89), respectively; (d) – (f) are the optical image, Gaussian focal point, and donut-shaped focal point of the metalens sample 2 (NA = 0.25), respectively; (g) SEM image of sample 1.

The fabricated metalens samples are measured by the home-customized microscope (Figure 3.5) a magnification of 100X and a NA of 0.9 to characterize the polarization-controlled focusing ability. The Gaussian focal point is first measured to evaluate the NA of two samples under the RCP beam illumination. The FWHM of sample 1 is measured to be $1.1 \mu m$, shown in Figure 5.2(b), which demonstrates that sample 1 has a NA of 0.89. The FWHM of sample 2's Gaussian focal point is $3.8 \mu m$ corresponding to a NA of 0.25, Figure 5.2(e). These results indicate that two diffraction-limited Gaussian focal points are obtained by illuminating samples 1 and 2 via an RCP light beam. As shown in Figure 5.2(c) and Figure 5.2(f), the two Gaussian focal points can be tuned to be two donut rings by tune the illumination light beam to be LCP via rotating the QWP (Figure 3.5). The donut ring of sample 1 has a radius of $1.6 \mu m$, and the donut ring of sample 2 has a radius of $5.7 \mu m$, respectively.

To realize a large-magnification (58X) and a high-resolution (0.7λ) dual-mode imaging system, an infinity-corrected microscope in Figure 5.1(b) is demonstrated by utilizing the metalens sample 1 as a high-NA (0.89) objective lens (section 5.3.1), and a second infinity-corrected dual-mode microscope with large FOV ($600\mu m \times 800\mu m$) and a diffraction-limited imaging resolution ($0.61\lambda/NA$) is demonstrated by utilizing the metalens sample 2 as the objective lens (section 5.3.1). Finally, a singlet dual-mode microscope system in Figure 5.1(c) is demonstrated via the metalens sample 2 (section 5.3.3).

5.3 Compact dual-mode imaging experiments

5.3.1 High-resolution and large magnification microscope

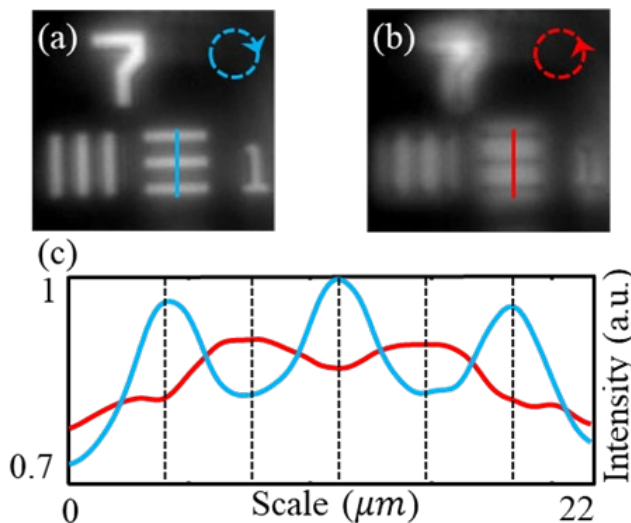


Figure 5.3 Imaging results of 58X microscope.

(a) and (b) show the bright-field image and edge-enhanced imaging obtained via the 58X infinity-corrected microscope, and (c) demonstrates the intensity curve.

An infinity-corrected microscope in Figure 5.1(b) is constructed by utilizing the metalens sample 1. The metalens serves as a high-NA (0.89) objective lens and polarization-controlled phase filter. A 1550nm LED light source (Thorlabs, M1550L4) is used for illuminating a USFA 1951 resolution target (Thorlabs, R1DS1N), and a cemented achromatic doublets lens (Thorlabs, AC254-060-C) with a focal length of 60mm is adopted as the tube lens. One polarizer and QWP are placed between the light source and the resolution target to manipulate the illumination light's polarization state. The image is captured by an InGaAs camera.

Figure 5.3(a) and Figure 5.3(b) show the bright-field image and edge-enhanced image of element 1 in group 7, respectively. the transition process of the imaging mode between bright-field and edge-enhanced phase contrast imaging mode can be clearly observed with rotating the QWP. To

quantitatively demonstrate the transition of imaging mode, the intensity along the blue and red lines in Figure 5.3(a) and Figure 5.3(b) are depicted in Figure 5.3(c), which demonstrates the intensity peaks are tuned to the intensity valley with the imaging mode being tuned from bright-field to phase contrast imaging mode. According to the real dimension of element 1 in group 7, the magnification of our compact dual-mode microscope is calculated to be 58 times (i.e., 58X). As shown in Figure 5.4(a) and Figure 5.4(b), the bright-field image and edge-enhanced image of the USAF element 6 in group 7 indicate that the microscope could effectively resolve a feature size around $1\mu m$ in both bright field and phase contrast imaging mode, which means the microscope has a diffraction-limited sub-wavelength resolution ($0.61\lambda/NA = 0.7\lambda = 1.1\mu m$) at the wavelength of 1550nm. However, limited by the sensor size of the InGaAs camera, this microscope can only provide us with a small FOV ($80\mu m \times 108\mu m$) in this configuration.

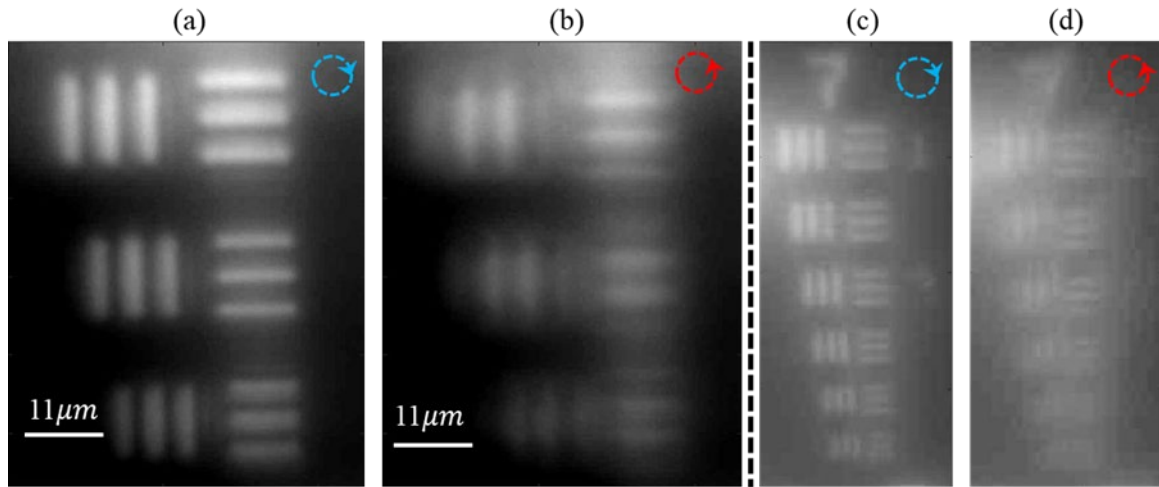


Figure 5.4 Resolution test of infinity-corrected microscope.

The bright-field image (a) and edge-enhance image (b) of elements 4-6 of group 7 obtained via the 58X microscope (section 5.3.1); The bright-field image (c) and edge-enhanced image (d) of the group 7 obtained via the 7.8X microscope (section 5.3.2).

5.3.2 Diffraction-limited resolution and large FOV microscope

By using the metalens sample 2 with a focal length of 8 mm and NA of 0.25 in the custom build microscope (section 5.3.1), the FOV of $600\mu m \times 800\mu m$, diffraction-limited image resolution, and biological dual mode imaging ability is demonstrated. The imaging resolution and magnification of this microscope are firstly measured by capturing the dual-mode images of the group 7 in USAF resolution target. Figure 5.4(c) and Figure 5.4(d) respectively show the bright-field image and edge-enhanced image of the USAF group 7. Correspondingly, the imaging magnification and resolution of this microscope are calculated to be 7.8X and $3.78\mu m$ (i.e., diffraction limitation of the metalens sample 2, $0.61\lambda/NA=2.44\lambda$).

A freshly peeled and unstained onion epidermal is prepared for verifying the dual-mode imaging ability of the microscope in biological samples. As shown in Figure 5.5, the cell wall (i.e., the edge of cells) becomes clear [Figure 5.5(b)] from blurred [Figure 5.5(c)] in whole FOV ($600\mu m \times 800\mu m$) with the illumination light being tuned to be LCP from RCP. The edge-enhancement process can be clearly observed and captured by the camera. The intensity along the blue and red lines in Figure 5.5 are depicted in Figure 5.5(c) to show the edge-enhancement effect quantitatively. In theory, the FOV can be further enlarged by adopting a camera with a larger imaging sensor.

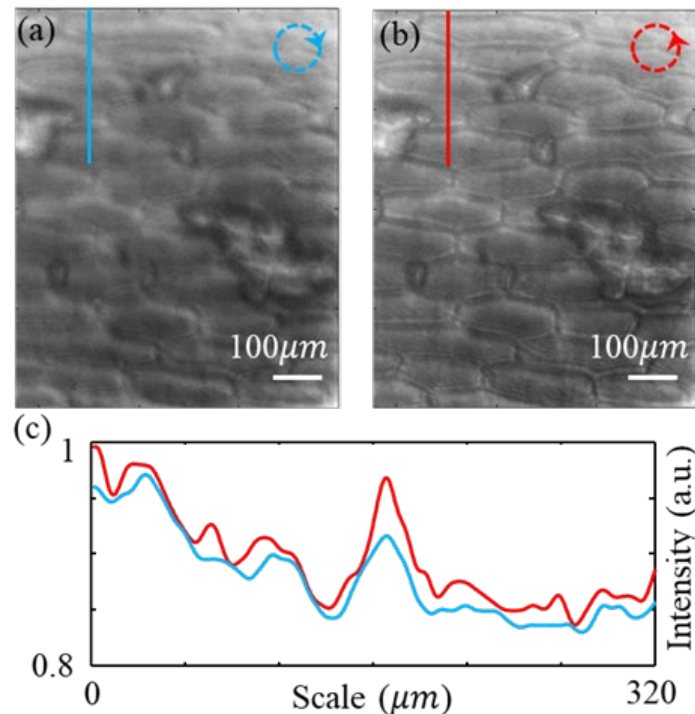


Figure 5.5 Imaging results of biological sample.

(a) and (b) show the bright-field image and edge-enhanced image obtained via the metalens-based 7.8X microscope, and (c) demonstrates the intensity curve.

5.3.3 Singlet dual-mode microscope for all-optical edge-detection

While edge detection plays an important role in a lot of industrial applications, the edge-detection is mostly achieved by post-processing of a bright-field image via software algorithms. The processing speed of current edge-detection algorithms highly depends on the computer hardware and software. If the edge-enhanced images of the target objects can be directly obtained based on an all-optics system, the edge detection can be operated in light speed, which would boost the industrial application. In addition, the imaging system should be simplified as much as possible to improve the system's robustness and reduce the cost. In the following, a singlet dual-mode microscope is demonstrated to realize all-optics edge-detection at 1550 nm wavelength.

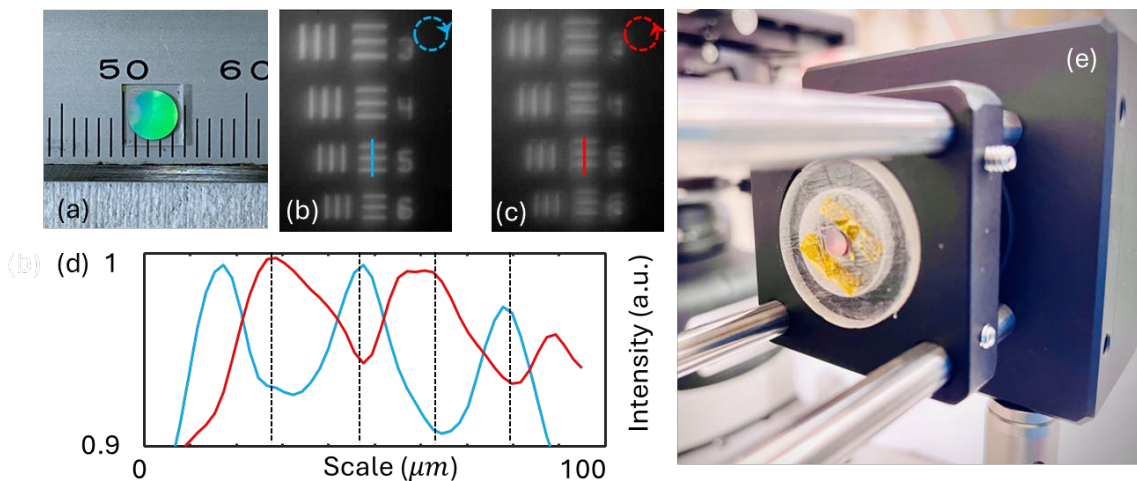


Figure 5.6 All-optics edge-detection experiment and results.

(a) metalens sample; (b) bright-field image and (c) edge-enhanced image obtained via the singlet dual-mode microscope; (d) is the intensity curve; (e) Experiment setup.

The metalens sample 2 [Figure 5.6(a)] is mounted 40mm in front of the InGaAs camera sensor (i.e., the imaging distance is 40mm) via a 3D-printed holder [Figure 5.6(e)]. The USFA 1951 resolution test target is placed 10mm in front of the metalens to get a clear image in the camera. Figure 5.6(b) and Figure 5.6(c) show the bright-field image and edge-enhanced image of the elements 3-6 in group 5, respectively. According to the real dimension of element 5 in group 5, the magnification of this singlet dual-mode microscope is calculated to be 4.2X. The intensity curves in Figure 5.6(d) demonstrate the intensity peaks are tuned to valleys with the imaging mode being tuned from bright-field to phase-contrast imaging mode. The transition process can be clearly observed via the camera. Therefore, an all-optics edge-detection system with a simple hardware configuration is achieved in this chapter.

5.4 Conclusion

The spiral phase contrast microscope can clearly distinguish the morphological information of the phase objects (i.e., biological samples) because of the isotropic edge-enhancement effect, while the bright field microscope can image the overall morphology of amplitude objects. However, the imaging resolution, magnification, and field of view of conventional spiral phase contrast microscopes based on $4f$ filtering configuration are limited by the system's complexity. This chapter studies compact dual-mode microscopes working at near-infrared using the engineered metalens which can be tune between the spiral phase contrast imaging and bright field imaging by polarization control. The metalens combines the high-resolution objective lens and polarization-controlled phase filter into a single-layer nanofins array. This chapter demonstrates two infinity-corrected microscope systems to achieve subwavelength resolution (0.7λ), large magnification (58X), and large field of view ($600\mu\text{m} \times 800\mu\text{m}$). Unstained onion

Chapter 5

epidermal is imaged by the microscope to show the dual-mode imaging ability for the biological sample. Finally, a singlet dual-mode microscope system is demonstrated to show the all-optics edge-detection application for industrial standards. These results could open new opportunities in applications of biological imaging, industrial machine vision, and semiconductor inspection.

Chapter 6 Metasurface for arbitrary HOPS and HyOPS beams

6.1 Introduction of HOPS and HyOPS beams

Structured light beam is attracting researchers' attention in many fields because of its powerful application potentials in classic and quantum fields ranging from laser communication, super-resolution imaging and lithography, multi-dimensional optical manipulation [20, 22, 48-50]. Vector vortex beam (VVB) as a special case of structured light beam owns spatially inhomogeneous state of polarization (SOP) and phase profile on its cross section, which makes it carry with orbital angular momentum and spin angular momentum [51].

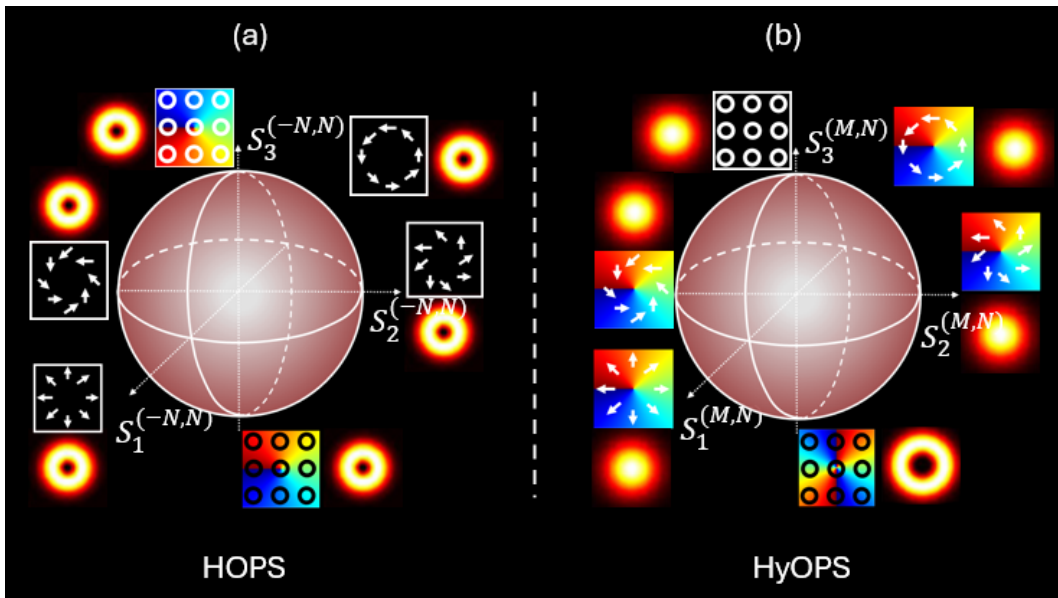


Figure 6.1 Conceptual figure of HOPS and HyOPS.

(a) HOPS, and (b) HyOPS. $S_1^{(N,M)}$, $S_2^{(N,M)}$, and $S_3^{(N,M)}$ are the strokes parameters of the beams, the superscript (M, N) denotes the topological charges carried by the LCP (southern pole) and RCP (northern pole) beams. When $M = -N$, the LCP and RCP beams are the vortex beams of same topological charge with opposite sign, and the HyOPS (c) is degraded to HOPS (b). Moreover, when $M = N = 0$, the LCP and RCP beams are plane waves, and the HOPS is degraded to a fundamental Poincaré sphere shown in Figure 4.7.

A theoretical framed named higher-order Poincaré sphere (HOPS) is developed to describe the VVB's total angular momentum and its evolution of SOP and phase profile, which provides researchers with great utility and convenience in analyzing the VVB [40]. As shown in Figure 6.1(a),

the two poles of HOPS represent two scalar vortex beams with spatially homogenous SOP (i.e., RCP and LCP) and vortex phase profile, which possesses a SAM of $\sigma\hbar$ ($\sigma = \pm 1$) and an OAM of $l\hbar$ (l is the orders of a HOPS as well as the topological charge of a vortex beam) [40, 51]. The equator of a HOPS represents a set of cylindrical vector beams which carries no angular momentum and is the most used type of VVBs because of its cylindrically symmetric feature and unique performance in optical imaging and manipulation [51].

Constrained by the identical angular momentum carried by the HOPS beams, their applicability remains limited to specific scenarios [41]. The hybrid-order Poincaré sphere (HyOPS) is developed to broaden the scope of HOPS to a more general form, where the LCP and RCP beams represented by the northern and southern poles have distinct topological charges ($|\ell_{LCP}| \neq |\ell_{RCP}|$) [Figure 6.1(b)]. As a result, the total angular momentum carried by a HyOPS beam varies across its surface [102].

Arbitrary vector vortex beams on a HyOPS can be expressed as Eq. (6.1) where φ is the azimuthal angle in polar coordinate of the light beam's cross section, $\tilde{A}_{LN} = A_{LN}e^{i(\phi_{LN})}$ and $\tilde{A}_{RM} = A_{RM}e^{i(\phi_{RM})}$ are the complex amplitudes of the LCP (i.e., $|L\rangle = \frac{\sqrt{2}}{2} \begin{bmatrix} 1 \\ i \end{bmatrix}$) vortex component with a topological charge of N and the RCP (i.e., $|R\rangle = \frac{\sqrt{2}}{2} \begin{bmatrix} 1 \\ -i \end{bmatrix}$) vortex component with a topological charge of M [41]. Note that the N should not be equal to M for the HyOPS beams.

$$U = A_{LN}e^{i(\phi_{LN})}e^{i(N\varphi)}|L\rangle + A_{RM}e^{i(\phi_{RM})}e^{i(M\varphi)}|R\rangle \quad (6.1)$$

From Eq. (6.1), the vector vortex beams on a HyOPS can be regarded as a combination of two orthogonal LCP and RCP vortex components with different topological charges. As shown in Figure 6.1(b), from the northern pole to southern pole of a HyOPS, the Eq. (6.1) could vary from a scalar plane beam to a scalar vortex beam with a topologic charge of 2 by setting $M = 0$ and $N = 2$. The equator of the HyOPS represents a set of cylindrical vector vortex beams (CVVBs) where the LCP and RCP components have same amplitudes $A_{LN} = A_{RM}$.

The scalar beams on the fundamental Poincaré sphere (FPS, Figure 4.7) have uniform distribution of the polarization overall the beam's cross section and a Gaussian intensity distribution. When $N = M = 0$, Eq. (6.1) is simplified to Eq. (6.2) which describes all the scalar beams on the FPS. Therefore, arbitrary polarization state of a scalar beam can be decomposed into two orthogonal LCP and RCP components. The polarization states would vary with the complex amplitudes \tilde{A}_{LN} and \tilde{A}_{RM} . Specifically, the LCP and RCP components in a linear polarization (LP) light beam have same amplitudes $A_{LN} = A_{RM}$, and the phase difference $\Delta\phi_{RL} = \phi_{R0} - \phi_{L0}$ determines the polarization direction of a LP laser beam [40], which is illustrated by the equator of the FPS in Figure 4.7. In experiment, arbitrary scalar beams on an FPS can be obtained by a

combination of a QWP and a half waveplate (HWP). In another word, the \tilde{A}_{LN} and \tilde{A}_{RM} can be tuned to be arbitrary values via a QWP and HWP.

$$U = \tilde{A}_{LN}|L\rangle + \tilde{A}_{RM}|R\rangle \quad (6.2)$$

As shown in Figure 6.1(a), the light beams on a HOPS have a spatial-varied distribution in phase and polarization. In addition, the orthogonal LCP and RCP components in a HOPS beam are vortex beams of same topological charge N with opposite sign. Therefore, the Eq. (6.1) can be re-written into Eq. (6.3) for describing the HOPS beams by replacing M with $-N$. According to Figure 6.1(a) and Eq. (6.3), the equator of a HOPS represents a set of cylindrical vector beams with an order of $N - 1$. Two special cases (azimuthal vector beam and radial vector beam) of the set of CVBs beams are widely used for super-resolution imaging and lithography because of its unique focusing performance, which would be demonstrated in following experiment.

$$U = \tilde{A}_{LN}e^{i(N\varphi)}|L\rangle + \tilde{A}_{RM}e^{i(-N\varphi)}|R\rangle \quad (6.3)$$

$$U(\rho, \varphi) = e^{i[\Phi(\rho) + (\frac{N+M}{2})\varphi]} \{ \tilde{A}_{LN}e^{i(\frac{N-M}{2}\varphi)}|L\rangle + \tilde{A}_{RM}e^{i(\frac{M-N}{2}\varphi)}|R\rangle \} \quad (6.5)$$

In addition, there is no focusing phase included in Eq. (6.1). To obtain arbitrary focused vector vortex beams on a HOPS or HyOPS, a hyperbolic focusing phase profile [Eq. (3.1)] should be imparted to the LCP and RCP components in Eq. (6.1). As a result, arbitrary focused vector vortex beams can be expressed as Eq. (6.5), which indicates that the dielectric metasurface should be able to simultaneously impart the polarization-independent phase profile of $\Phi(\rho) + (\frac{N+M}{2})\varphi$ via the propagation phase ϕ_x and polarization-dependent phase profile of $\pm(\frac{N-M}{2}\varphi)$ via the geometric phase $\pm 2\theta$ on the ongoing scalar laser beam.

Based on the spin-multiplexing principle of a metasurface as well as the relationship between FPS, HOPS, and HyOPS, a unity design method is proposed in this chapter to generate arbitrary vector vortex beams on a HOPS and HyOPS via an all-dielectric metasurface working in the classical spin-multiplexing regime.

It needs to be admitted that, in past ten years, some metasurfaces have been developed for generating and focusing the cylindrical vector beams, HOPS beams, and HyOPS beams [4, 26, 42-47, 103-107]. However, there is not a general design frame of using metasurface to generate non-focused and focused VVBs on a HOPS or a HyOPS. In addition, the HOPS beams and HyOPS beams have not been experimentally generated in the wavelength of 1550nm via a metasurface, while the 1550nm wavelength plays an important role in laser communication, biological imaging, and optical manipulation [101, 108].

A general design frame will be proposed in section 6.2, and section 6.3 derives the controlled generation principle of the arbitrary vector vortex beams over the HOPS and HyOPS is analyzed as well. Then, in proof-of-concept experiments as well as section 6.4, 4 metasurface samples are designed, fabricated, and characterized to controlled generate arbitrary vector vortex beams on the 5th order HOPS (non-focused and tightly-focused), 0-2 order HyOPS, and 0-1 order HyOPS.

6.2 General design frame

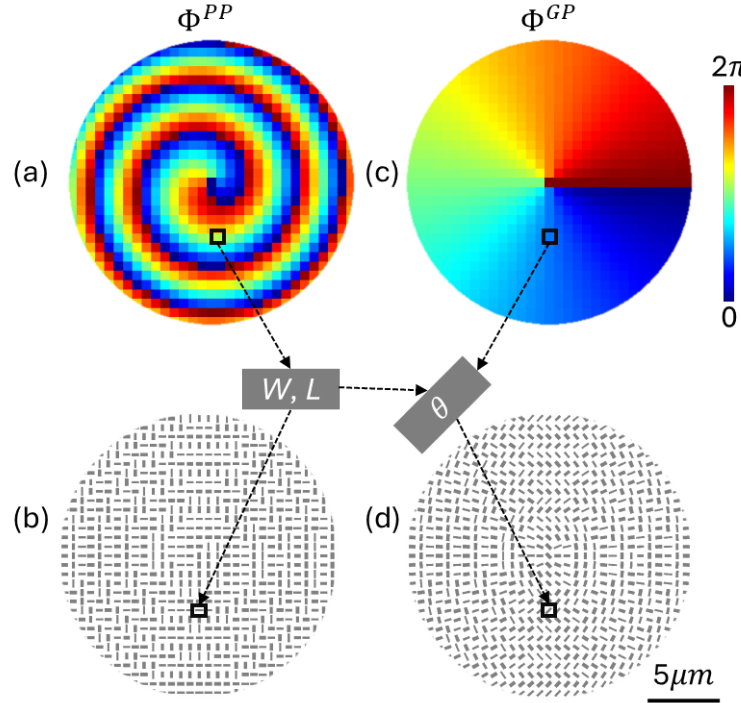


Figure 6.2 Proposed general design frame.

(b) is the dimension's distribution of the meta-atom array obtained via the target propagation phase profile Φ^{PP} shown in (a), (d) is the final distribution of the meta-atom array. Each meta-atom shown in (b) is rotated an angle of θ based on the target geometric phase Φ^{GP} shown in (c).

As discussed above, the metasurface needs to impart a propagation phase profile Φ^{PP} [Eq. (6.6)] and a geometric phase profile Φ^{GP} [Eq. (6.7)] to the transmitted light beam. Based on the meta-atom library built up in Figure 2.2 and Table 5.1, the metasurface can be designed following a general flow.

$$\Phi^{PP}(\rho, \varphi) = \Phi(\rho) + \left(\frac{N+M}{2}\right)\varphi \quad (6.6)$$

$$\Phi^{GP}(\rho, \varphi) = \pm \left(\frac{N-M}{2}\right)\varphi \quad (6.7)$$

Taking the metasurface of generating arbitrary focused vector vortex beams on a HyOPS ($M = 0$, $N = 2$, $\text{NA} = 0.89$) as an example, Figure 6.2 demonstrates the metasurface design flow in detail. Starting from the digitalization [Figure 6.2 (a)] of the target propagation phase Φ^{PP} , the dimension (W, L) [Figure 6.2 (b)] of the meta-atom at each lattice can be determined by looking-up the meta-atoms library (Table 5.1). Next, the rotation angle $\theta = \Phi^{PP}/2$ of each meta-atom can be obtained according to the digitalized geometric phase Φ^{PP} [Figure 6.2 (c)]. Repeating above steps [Figure 6.2(a) - Figure 6.2(c)] for all lattices, the whole metasurface can be designed as shown in Figure 6.2(d)]. Obviously, the rotation angle of the meta-atom array owns a distribution of $\theta(\rho, \varphi) = (N - M)\varphi/4$.

6.3 Manipulation of ongoing optical field

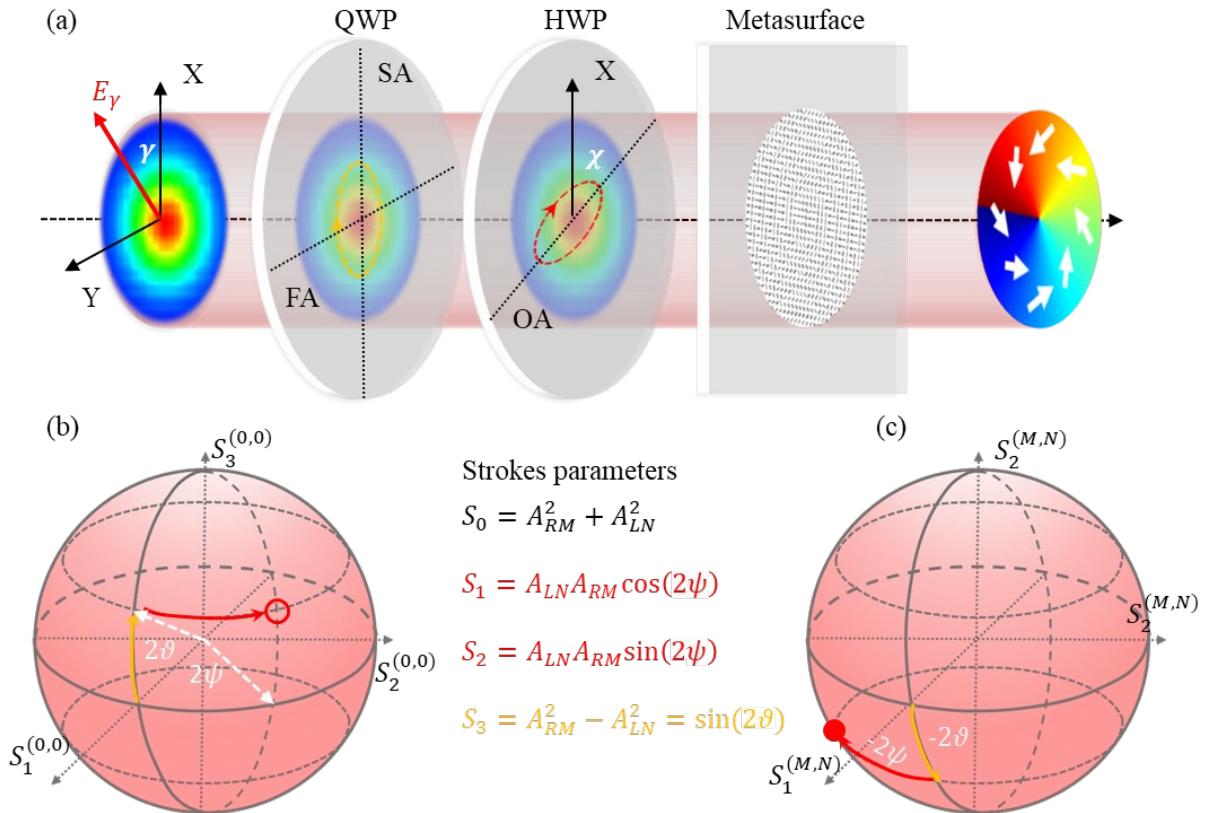


Figure 6.3 Manipulating ongoing optical field over a HOPS and HyOPS.

(a) Scheme of generating arbitrary vector vortex beams on a target HOPS or HyOPS, (b) the circular point represents a scalar beam having a position angles $(2\vartheta, 2\psi)$, (c) the solid red point is the transmitted light beam's position $(-2\vartheta, -2\psi)$ on a HOPS/HyOPS.

As shown in Figure 6.3, a set of QWP and HWP is adopted for manipulating the ongoing optical field over the whole PS surface to achieve arbitrary vector vortex beams on a target HOPS or HyOPS. An LP light beam (E_Y in Figure 6.3, the polarization direction γ) passing through the QWP and HWP can be described as U_0 [Eq. (6.8)] based on Jones matrix. To determine the polarization

state of U_0 (i.e., the polarization angles 2ϑ and 2ψ on an FPS), the complex amplitudes \tilde{A}_{LN} and \tilde{A}_{RM} [Eq. (6.9)] of the LCP and RCP components in U_0 needs to be obtained. Substituting \tilde{A}_{LN} and \tilde{A}_{RM} into the definition of strokes parameters (See Figure 6.3), the position angles (2ϑ and 2ψ in Figure 6.3) can be obtained as Eq. (6.10) where 2ψ denotes the phase difference between the RCP and LCP components. As both χ and γ angles can be continuously tuned from 0 to 2π , arbitrary positions represented by 2ψ and 2ϑ (i.e., \tilde{A}_{LN} and \tilde{A}_{RM}) can be obtained. Therefore, arbitrary beams represented by an FPS can be achieved.

$$U_0 = \begin{bmatrix} \cos(2\chi) & \sin(2\chi) \\ \sin(2\chi) & -\cos(2\chi) \end{bmatrix} \begin{bmatrix} 1 & 0 \\ 0 & i \end{bmatrix} \begin{bmatrix} \cos(\gamma) \\ \sin(\gamma) \end{bmatrix} \quad (6.8)$$

$$\begin{cases} \tilde{A}_{LN} = \frac{1}{\sqrt{2}} [\cos(\gamma) + \sin(\gamma)] e^{i(2\chi)} \\ \tilde{A}_{RM} = \frac{1}{\sqrt{2}} [\cos(\gamma) - \sin(\gamma)] e^{i(-2\chi)} \end{cases} \quad (6.9)$$

$$\begin{cases} 2\psi = -4\chi \\ 2\vartheta = -2\gamma \end{cases} \quad (6.10)$$

Substituting Eqs. (6.6), (6.7), and (6.9) into Eq. (2.8), the light beam transmitted the metasurface sample can be obtained as Eq. (6.11), which demonstrates arbitrary vector vortex beams on a specific HOPS and HyOPS. As shown in Figs. 6(b) and 6(c), after passing through the metasurface, the light beam's position on a HOPS and HyOPS would be opposite to its position on the FPS, because the LCP (RCP) component is converted be RCP (LCP) by the metasurface [Eqs. (18) and (20)].

$$\begin{bmatrix} E_x^o \\ E_y^o \end{bmatrix} = e^{i[\Phi(\rho) + (\frac{N+M}{2})\varphi]} \left\{ \frac{1}{\sqrt{2}} [\cos(\gamma) - \sin(\gamma)] e^{i(-2\chi)} e^{i(\frac{N-M}{2}\varphi)} |L\rangle + \dots \right. \\ \left. \dots \frac{1}{\sqrt{2}} [\cos(\gamma) + \sin(\gamma)] e^{i(2\chi)} e^{i(\frac{M-N}{2}\varphi)} |R\rangle \right\} \quad (6.11)$$

$$\left. \begin{bmatrix} E_x^o \\ E_y^o \end{bmatrix} \right|_{\gamma=0} = e^{i[\Phi(\rho) + (\frac{N+M}{2})\varphi]} \begin{bmatrix} \cos\left[\frac{(N-M)\varphi}{2} - 2\chi\right] \\ \sin\left[\frac{(N-M)\varphi}{2} - 2\chi\right] \end{bmatrix} \quad (6.12)$$

Specifically, when $\gamma = 0$ (i.e., the polarization direction of the incoming light is along the slow axis of the QWP), 2ϑ equal to zeros [Eq. (6.11)] as well. It means that, for $\gamma = 0$, Eq. (6.11) represents the vector beams on the equator of the HOPS and HyOPS. Introducing $\gamma = 0$ to the Eq. (6.8), the outgoing light beam $U_0(\gamma = 0) = \begin{bmatrix} \cos(2\chi) \\ \sin(2\chi) \end{bmatrix}$ which is LP and has a polarization direction of 2χ . In linear polarization basis (see Appendix C), the optical field represented by Eq. (6.11) can be simplified to be Eq. (6.12).

Eq. (6.12) clearly demonstrates that the vector beams represented by the HOPS and HyOPS' equator are a set of CVVBs with an order of $(N - M)/2$ and a topological charge of $(N + M)/2$. For example, when $N = 2, M = 0$, the equator represents a set of CVVBs with an order of 1 and a topological charge of 1, as shown in Figure 6.1(b). Appendix C gives a simple explanation of Eq. (6.12) based on linear polarization basis.

6.4 Proof-of-concept experiments

Up to now, the general design frame and manipulation of ongoing VVBs over a target HOPS/HyOPS have been theoretically studied. Specifically, based on the linear polarization basis, the order and topological charge of the CVVBs represented by a HOPS/HyOPS' equator are quantitatively presented for the first time. In following proof-of-concept experiment, 4 metasurface samples are designed, fabricated, and characterized. Design parameters and target of the 4 samples are summarized in Table 6.1.

Table 6.1 Parameters and target of metasurface samples.

Number of samples	Design parameters	Target
1	$M = 5, N = -5, \Phi(\rho) = 0$	Non-focused 5 th -order HOPS beams
2	$M = 5, N = -5, f = 300\mu m$	Focused 5 th -order HOPS beams (NA=0.89)
3	$M = 0, N = 2, f = 1mm$	Focused 0-2 order HyOPS beams (NA=0.89)
4	$M = 0, N = 1, f = 1mm$	Focused 0-1 order HyOPS beams (NA=0.89)

6.4.1 Non-focused 5th-order HOPS beams

The metasurface sample 1 is designed by setting $M = 5, N = -5, \Phi(\rho) = 0$ to generate arbitrary non-focused 5th-order HOPS beams. The intensity distribution of the transmitted light beam is theoretically calculated based on the Eq. (6.11) and illustrated in Figure 6.4(a). The position angles $(2\vartheta, 2\psi)$ in Figure 6.4(a) are obtained based on the Eq. (6.10) and the parameters (γ, χ) adopted for Eq. (6.11). Considering the orthogonality of the X- and Y-components in the transmitted light and the symmetry of the X- and Y-component's intensity, Figure 6.4(a) only

depicts the near-field of the X-component in the transmitted light beam. As shown in Figure 6.4(a), the near field distribution of the X-component becomes a clearly gear-like pattern from an almost uniform pattern with manipulating the 2θ from $\pm \frac{\pi}{2}$ to 0. (i.e., the ongoing optical field $\begin{bmatrix} E_x^o \\ E_y^o \end{bmatrix}$ is manipulated from the two poles to the equator).

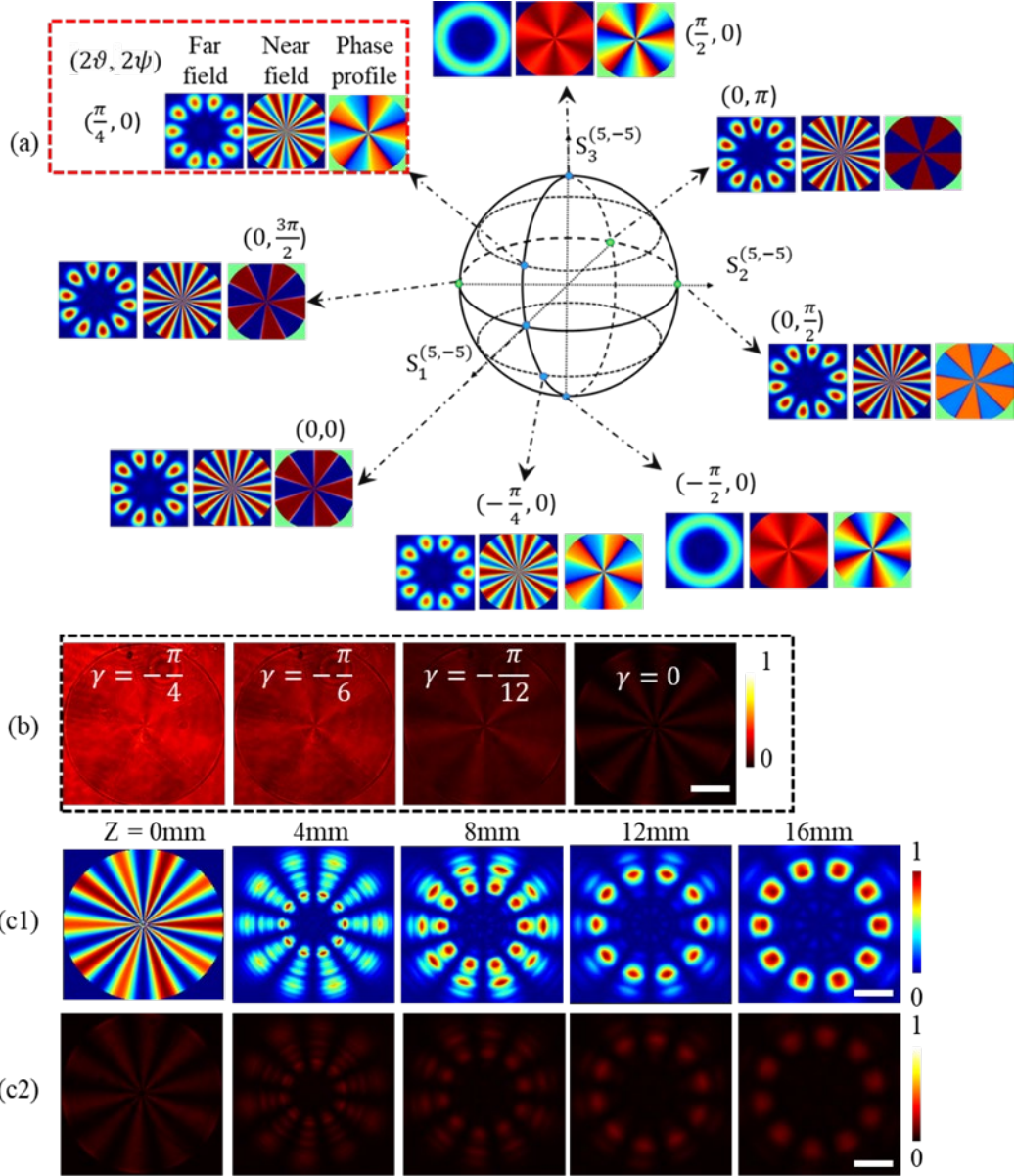


Figure 6.4 Experimental results: non-focused 5th-order HOPS beams.

(a) Simulated far-field, near-field, and phase profile distribution of the X-component in the transmitted light beams over the target 5th-order HOPS by manipulating the position angles $(2\theta, 2\psi)$, (b) measured near-field distribution of the X-component, (c1) and (c2) are the simulated and experimental results of the X-component's propagation evolution from the metasurface ($Z=0\text{mm}$) to $Z = 16\text{mm}$. Scale bars: $130\mu\text{m}$.

In experiment, the ongoing optical field $\begin{bmatrix} E_x^o \\ E_y^o \end{bmatrix}$ is collected via the customized microscope (Figure 3.5) where the sample 1 is illuminated by a collimated 1550nm laser beam. To obtain the near field distribution of the X-component, the microscope is focused on the sample 1 ($Z = 0$), and a polarizer is placed in front of the camera to select the X-component in ongoing optical field. Figure 6.4(b) shows the experiment result where the near-field of X-component is tuned to be clearly gear-like pattern from an almost uniform pattern with manipulating the 2γ (i.e., -2ϑ) from $-\frac{\pi}{2}$ to 0.

Based on the Fourier transformation of near field, the far field of the X-component is obtained and shown in Figure 6.4(a) as well. It is obviously that the distribution of near field and far field of the transmitted light beam is quite different as shown in Figure 6.4(a). Therefore, it is meaningful to figure out that how the transmitted light beam evolves from the near field pattern ($Z = 0$) to the far field pattern. Keeping $\gamma = 0$ ($2\vartheta = 0$), the intensity evolution with the propagation distance Z is theoretically obtained via angular spectrum theory [109] and measured in experiment. The theoretical and experimental results are shown in Figure 6.4(c1) and Figure 6.4(c2), respectively, which demonstrates that experimental results coincide well with the theoretical results. From both numerical and experimental results, the gear-like near field ($Z = 0\text{mm}$) gradually converge to the far field pattern with multiple-lobes at around $Z = 12\text{mm}$, and then the far field pattern divergently propagates away ($Z > 12\text{mm}$).

6.4.2 Tightly-focused 5th-order HOPS beams

To obtain the tightly-focused 5th-order HOPS beams via a metasurface, the metasurface sample 2 owning a diameter of 1.2mm is designed by setting $M = 5, N = -5, f = 300\mu\text{m}$. The target NA of sample 2 is 0.89. The tightly-focused far field (Figure 6.5) can be measured at the focal plane of the sample 2.

Figure 6.5 demonstrates the controlled generation of tightly focused 5th-order HOPS beams along its longitude line and equator by tuning the angles (γ, χ) . It could be seen that the far field of X- and Y-components is orthogonal to each, and the total fields are donut-shape over the whole 5th-order HOPS. From the first 3 columns in Figure 6.5, the X- and Y-components spread to be donut-shaped from 10 lobes [Figure 6.5 (b)] with manipulating the 2γ (i.e., -2ϑ) from 0 to $\pm\pi/2$. Keeping $\gamma = 0$, it is observed that the 10 lobes in X- and Y-components rotate by the angle of HWP (i.e., 2χ) [Figure 6.5(b), (d) – (f)]. The far field distributions (Figure 6.5) measured in the focal plane of the sample 2 match well with the theoretically obtained far field distribution [Figure 6.4(a)].

To show the tightly-focusing property of the 5th-order HOPS beams, the size of each lobe in the Figure 6.5(b) is quantitatively evaluated. Each lobe has a tiny lateral FWHM of 828nm, which is

22% smaller than the diffraction limitation (1062nm, $0.61\lambda/NA$), which indicates that the tightly-focused HOPS beams can be used for super-resolution imaging.

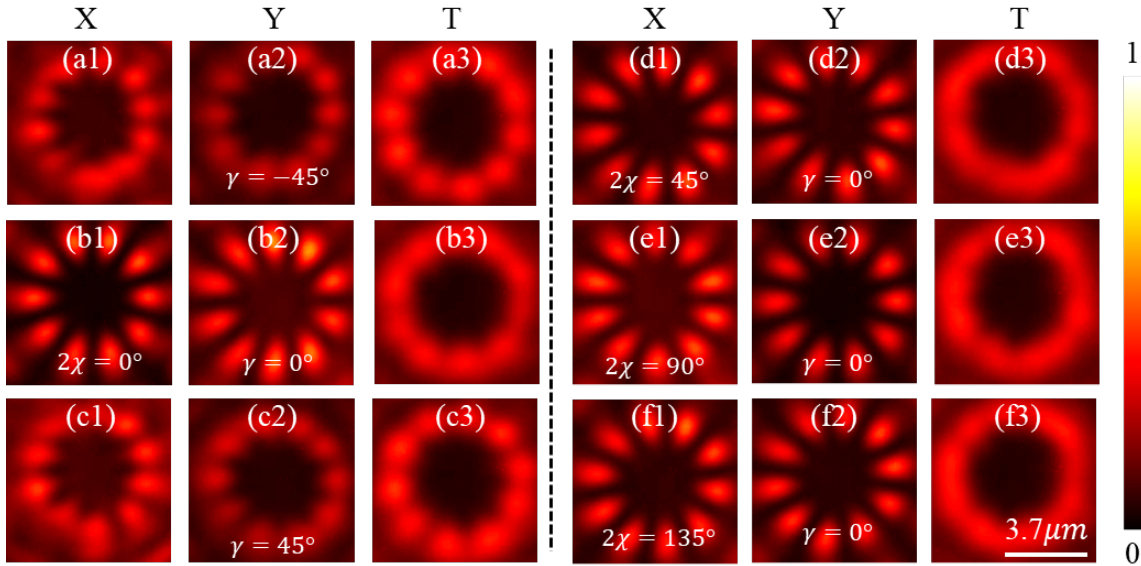


Figure 6.5 Experiment results: tightly focused 5th-order HOPS beams.

Manipulating along the HOPS's longitude (a) – (c) and along its equator (d) – (f). The 1st and 4th columns are the X-components in the total focal fields T (3rd and 6th columns), the 2nd and 5th columns are the Y-components.

6.4.3 Tightly-focused 0-2 order HyOPS beams

In this section, the metasurface sample 3 with a diameter of 4mm is detailed studied in simulation and experiment for generating arbitrary focused beams on the 0-2 order HyOPS. As shown in Figure 6.1(b), from the northern pole to southern pole along a latitude line, the topological charge (TC) carried by a 0-2-order HyOPS beam gradually increases to 2 from 0. The beams on its equator are the 1st-order CVVBs with a TC of 1 [Eq. (6.12) as well as Eq. (A.5)]. It is firstly verified that the outgoing optical field from the metasurface can be tuned from a scalar RCP (LG00, TC, $\ell = 0$) to a CVVB (TC, $\ell = 1$) and to a scalar LCP (LG02, TC, $\ell = 2$) with the incident laser beam being tuned from a scalar LCP to an LP and to an RCP beam in simulation (first three columns in Figure 6.6). With rotating the polarization direction (i.e., 2χ) of the incident LP beam, arbitrary 1st-order CVVBs (TC, $\ell = 1$) can be generated via this metasurface (last three columns in Figure 6.6).

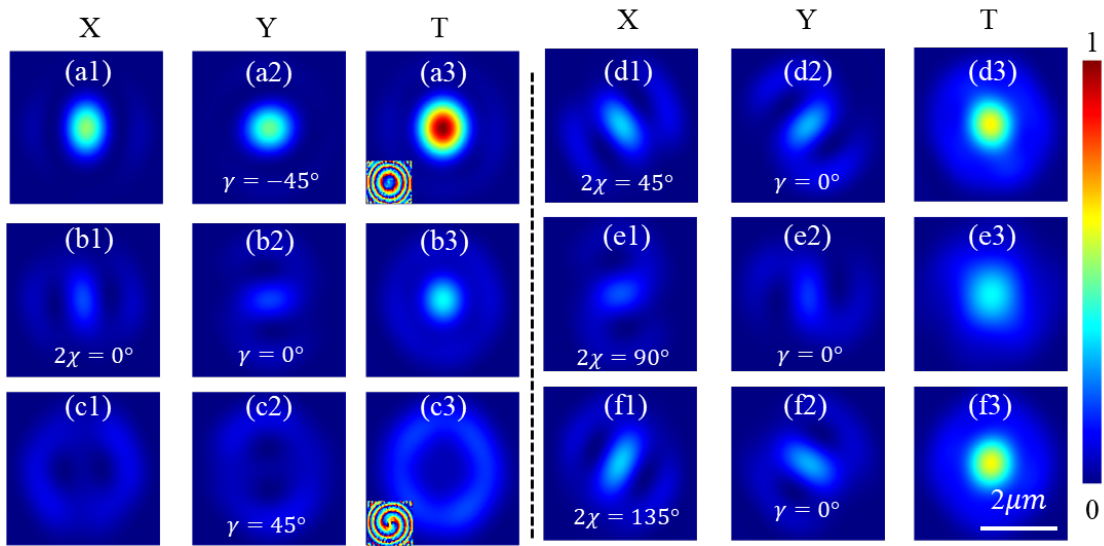


Figure 6.6 Simulation results: tightly focused 0-2-order HyOPS beams.

Manipulating along the PS's longitude (a) – (c) and along its equator (d) – (f). The 1st and 4th columns are the X-components in the total focal fields T (3rd and 6th columns), the 2nd and 5th columns are the Y-components.

The NIR microscope (Figure 3.5) with a magnification of 100X and NA of 0.9 is customized for characterizing the metasurface. The LG00 focal point is measured to obtain the metasurface's NA under the LCP beam illumination. The FWHM of the LG00 focal point is measured to be 1060nm [Figure 6.7(c1)], which demonstrates that the fabricated metasurface has a NA of 0.89. As the incident beam's polarization changing from LCP to RCP, the focal point is tuned from a diffraction-limited LG00 spot [Figure 6.7(a)] to an LG02 donut [Figure 6.7(c)] along the latitude line of the 0-2 order HyOPS. The intensity in the focal plane gradually spreads from the central area to the donut ring [Figure 6.7(a-c)] with tuning incident laser beam's polarization state from LCP ($\gamma = -45^\circ$) to RCP ($\gamma = 45^\circ$) by rotating a QWP.

As predicted by Eq. (6.12) and simulation results in Figure 6.6, arbitrary 1st-order CVVBs by manipulating the LP laser beam's polarized angle 2χ via rotating the HWP [Figure 6.7(b), (d)-(f)]. For $2\chi = 0$, an azimuthal vector vortex beam (a special case of the CVVBs) is generated and tightly-focused. As a result, a focal point (FWHM = 870nm) which is smaller 18% than the diffraction limitation (1062nm, $0.61\lambda/NA$) is obtained [Figure 6.7(b)]. With changing the LP laser beam from an X-polarized ($2\chi = 0^\circ$) beam to a Y-polarized beam ($2\chi = 90^\circ$), the focal point's FWHM goes up, and optical intensity goes down. Furthermore, it is measured that the 8-shaped intensity distribution of the X-components [Figure 6.7(b1), (d1) -(f1)] and Y-components [Figure 6.7(b2), (d2) -(f2)] rotates with the polarization direction 2χ .

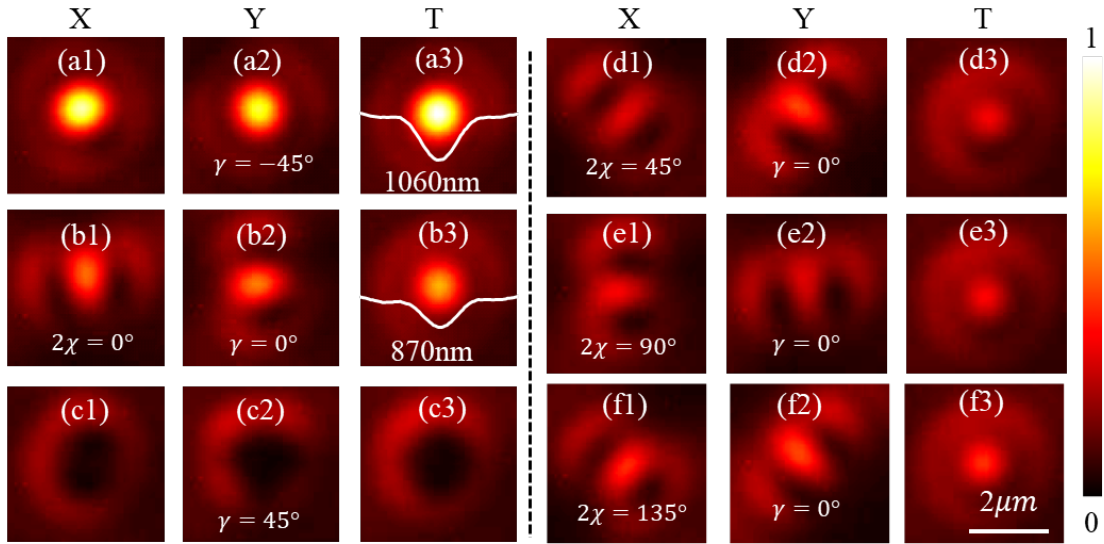


Figure 6.7 Experiment results: tightly focused 0-2-order HyOPS beams.

Manipulating along the PS's longitude (a) – (c) and along its equator (d) – (f). The 1st and 4th columns are the X-components in the total focal fields T (3rd and 6th columns), the 2nd and 5th columns are the Y-components.

6.4.4 Tightly-focused 0-1 order HyOPS beams

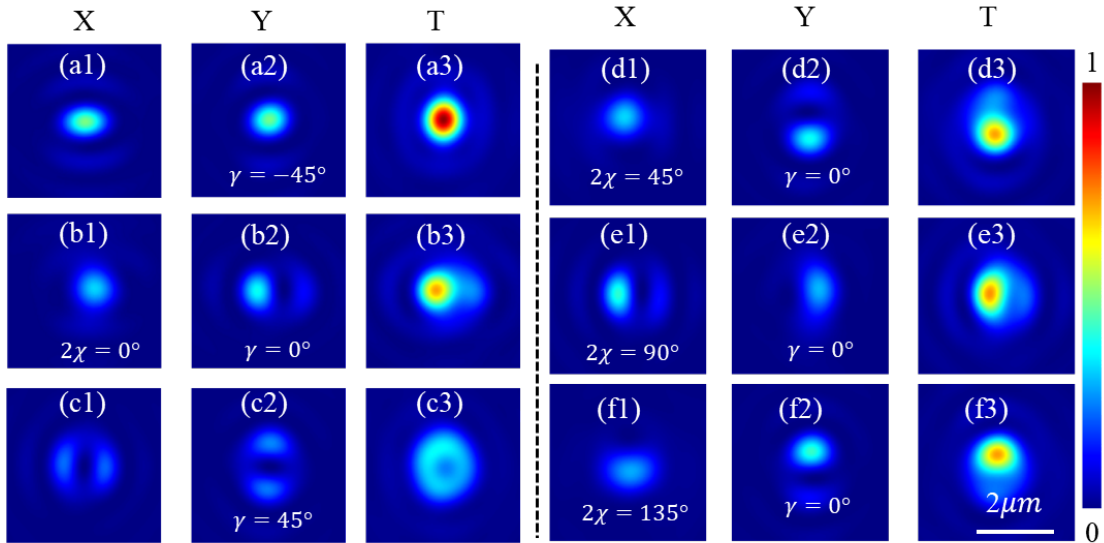


Figure 6.8 Simulation results: tightly focused 0-1-order HyOPS beams.

Manipulating along the PS's longitude (a) – (c) and along its equator (d) – (f). The 1st and 4th columns are the X-components in the total focal fields T (3rd and 6th columns), the 2nd and 5th columns are the Y-components.

The vector order and topological charge of the CVVBs represented by the 0-2 order HyOPS are both one and integer values, and a super-resolution focal point beyond diffraction-limitation is obtained in both simulation and experiment. It is theoretically reported that there is a large difference between the CVVBs with integer order/topological charge and fractional order/topological charge. Therefore, the sample 4 with a diameter of 4mm and a target NA of 0.89 is designed and measured to experimentally study the difference for the first time. The sample 4 is detailly studied in simulation (Figure 6.8) and experiment (Figure 6.9). According to Eq. (6.11), the topological charge carried by all vector vortex beams on the 0-1 order HyOPS is fractional. Based on Eq. (6.12), The CVVBs represented by the 0-1 order HyOPS' equator have a vector order of 0.5 and a topological charge of 0.5.

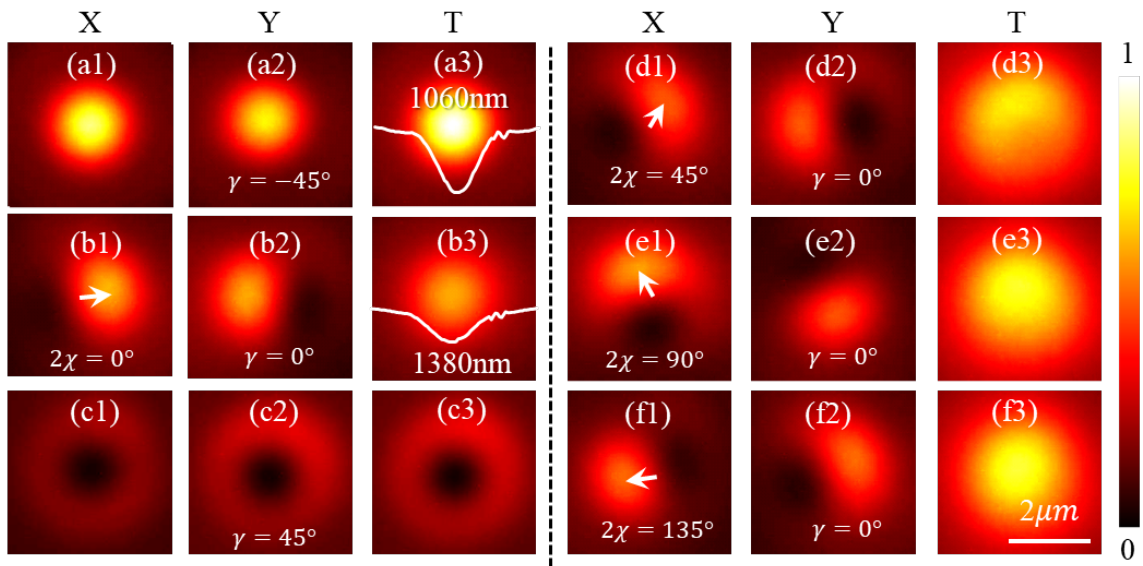


Figure 6.9 Experiment results: tightly focused 0-1-order HyOPS beams.

Manipulating along the PS's longitude (a) – (c) and along its equator (d) – (f). The 1st and 4th columns are the X-components in the total focal fields T (3rd and 6th columns), the 2nd and 5th columns are the Y-components.

The tunability of the topological charge carried by the ongoing light beam is studied by manipulating the incident laser beam's polarization state. With the polarization state is tuned from LCP to RCP, the ongoing laser beam is tuned from a diffraction-limited Gaussian spot [FWHM = 1060nm, Figure 6.8(a3) and Figure 6.9(a3)] to an LG01donut [Figure 6.8(c3) and Figure 6.9(c3)]. Because the topological charge (1) carried by the southern pole of 0-1 order HyOPS is smaller than that (2) of the 0-2 order HyOPS, the radius of the central holes shown in Figure 6.8(c3) and Figure 6.9(c3) is smaller than that in Figure 6.6(c3) and Figure 6.7(c3).

Comparing the focal fields in sections 6.4.3 and 6.4.4, there is a clear difference in the intensity evolution of the 0-1 order and 0-2 order HyOPS beams from northern to southern poles. While the

light energy spreads from a Gaussian solid point to a donut and keeps rotational symmetric for the 0-2 order HyOPS (section 6.4.3), the light intensity maximum is offset from the optical axis and intensity distribution becomes non-symmetric around the optical axis for the 0-1 order HyOPS (section 6.4.4). Moreover, a non-axial zero point appears in the focal field of arbitrary vector vortex beams on the 0-1-order HyOPS, which arises from the superposition of fractional vortex phase carried by the LCP and RCP components [Eq. (6.11)].

When the sample 4 is illuminated by an LP light beam, the uniaxial symmetric property is distinct in the transmitted light beam's focal plane [Figure 6.9(b)]. As a results, the FWHM of the total field [Figure 6.9(b3)] is 1380nm and larger than the diffraction limitation. With changing the linear polarization direction 2χ , the non-axial maximum intensity [arrows in Figure 6.9(b), (d)-(f)] and null intensity in X- and Y-components rotate around the optical axis. These experiment results in Figure 6.9 match well with the simulation results in Figure 6.8 as well as the reported theoretical results in paper [110]. As far as we know, it is the first time that the tightly focusing properties of fractional VVBs and CVVBs are experimentally studied, which highlights the merit of the proposed general design frame.

6.5 Conclusion

In the classical spin-multiplexing regime, a general design frame of single-layer dielectric metasurface is proposed to generate arbitrary non-focused/focused vector vortex beams on a HOPS/HyOPS. Based on the Jones-matrix method, the controlled generation mechanism is theoretically derived as well. Especially, based on linear polarization basis, the simultaneous modulation of local polarization direction and phase is obtained for the first time to analyze the controlled generation of the CVVBs on the HOPS/HyOPS' equator. According to the proposed design frame and a linear polarization basis, the orders and topological charges of the CVVBs represented by the equator of a HyOPS can be obtained. In proof-of-concept experiments, 4 metasurface samples are designed, fabricated, and measured to generate arbitrary beams on the 5th order HOPS (non-focused and tightly-focused), 0-2 order HyOPS, and 0-1 order HyOPS. Because of the simplicity and feasibility of the general design frame, I conceive this research could boost the metasurface as well as VVB's applications.

Chapter 7 Longitudinal tri-foci metalens for integrated microscope

7.1 Introduction

Different from a conventional lens, a metalens can be engineered to possess multiple focal points via spatial multiplexing or wavefront shaping technique, which makes it possible to realize a multiple focal points via a single metalens [60, 111-113]. However, the multiple-foci metalens has not been used to build up an integrated microscope system with multiple magnifications and diffraction-limited resolution. In addition, there is no report on Si_3N_4 multi-foci metalens, limited by the classical spin-multiplexing working regime, low refraction index of Si_3N_4 , and the fabrication ability of high aspect ratio nanostructure.

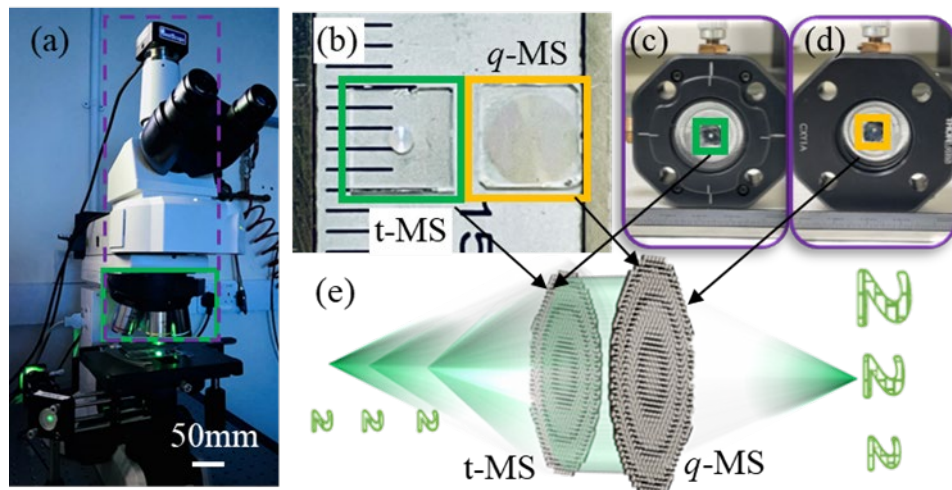


Figure 7.1 Conceptual figure of integrated microscope with three magnifications.

(a) Conventional infinity-corrected microscope; (b) optical images of two metalens samples; (c) and (d) are the front (t-MS) and rear (q-MS) surface of the integrated microscope, respectively; (e) Optical configuration of integrated microscope. t-MS: tri-foci metalens; q-MS: metalens with quadratic phase profile.

In a conventional microscope, only one magnification and resolution can be achieved using one objective lens [114]. Multiple objective lenses are necessary for realizing multiple magnifications and resolutions, and a nosepiece with high accuracy is required for replacing the objective lens [the section marked by green rectangle in Figure 7.1(a)]. As a result, the conventional microscope system is bulky and expensive. To integrate three objective lenses into one element and eliminate the nosepiece, a Si_3N_4 metalens with longitudinal three focal points (i.e., tri-foci metalens, t-MS) and a diameter of 1.2mm is obtained in this chapter [Figure 7.1(b)] based on the non-classical spin-multiplexing regime. By introducing the t-MS into a commercial microscope [Figure 7.1(a)],

three magnifications can be obtained without replacing objective lens. Then, the whole microscope system [the section marked by purple rectangle in Figure 7.1(a)] including three objective lenses is miniaturized to millimeter-scale where two metalens samples are compactly integrated by a 3D printed holder [Figure 7.1(c - e)]. In the miniaturized microscope system [Figure 7.1(e)], the t-MS is utilized as an objective lens with three focal points, and another metalens (q -MS) with a quadratic phase profile and one focal point works as a tube lens.

7.2 Desing of longitudinal tri-foci metalens

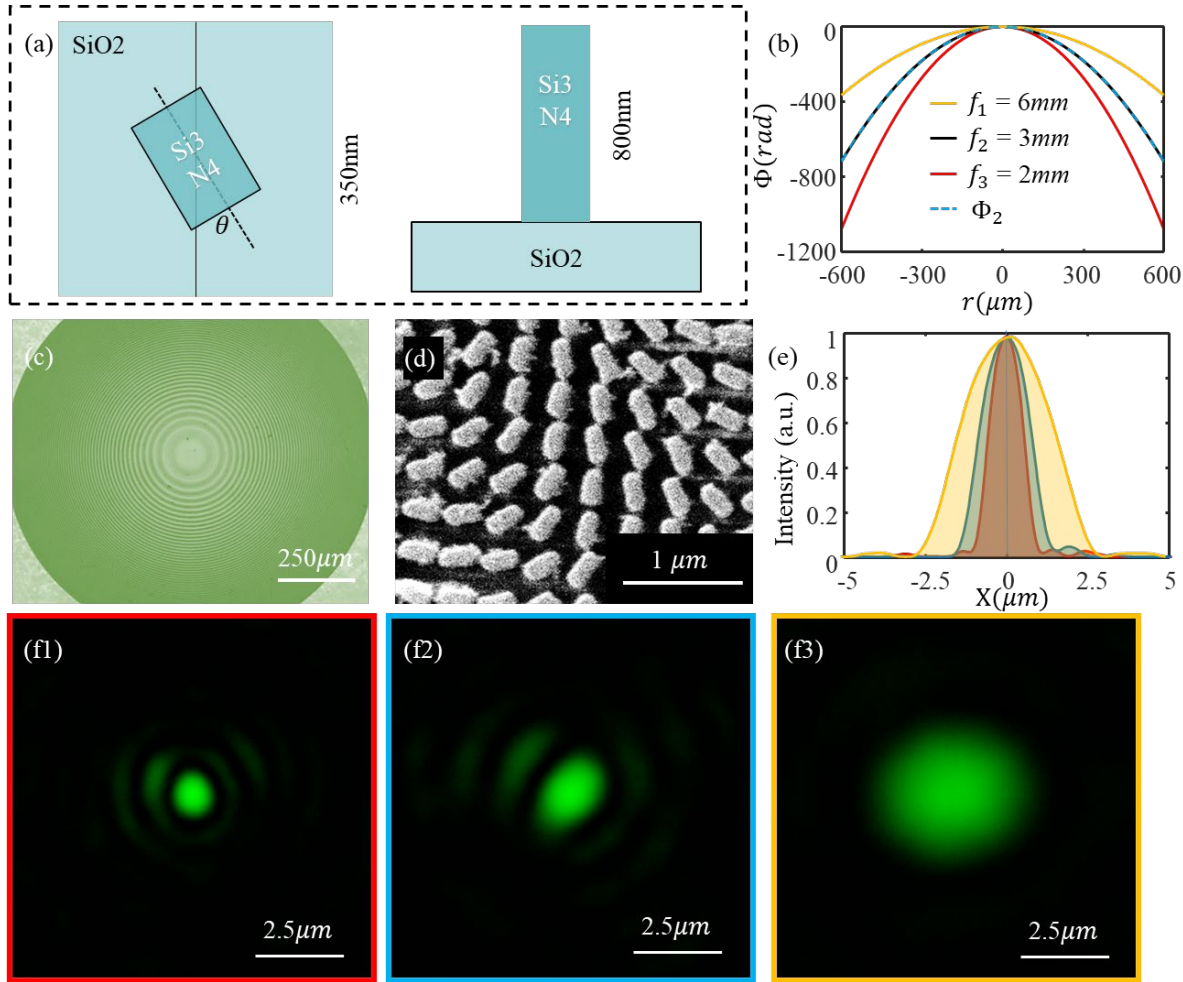


Figure 7.2 Design and optical characterization of the metalens sample.

(a) nanofin structure; (b) three hyperbolic phase profiles for the three focal points; (c) optical image of the metalens with a diameter of 1.2mm; (d) metalens sample's SEM image; (e) the FWHMs of three focal points; (f1) - (f3) are the three focal points at focal length $f = 1.9mm, 3mm$, and $6mm$, respectively.

To achieve the longitudinal tri-foci metalens based on Si_3N_4 with a refraction index of 2, the metalens being made of an anisotropic truncated waveguide meta-atom [Figure 7.2(a)] array is designed in non-classical spin-multiplexing regime (see section 2.2.3 in page 26). When the metasurface working in non-classical spin-multiplexing regime, the ongoing light $|E_0\rangle$ from the

meta-atom could be imposed three phase profiles $\Phi_1(\rho, \varphi) = 2\theta(\rho, \varphi) + \phi_p(\rho, \varphi)$, $\Phi_2(\rho, \varphi) = -2\theta(\rho, \varphi) + \phi_p(\rho, \varphi)$, and $2\Phi_3(\rho, \varphi) = \phi_p(\rho, \varphi) = \Phi_1(\rho, \varphi) + \Phi_2(\rho, \varphi)$. $\phi_p(x, y)$ is the distribution of propagation phase $\phi_p = (\phi_x + \phi_y)/2$, and $\theta(x, y)$ is the rotation distribution of the meta-atoms array. To design the t-MS, a Si_3N_4 meta-atoms library is built up as first.

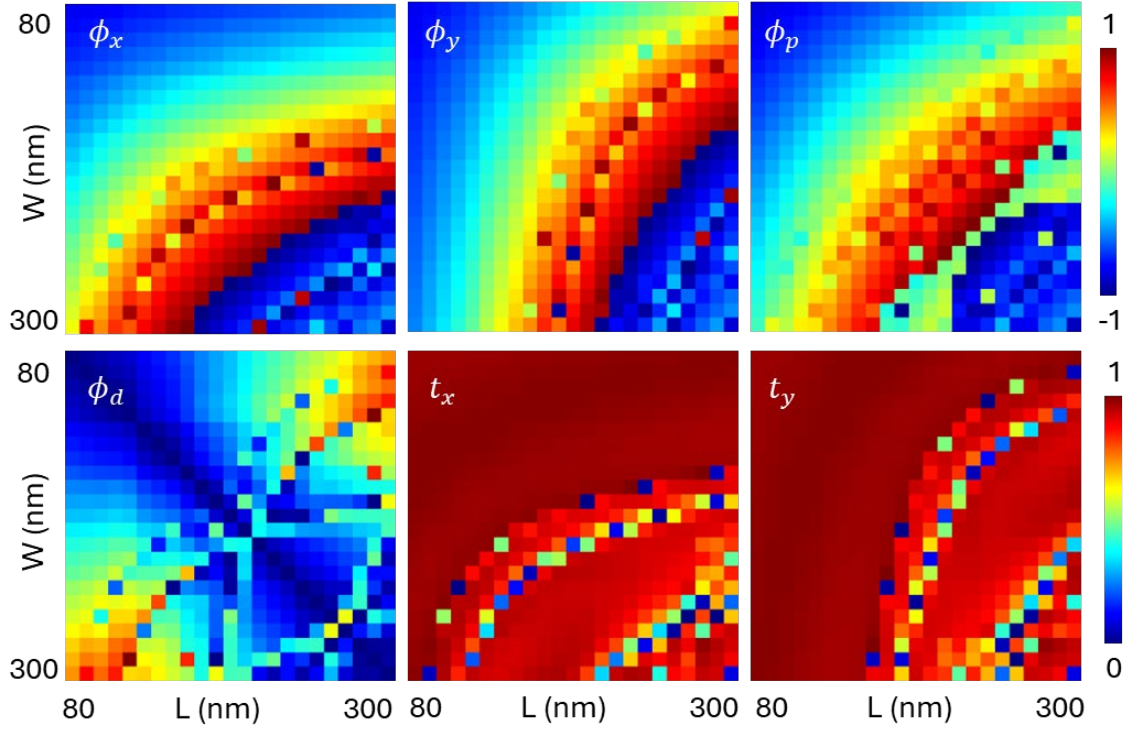


Figure 7.3 Cell library for Si_3N_4 metalens in chapters 7 and 8.

The phase maps ϕ_x, ϕ_y, ϕ_p , and ϕ_d have a unit of π .

To build a Si_3N_4 meta-atom library with high transmission and working in the non-classical spin-multiplexing, the height and period of the meta-atom is firstly optimized to be 800nm and 350nm [Figure 7.2(a)], respectively. Then, the width and length of the meta-atom are swept as shown in Figure 7.3. Based on the data, 14 meta-atoms are selected to build up a library where each meta-atom has a phase difference ϕ_d of $\frac{5\pi}{12}$ and the phase propagations ϕ_p varies from $-\pi$ to π .

In designing the t-MS, the phase profile $\Phi_1(\rho, \varphi)$ is the hyperbolic phase profile [Eq. (3.1)] with a focal length f_1 of 6mm, the phase profile $\Phi_3(\rho, \varphi)$ is the hyperbolic phase profile with a focal length f_3 of 2mm. Then, the $\Phi_2(\rho, \varphi) = 2\Phi_3(\rho, \varphi) - \Phi_1(\rho, \varphi)$ is obtained. According to Eq. (7.1) where $\Phi(f, \rho, \varphi)$ is the hyperbolic phase profile given in Eq. (3.1), the $\Phi_2(\rho, \varphi)$ can be seen as a hyperbolic phase with a focal length f_2 of 3mm. The three phase profiles are plotted in Fig. 2(b) in yellow, blue, and red colors, respectively. In addition, from the red curve and purple dashed curve, the $\Phi_2(\rho, \varphi)$ meets well with the $\Phi(f_2 = 3\text{mm}, \rho, \varphi)$. Once the metalens with a diameter of 1.2mm is designed, some samples are fabricated following a CMOS-compatible process in our University Cleanroom (Figure 7.8).

$$2\Phi\left(\frac{2f_1f_3}{f_1+f_3}, \rho, \varphi\right) \approx \Phi(f_1, \rho, \varphi) + \Phi(f_3, \rho, \varphi) \quad (7.1)$$

7.3 t-MS characterization

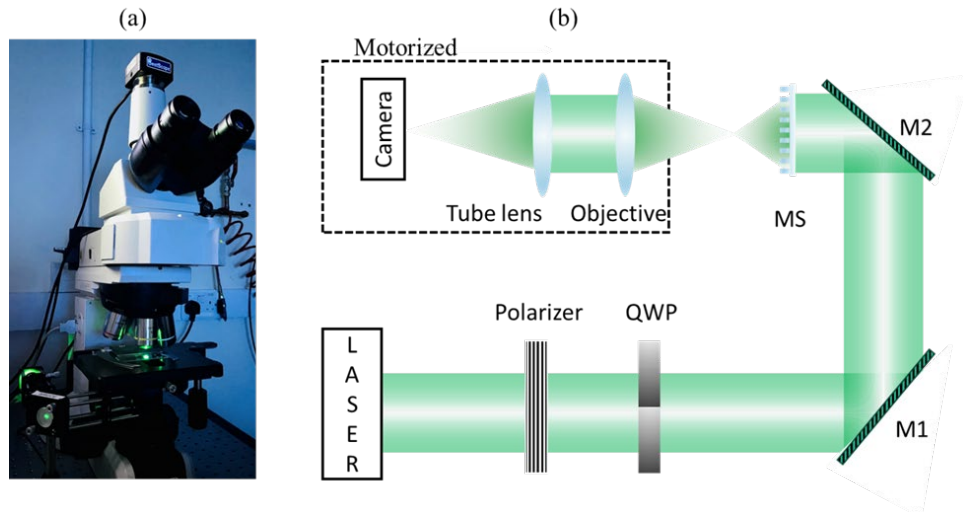


Figure 7.4 Optical configuration for measuring Si_3N_4 metolens samples.

As shown in Figure 7.1(a) and Figure 7.4, a microscope is built in our lab based on a Nikon microscope. A collimated 520 nm laser is adopted to replace the illumination path and guided to the MS sample via two mirrors (M1 and M2). The focused light via the MS is collected by a 10X objective lens ($\text{NA} = 0.3$) and imaged to a camera via a tube lens with a focal length of 200 mm. A polarizer and QWP are placed in the illumination path for controlling the incident light's polarization.

Figure 7.2(c and d) shows the optical image and SEM image of the fabricated metolens sample. Then, the t-MS sample is characterized by the home-built microscope. The first focal point [Figure 7.2(f1)] is observed with moving the imaging part of the microscope 1.9 mm away from the surface [Figure 7.2(c)] of the t-MS sample. It means the measured first focal point has a focal length of 1.9 mm. With moving microscope's imaging part 3 mm and 6 mm away from the sample surface, the second focal point [Figure 7.2(f2)] and third focal point [Figure 7.2(f3)] are observed, respectively. Therefore, the three longitudinal focal points have an expected focal length. The measured NAs of three focal points can be calculated as 0.3 ($f = 1.9\text{mm}$), 0.2 ($f = 3\text{mm}$), and 0.1 ($f = 6\text{mm}$), respectively.

To furtherly evaluate focusing performance of the three focal points, focal points' FWHM are calculated [Figure 7.2(e)]. The FWHMs of three focal points are $1.18\mu\text{m}$, $1.79\mu\text{m}$, and $3.51\mu\text{m}$, respectively. As the diffraction limitation ($0.61\lambda/\text{NA}$) can be theoretically calculated upon the working length $\lambda = 520\text{nm}$ and NA , the diffraction limitations of each focal points can be obtained as $1.02\mu\text{m}$ ($f = 1.9\text{mm}$, $\text{NA} = 0.3$), $1.56\mu\text{m}$ ($f = 3\text{mm}$, $\text{NA} = 0.2$), and $3.12\mu\text{m}$ ($f = 6\text{mm}$,

NA = 0.1). Comparing the FWHMs and theoretical diffraction limitations of each focal points, three near-diffraction-limitation longitudinal focal points are obtained via the Si_3N_4 metasurface sample.

7.4 Compact imaging experiment

7.4.1 Combining with Nikon microscope

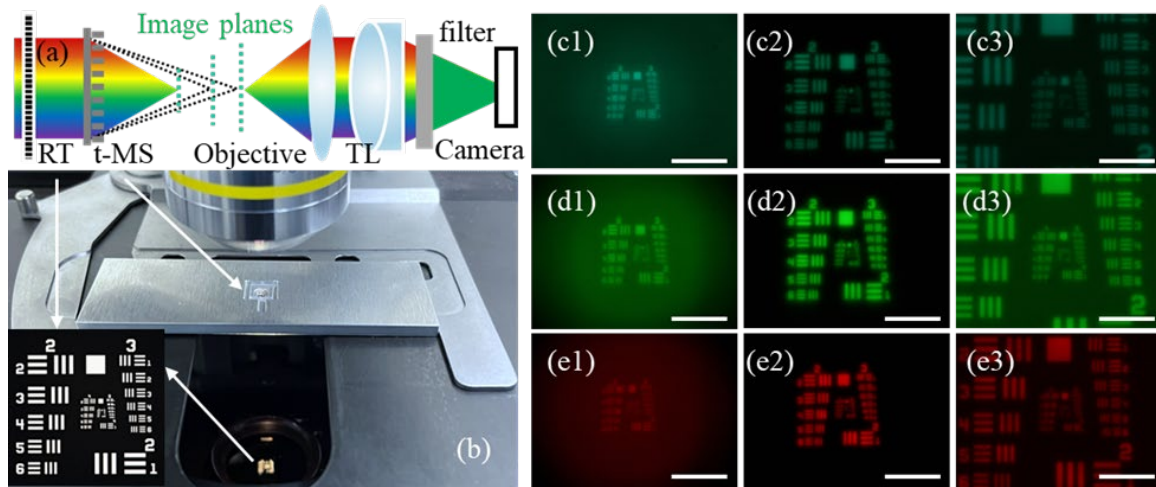


Figure 7.5 Singlet imaging for extending Nikon microscope.

(a) Optical configuration. RT: resolution target [USAF 1951, see the insert in (b)]; TL: tube lens;

(b) Experiment setup; (c) – (e) are the imaging results (the 1st column is obtained at $f = 1.9\text{mm}$, the 2nd column at $f = 3\text{mm}$, the 3rd column at $f = 6\text{mm}$) for the wavelength of 488nm, 520nm, and 650nm, respectively. Insert figure in (b) is the ground truth of the RT. Scale bars: 1mm.

The t-MS sample is firstly used as a condenser in a commercial microscope [Figure 7.1(a)]. As shown in Figure 7.5(a and b), a positive USAF 1951 resolution target (RT) is placed in the collimated illumination light path, and it is illuminated by a lamp with wide emission spectrum. Then, through the imaging of the t-MS sample, three images [Figure 7.5(a)] corresponding to the three focal points can be obtained. Then, the three images are collected and magnified by the commercial microscope with an objective lens (10X, NA = 0.3). Because the chromatic aberration is corrected in designing, the RT cannot be imaged to a same plane for different wavelength at each focal point. Therefore, a tunable bandpass filter (Thorlabs: KURIOS-WB1/M) is placed in front of the camera to capture the image of each single wavelength. Note that the light passing through the filter still has a bandwidth of 35nm. Therefore, the image captured by the camera is not exactly for a single wavelength.

By setting the central wavelength of the filter at 488nm, 520nm, and 650nm, 9 images are obtained and demonstrated in Figure 7.5 (c – e). To compare the magnification's difference of each focal point as well as the central wavelength, the scale bars are marked based on the image size (i.e., pixel number \times pixel size) in camera coordinator. Therefore, the larger FOV from the images illustrates a smaller magnification. The images on Figure 7.5(c1), Figure 7.5(c2), and Figure 7.5(c3) are respectively obtained at the 1st ($f = 1.9\text{mm}$), 2nd ($f = 3\text{mm}$), 3rd ($f = 6\text{mm}$) focal point. We can see that, with moving the objective lens from the 1st focal point to the 3rd one, the imaging FOV goes down. Because the singlet imaging magnification goes up with the increasement of focal length for a fixed object distance between the RT and t-MS sample.

Comparing Figure 7.5(d) and Figure 7.5(e), it is observed that the imaging FOV goes up with the working wavelength is tuned from 520nm to 650nm, which indicates that the magnifications corresponding to each focal point goes down with increasing the working wavelength. Furtherly, this phenomenon arising from the dispersion relation (i.e., the focal length goes down with increasing the working wavelength) of a metalens. Therefore, the t-MS sample works well for a wide visible spectrum (488nm – 650nm), while it cannot achieve broadband achromatic imaging. Importantly, by using the t-MS sample as a condenser, the commercial Nikon microscope could realize three magnifications without replacing objective lens.

7.4.2 Integrated tri-magnification microscope

In this section, the t-MS sample is adopted as an objective lens to build an integrated and miniaturized microscope with three magnifications. To try miniaturizing the whole microscope to be centimeter level and reduce its weight, this section designs and fabricates another metalens sample which is used a tube lens as shown in Figure 7.1(a) and Figure 7.6(a). To realize large FOV imaging with low distortion, a quadratic phase profile [Eq. (7.2)] is adopted in designing the second metalens sample [Figure 7.7(a)][113]. Therefore, the second metalens sample is called *q*-MS. In addition, the *q*-MS has a diameter of 4.5mm to increase the brightness of the FOV edge. As shown in Figure 7.6(b), to effectively collecting the light scattered from the off-axis object point, the *q*-MS must have a larger diameter than the t-MS [114]. Otherwise, the edge light energy would be lost in the imaging system. The focal length of the *q*-MS is 45mm for achieving high magnifications.

$$\Phi_q(f, \rho) = -\frac{\pi r^2}{\lambda f} \quad (7.2)$$

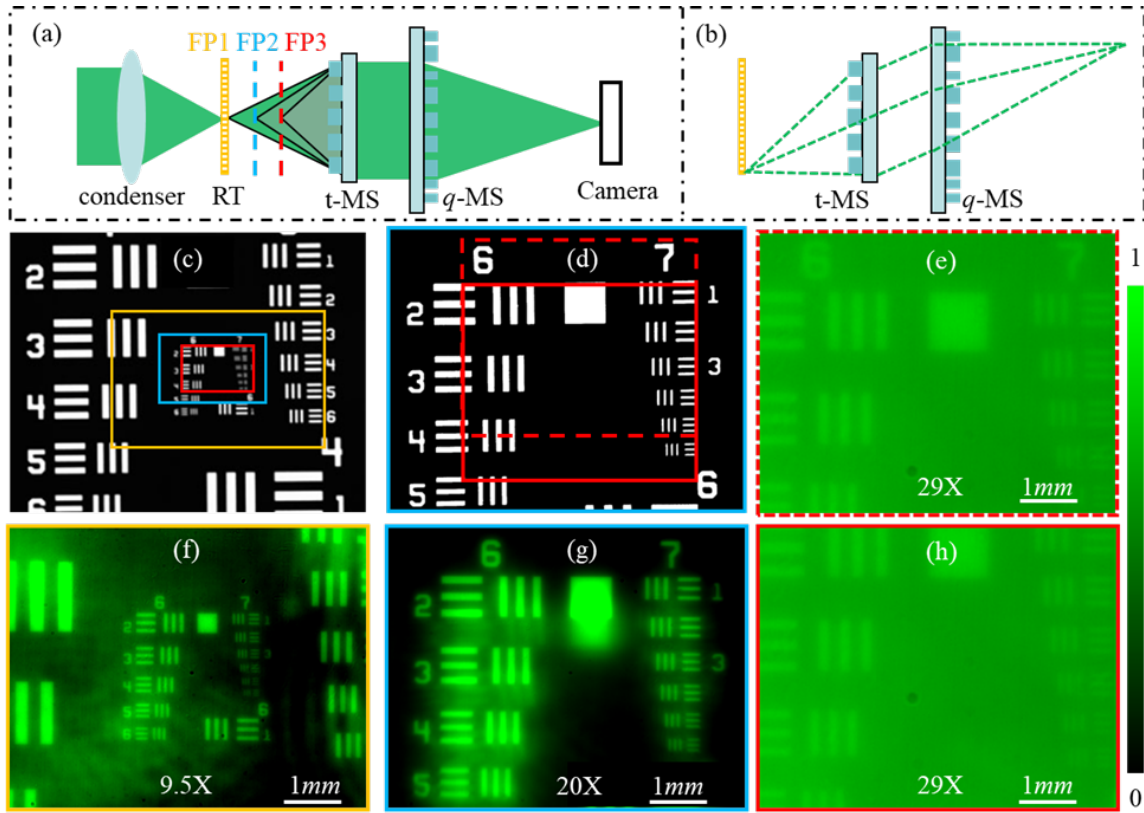


Figure 7.6 Experiment on integrated tri-magnification microscope.

(a) optical configuration; (b) Optical path of wide FOV imaging; (c) and (d) indicate the imaged FOV for each focal plane; (f) – (h) are the captured images when the RT is respectively placed at $f = 6\text{mm}$, 3mm , and 1.9mm ; (e) is the second image captured at $f = 1.9\text{mm}$.

As shown in Figure 7.1(c, d), the two metalens samples are integrated together by a 3D printed holder. As the holder is printed using transparent material, the light ray (i.e., stray light) out of the t-MS region would go into the q-MS and imaged to the camera, which would degrade the integrated microscope's imaging quality. Therefore, the central region of the holder is stained to be black to block the stray light. Based on the holder, the two metalens samples have a separation of 5mm.

As shown in Figure 7.6(a), to realize intensive illumination, the collimated light from a 520nm LED is focused onto the RT via a condenser lens. The condenser lens and RT are mounted together so that they can be moved from focal plane 1 (FP1) to focal plane 3 (FP3). As the integrated microscope is an infinity-corrected configuration, once the RT is placed in the three focal planes, it can be imaged to the focal plane of the q-MS. Therefore, a camera is placed at the q-MS focal plane to obtain the images.

Figure 7.6(f - h) illustrates the captured whole images when the RT is placed at $f = 6\text{mm}$ [focal plane 1 marked in orange in Figure 7.6(a)], 3mm [focal plane 2 marked in blue in Figure 7.6(b)],

and 1.9mm [focal plane 3 marked in red in Figure 7.6(b)], respectively, and the measured FOVs are limited by the camera's sensor size (6.4mm \times 5.12mm). The imaged regions as well as the FOVs of each focal plane are marked in orange, blue, and red on a ground truth image [Figure 7.6(c)]. As the red FOV ($674\mu\text{m} \times 539\mu\text{m}$) is smaller than the blue one ($320\mu\text{m} \times 256\mu\text{m}$) which is smaller than the orange one ($221\mu\text{m} \times 177\mu\text{m}$), the FOV goes down with the RT being moved from $f = 6\text{mm}$ [Figure 7.6(f) orange border] to $f = 1.9\text{mm}$ [Figure 7.6(h) red border]. Furthermore, it means that the magnifications go up with moving the RT from $f = 6\text{mm}$ focal plane [Figure 7.6(f)] to $f = 1.9\text{mm}$ focal plane [Figure 7.6(h)]. Based on quantitative calculation, the magnifications for three images are respectively 9.5X, 20X, and 29X, which are around 1.3 times of the expected magnifications of 7.5X, 15X, and 22.5X. The expected magnifications are evaluated by dividing the focal length 45mm of the *q*-MS by the three focal length 6mm, 3mm, and 1.9mm. The slightly defocus of the camera contributes to the magnification errors. When the RT is placed in the focal plane 3, as indicated by the Figure 7.6(d), the imaging region is changed from the red solid rectangle to the red dashed rectangle for obtaining solid evidence of the imaging position (i.e., the group and element number).

Except for the magnification, the imaging resolution of integrated microscope is evaluated as well. From the Figure 7.6(f), the element 5 in group 7 can be resolved with a high contrast, which indicates that the integrated microscope can realize a diffraction-limited resolution of 203.2lp/mm in the whole FOV at the focal plane 1 (focal length = 6mm, NA = 0.1). As the other two focal points have diffraction-limited FWHM as well, it is conceived that the integrated microscope can achieve diffraction-limited resolutions (322.5lp/mm and 456lp/mm) at the focal planes 2 and 3 as well, while the imaging contrast of the focal plane 3 is lower.

7.5 Design of *q*-MS and fabrication

As the *q*-MS works as a tube lens in the integrated microscope, the *q*-metalen needs to polarization-independently focus incident light to a focal point. Therefore, an isotropic meta-atom ($H = 800\text{nm}$, $P = 350\text{nm}$, and $W = L$) library [Figure 7.7(a)] is built to design the *q*-MS.

As shown in Figure 7.8, the metalens samples are fabricated on a double-side polished SiO_2 wafer. The wafer is firstly cleaned in NMP for 10mins and IPA for 10min. Then, a layer of Si_3N_4 (800nm in thickness) is deposited with a rate of 25nm/min via PECVD at 350°C. The refraction index and absorption coefficient of the PECVD Si_3N_4 are illustrated in Figure 7.7(a). 300nm ZEP520A resist is spin coated on the wafer and baked on a hot plate for 3mins at 180°C. Subsequently, metalens pattern is defined by the e-beam lithography (EBL) and develop process in ZED solution. As the hard mask, a 35nm-thick Cr layer is coated on the substrate by e-beam evaporation and followed by a lift-off in NMP. Consequently, the designed patterns are

transferred to the Cr layer. Then, the wafer with the patterned Cr layer is etched by reactive ion etching (RIE) with a rate of 27nm/min. Finally, metalens samples are obtained after removing Cr layer via Cr etchant. More details on fabrication can be found in Appendix B.

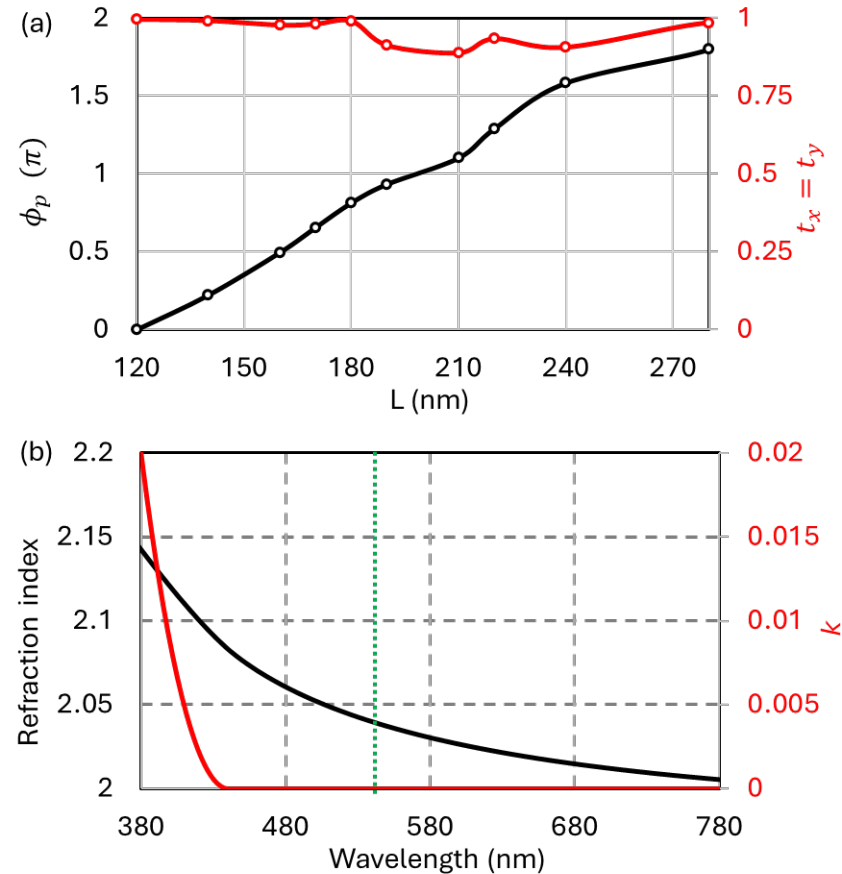


Figure 7.7 (a) meta-atom library for q-MS; (b) Index of PECVD Si_3N_4 .

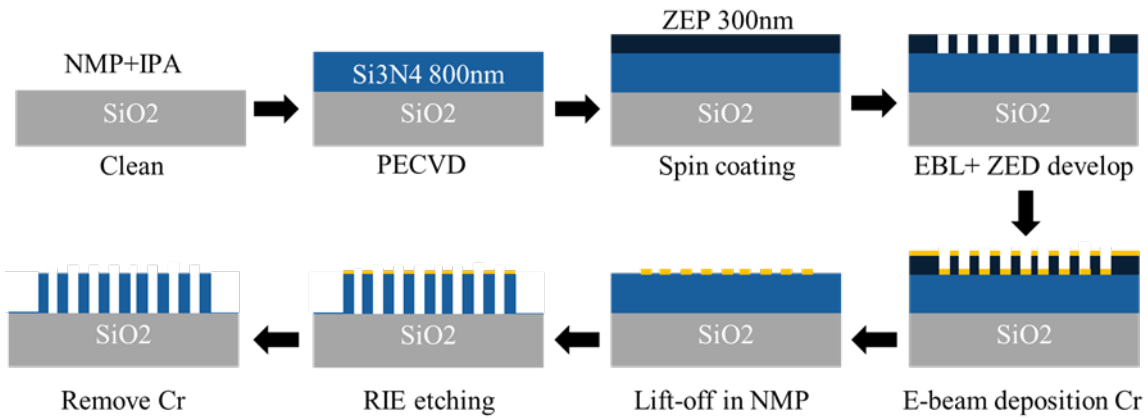


Figure 7.8 Fabrication flow of Si_3N_4 metalens.

7.6 Conclusion

Based on the non-classical spin-multiplexing working regime, a Si_3N_4 t-MS sample with a diameter of 1.2mm is designed and obtained in experiment for the first time. Three diffraction-

Chapter 7

limited focal points are achieved in experiment, and the NAs of three focal points are 0.1, 0.2, and 0.3, respectively. It is demonstrated that a commercial Nikon microscope could realize three magnifications with a fixed objective lens by using the t-MS sample for singlet imaging. The broadband imaging performance of the t-MS sample is investigated, and the chromatic aberration's influence on imaging effect is analyzed. Finally, an infinity-corrected microscope with three high magnifications of 9.5X, 20X, and 29X is integrated to a dimension of centimeter level by using the t-MS sample as an objective lens. To realize large FOV and diffraction-limited imaging performance, a *q*-MS sample with a quadratic phase profile and a diameter of 4.5mm is fabricated and used as the tube lens in the integrated microscope system.

Chapter 8 Simultaneously chiral and achiral microscope

8.1 Introduction

Chirality refers to some biological and chemical species which cannot be superimposed on their mirror image like human's right and left hands [115, 116]. The chirality can contribute to the biological and chemical species's flavor, odor, effectiveness, and safety when some molecules are made of same chemical elements and bonds [117]. Currently more than half of available biomedical drugs on the market are chiral, thus, chirality identification of biochemical samples plays an important role in drug discovery [118, 119]. Chiral imaging as a fast and effective chirality identification is attracting increasing attention in biochemical and optical field [56, 63, 120]. Moreover, the polarization information obtained via chiral imaging can give us more details of the imaged object [56, 57]. For instance, we can see strong difference between beetle's left-hand and right-hand images obtained via a chiral imaging system, because the beetle's exoskeleton strongly reflects left-hand circularly polarized (LCP) light while absorbing more right-hand circularly polarized (RCP) light [57].

Conventionally, a chiral imaging system relies on cascading multiple optical components in a complicated setup, which is bulky also reduces the imaging quality and resolution. In the past ten years, varieties of optical imaging systems are experiencing a lightweighting and high-compact revolution benefiting from the fast development of flat metalens [13]. As a flat optical device, metalens consisting of an array of subwavelength nanostructures on a flat substrate can be used for arbitrarily engineering the incident light beam's amplitude [121], phase [26], polarization [7], and frequency [8]. The research progress on metalens for compact multi-functional imaging systems has been reviewed in some high-quality papers [11, 13, 52, 71, 122]. Here, we only focus on the metalens' application in chiral imaging systems. A multispectral chiral imaging metalens is proposed to simultaneously image the LCP and RCP light scattered by the object based on PB phase and two interweaved sets of TiO_2 nanopillars [57]. With the development of spin-multiplexing metalens, the metalens composed of one set of nanopillars are demonstrated to simultaneously focus the LCP and RCP light at different position in visible [123], near-infrared [124], [125], and Terahertz spectrum [125].

It should be noted that the amplitude information of the target species is also important in biological and chemical research [5]. Therefore, integrating the chiral imaging and achiral imaging system into one metalens would attract more attentions across the biological and chemical society. While it is claimed that the simultaneously achiral and chiral imaging is achieved via a

200 μm -diameter plasmonic metalens in a reflective configuration, the two imaging channels of the metalens make it cannot simultaneously obtain the LCP, RCP, and achiral images [124]. In addition, the reported metalens sample is fabricated in a CMOS-incompatible way and works in the wavelength of 1550nm [124]. Therefore, there is no report on simultaneously achiral and chiral imaging based on visible metalens.

To show the merit of non-classical spin-multiplexing regime, a tri-channel Si_3N_4 metalens is demonstrated to realize simultaneously achiral and chiral imaging in a transmissive configuration (Figure 8.1). Moreover, a high magnification of 53 times and a diffraction-limited resolution are achieved in this chapter. In addition, the 1.2mm-diameter metalens is composed of one set of Si_3N_4 nanopillars and fabricated following a CMOS-compatible process, which makes the tri-channel metalens can be scale-up with low cost in both time and budget.

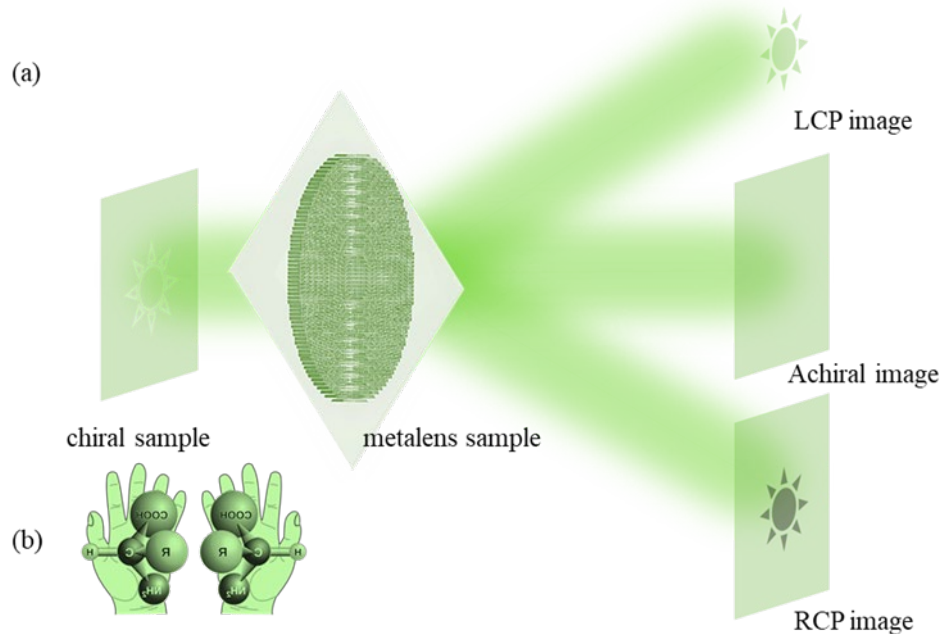


Figure 8.1 Conceptual figure of simultaneously achiral and chiral imaging.

(a) The imaged sample is transparent and has a different chirality across the field of view. The central sun region is LCP, and the other region in RCP; (b) Chirality of chemical molecular.

8.2 Metalens design and characterization

As shown in Figure 8.1, the light beam scattered by a chiral sample [Figure 8.1(b)] can be imaged into three channels according to their chirality (i.e., LCP and RCP images) and polarization-independent transmission (i.e., achiral image). Specifically, for a transparent sample having opposite chirality, the achiral image would have a uniform intensity distribution. Meanwhile, the LCP region (e.g., the central region marked by a sun in Figure 8.1) would be imaged to the LCP

channel, the other region would be imaged to the RCP channel, and the LCP region would be absent from the RCP image (i.e., the dark sun in the LCP image of Figure 8.1). To realize the above imaging function, the tri-channel metalens is required as shown in Figure 8.2(a). The metalens needs to focus incident light beam at three different positions in a same plane. The LCP and RCP focal points are polarization dependent for chiral imaging, and a polarization-independent focal point (i.e., achiral focusing) for realizing achiral imaging.

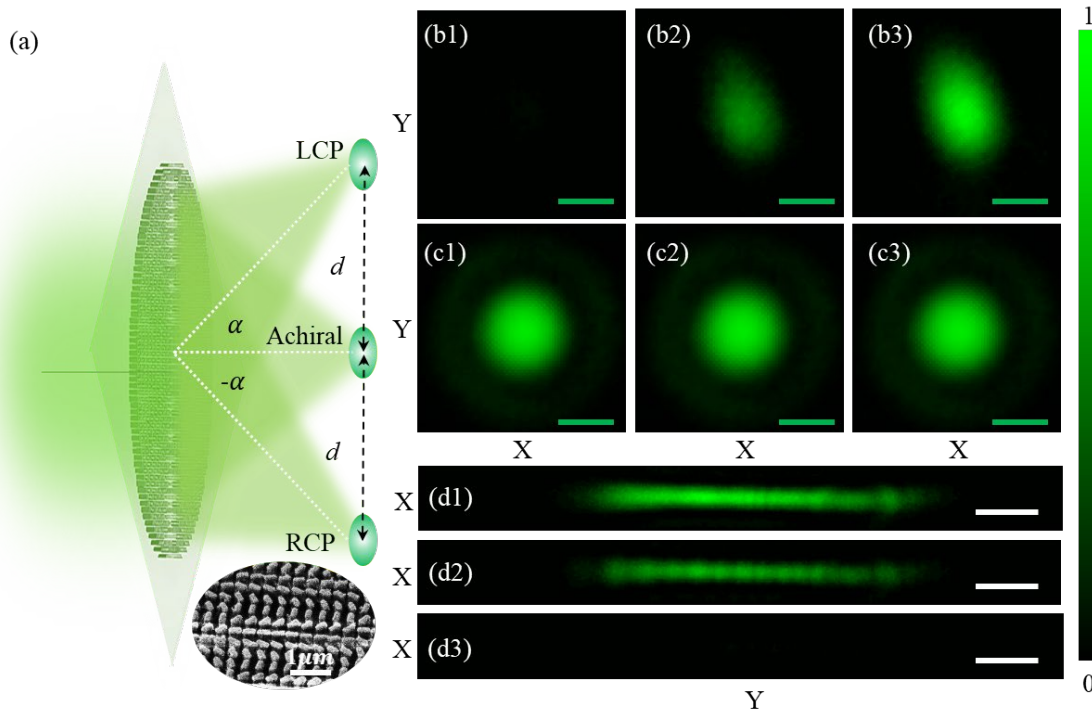


Figure 8.2 Working (a) and results (b - d) of tri-channel metalens.

(b1) – (b3) [(d1) – (d3)] are the measured LCP [RCP] focal points with tuning the laser beam from LCP to LP and to RCP; (c1) – (c3) are the achiral focal points. The green scale bars in (b1) – (c3) are $3\mu m$, and the white scale bars in (d1) – (d3) are $10\mu m$.

Based on the non-classical spin-multiplexing working mechanism (see section 2.2.3) and the meta-atom library in Figure 7.3, the Si_3N_4 metalens can be designed after determining the target phase profiles. As shown in Figure 8.2(a), to obtain an on-axis achiral focal point, a hyperbolic phase profile Φ_A [Eq. (3.1)] is polarization-independently encoded to the incident light beam via the propagation phase ϕ_p . In this chapter, the working wavelength $\lambda = 520nm$, target focal length $f = 6mm$ [Figure 8.3(a)]. Then, as shown in Figure 8.3(b), an off-axis hyperbolic phase profile Φ_L [Eq. (4.1)] where the focusing tilt angle $\alpha = 10^\circ$ [Figure 8.2(a)] is imposed to the LCP channel. Therefore, a large separation distance $d = f \times \tan(\alpha) = 1.05mm$ [Figure 8.2(a)] can be obtained to avoid the overlap of achiral and chiral images. According to the working mechanism, a phase profile $\Phi_R = 2\Phi_A - \Phi_L$ [Figure 8.3(c)] can be encoded to the RCP channel at a same time.

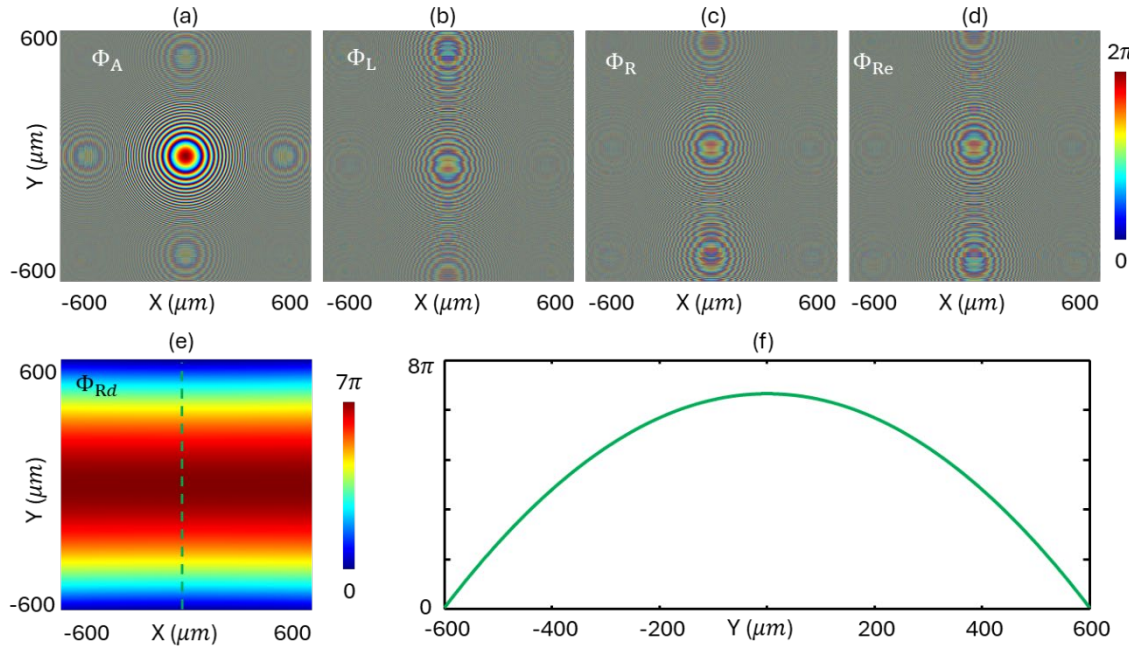


Figure 8.3 Phase profiles for tri-channel metasurface.

(a) – (c) are the phase profiles Φ_A ($f = 6\text{mm}$), Φ_L ($f = 6\text{mm}, \beta = 10^\circ$), and $\Phi_R = 2\Phi_A - \Phi_L$ encoded on the metasurface sample, (d) is the expected tilt focusing phase profile Φ_{Re} ($f = 6\text{mm}, \beta = -10^\circ$) with a tilt angle of -10° . (e) shows the phase difference $\Phi_{Rd} = \Phi_R - \Phi_{Re}$ between the real encoded Φ_R and expected Φ_{Re} , (f) is the 1D phase profile of the Φ_{3d} ($X = 0$) in the Y-direction.

To investigate the focusing performance of the RCP channel, an expected off-axis hyperbolic phase profile Φ_{3e} [Eq. (4.1)] with a tilt angle $\alpha = -10^\circ$ is demonstrated in Figure 8.3(d). Then, the unwrapped phase difference $\Phi_{Rd} = \Phi_R - \Phi_{Re}$ can be obtained and shown in Figure 8.3(e). As the peak-valley value of phase difference Φ_{Rd} is only 7π and much smaller than the expected phase profile Φ_{Re} . The Φ_R can be regarded as an estimated phase profile of the Φ_{Re} . Therefore, the RCP channel would achieve a focal length of 6mm and a focusing tilt angle of -10° , which is experimentally verified. The phase difference Φ_{Rd} varying along Y direction [Figure 8.3 (e) and Figure 8.3(f)] is the fundamental reason why the RCP focal point is enlarged along the Y direction [Figure 8.2(d)].

A metasurface sample with a diameter of 1.2mm is fabricated following the CMOS-compatible process [Figure 7.8] and measured by the home-made microscope (Figure 7.4) working in the wavelength of 520nm.

As shown in Figure 8.2(b - d), three focal points at the target focal plane which is 6mm away from the metasurface's surface are experimentally obtained. Therefore, the focal length of three focal points is 6mm in experiment. With tuning the laser beam from being LCP to LP and to RCP, the LCP focal point's intensity increases to a maximum [Figure 8.2(b1) to (b3)], and the RCP focal

point's intensity deceases to a minimum from a maximum value [Figure 8.2(d1) to (d3)], which demonstrates the chirality of these two focal points. In addition, the on-axis focal point [Figure 8.2(c1) to (c3)] doesn't change with tuning the incident laser's polarization, which means that this focal point is achiral. The FWHM of the achiral focal point is measured to be $3.2\mu m$ which is corresponding to the diffraction limitation of a NA of 0.1. In addition, the two achiral focal point's FWHM is diffraction-limited $3.2\mu m$ as well along the X-direction. As two chiral focal points are formed via inclined focusing [Figure 8.4(a) and Figure 8.4(c)], two chiral focal points' FWHM is larger than $3.2\mu m$ in the Y-direction. The enlarged RCP focal point in the Y-direction results from the phase difference Φ_{Rd} [Figure 8.3(e)]. From the focusing process shown in Figure 8.4, the focusing tilt angle of the LCP and RCP channels can be determined to be $\pm 10^\circ$.

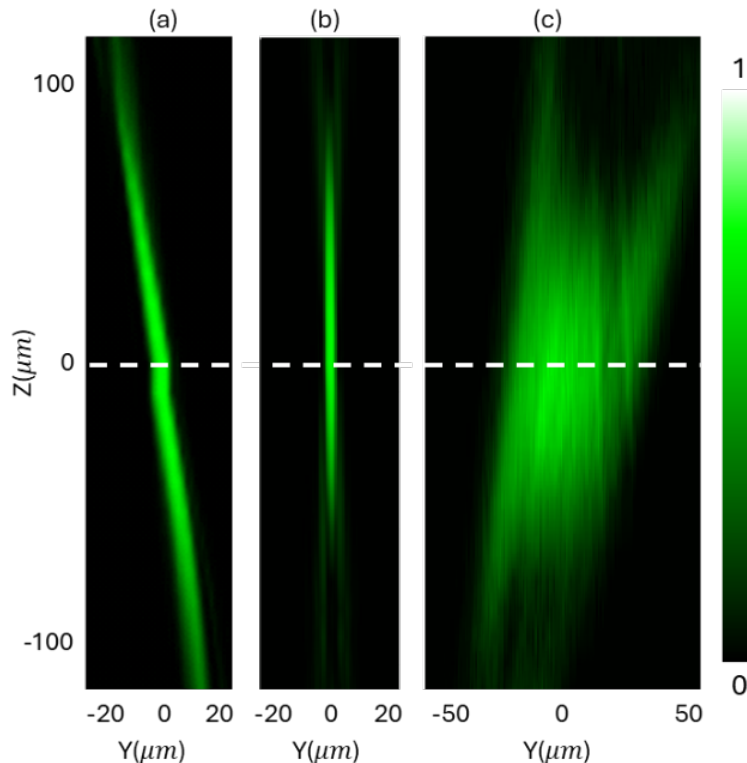


Figure 8.4 Focusing process of the LCP (a), achiral (b), and RCP (c) channels.

8.3 Demonstration of tri-channel microscope

8.3.1 Simultaneously achiral and chiral imaging

Based on this metalens sample, a simultaneously chiral and achiral microscope system is demonstrated. As shown in Figure 8.5, the microscope system works in a transmissive configuration, and a USFA 1951 resolution object is illuminated by a focused 520nm laser beam, the scattered light from the RT is collected by the metalens sample (MS) and imaged to a white board (WB). The imaged object is illuminated by a focused 520nm laser beam via the lens L1, and

the polarizer and QWP are placed for controlling the laser beam's polarization state. In addition, a ruler is placed in front of the WB to calibrate the size of the achiral and chiral images as well as the magnification of the microscope system.

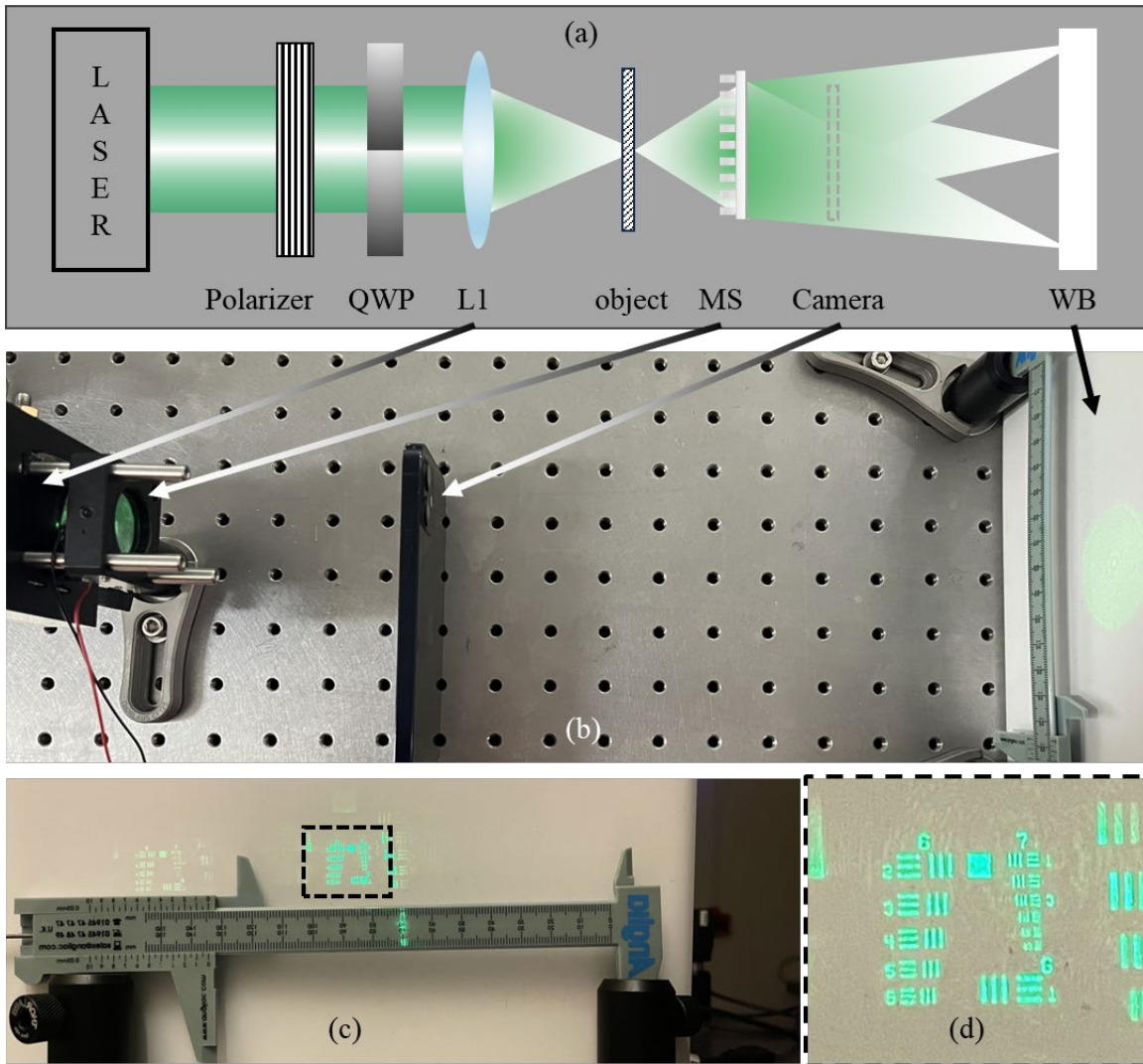


Figure 8.5 Simultaneously achiral and chiral microscope.

(a) Optical configuration of the metalens-based microscope for achiral and chiral imaging, (b) the experiment setup, (c) the initial picture captured by the iPhone camera, (d) is the zoom in picture of the marked region in (c) which shows the imaging resolution of $3.1\mu m$.

In experiment, the object is placed 6.11mm away from the front surface of the metalens sample (i.e., the object distance equals to 6.11mm), and a most clear image can be obtained when the white board is placed 325mm away from the metalens rear surface. According to the Gaussian imaging equation, the magnification of this microscope system can be calculated as 53.2 times. The imaging results are illustrated in Figure 8.6, which are taken by an iPhone 12 camera. The magnification is calibrated by placing a ruler in front of the white board. According to the ruler in captured images [Figure 8.5(c)], the microscope system's magnification is calibrated to be 53

times which meets well with the theoretical value of 53.2 times. The scale bars are corresponding to the calibrated size of captured images.

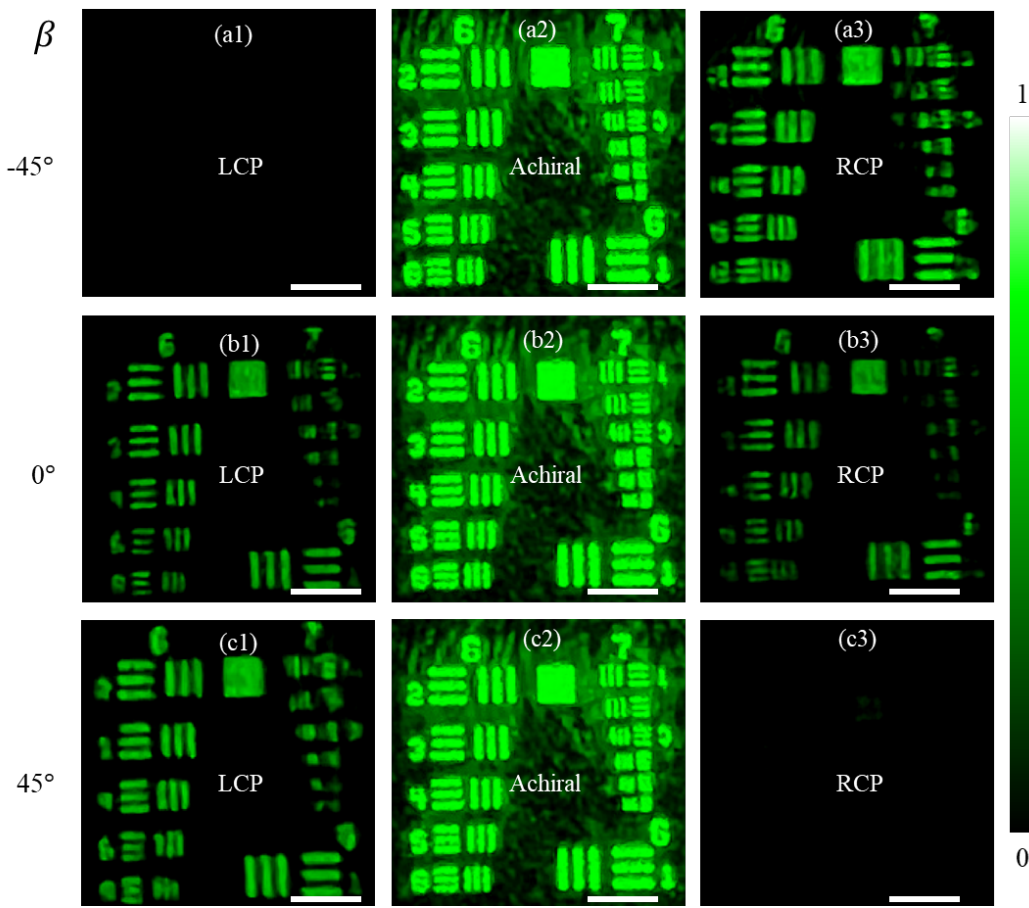


Figure 8.6 Imaging results of the microscope shown in Figure 8.5.

Simultaneously achiral (2nd column) and chiral imaging (1st and 3rd columns) of USAF 1951 resolution target with tuning the illumination light beam's polarization state from be RCP (1st raw) to LP (2nd raw) to LCP (3rd raw) via rotating a QWP. Scale bars: 4mm.

As shown in Figure 8.6, with rotating the QWP angle β from -45° (1st raw) to 0° (2nd raw) and to 45° (3rd raw), the image corresponding to the LCP channel (1st column) gradually gets brightest from dark, and the brightest image corresponding to the RCP channel (2nd column) gradually becomes dark, which demonstrates that the chiral imaging is achieved. Meanwhile, the images corresponding (the 2nd column in Figure 8.6) to the on-axis channel keeps steady with rotating the QWP, which shows that the achiral imaging channel works well. In one word, a simultaneously chiral and achiral microscope is achieved in transmissive configuration, and the microscope has a high magnification of 53 times and a diffraction-limited resolution of $3.1\mu\text{m}$ (i.e., 161.3lp/mm) because the element 3 in group 7 can be clearly resolved in the achiral imaging channel (the 2nd column in Figure 8.6).

8.3.2 All-optics chirality identification of chemical sample

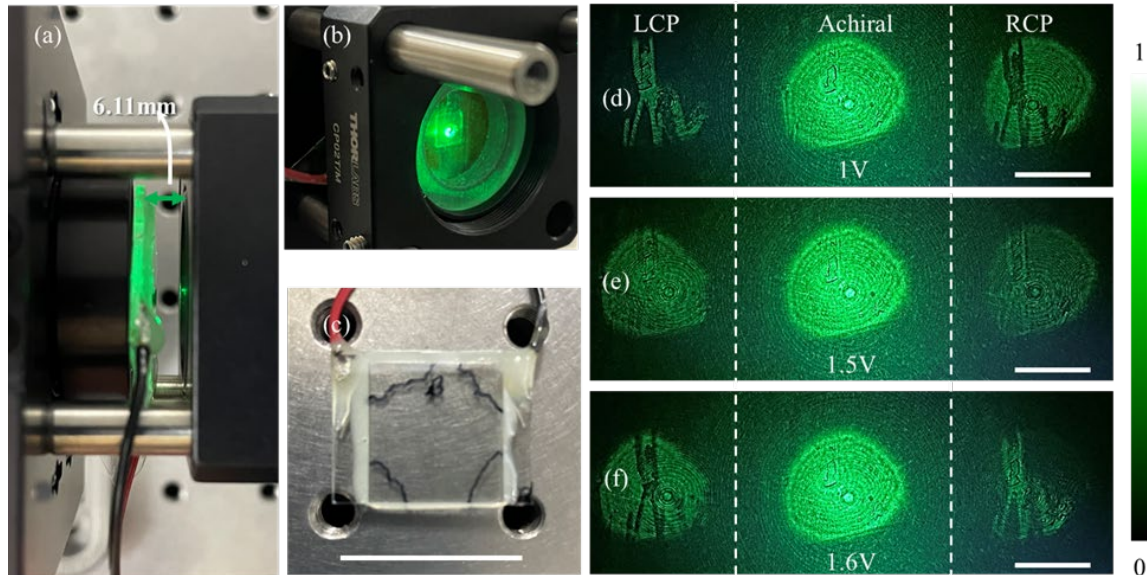


Figure 8.7 All-optics chirality identification of liquid crystal sample.

Experiment setup (a, b) for fast identifying the chirality of a transparent liquid crystal sample (c).

(d) – (f) are the imaging results with tuning the electrical voltage.

Lastly, the resolution object is replaced by a liquid crystal sample (LCS, which is fabricated by our cooperator) to test the microscope system's ability in fast detecting sample's chirality as shown in Figure 8.7(a - c). The LCS is totally transparent in visible spectrum as shown in Figure 8.7(c), while the fast-axis and slow-axis of the LC cells in one region (i.e., Region I) are opposite to the other region (i.e., Region II). It means that the chirality of Region I would be opposite to the Region II when a quarter-wave voltage is applied. In addition, when a half-wave voltage is applied, the whole LCS works as a half-waveplate.

In experiment, the achiral images [central images in Figure 8.7(d - f)] have a uniform intensity pattern with changing the load voltage. In contrast, two complementary images in the LCP and RCP channels are obtained as shown in the left and right region of Figure 8.7(d - f), when the quarter-wave voltage of 1V is applied. Specifically, the LCP channel obtains a bright image of the Region I [the left image in Figure 8.7(d)], and the image of Region I obtained by RCP channel is dark [the right image in Figure 8.7(d)]. It means that the chirality of Region I is right-hand, and the Region II has a chirality of left-hand, when the load voltage is 1V. With the load voltage being increased to be a half-wave voltage of 1.5V, three chiral and achiral channels obtain almost same intensity distribution [Figure 8.7(e)]. Continuously increasing the load voltage to the second quarter-wave voltage of 1.6V, the LCP and RCP channels respectively obtain a dark and bright image of the Region I [Figure 8.7(f)]. It means that the Region I is transferred to be left-hand chirality, and the Region II is transferred to be right-hand chirality. As the chirality of the LCS is

identified via an all-optics system, theoretically, the chirality identification speed can reach to light speed based on the tri-channel microscope.

8.4 Conclusion

To furtherly demonstrate the merit of utilizing non-classical spin-multiplexing regime, a new Si_3N_4 metalens is designed to simultaneously obtain achiral and chiral focal points on a same focal plane. A metalens sample is fabricated to obtain diffraction-limited three focal points. A simultaneously achiral and chiral microscope with a high magnification of 53 times and a diffraction-limited resolution is demonstrated in experiment. The all-optics chirality identification ability of the microscope is experimentally demonstrated by detecting a chemical sample's chirality. This work would boost the metalens' imaging applications in biological and chemical fields. In addition, by exploring the working mechanism in non-classical spin-multiplexing regime, the CMOS-compatible Si_3N_4 is adopted for the multi-functional metalens as well as imaging system, this research would pave the way of utilizing low-contrast material for advanced imaging system.

Chapter 9 Hybrid calculation model and prototype of LOMS

9.1 Hybrid calculation model

9.1.1 Introduction

Several numerical calculation methods, including the transfer matrix (T-matrix) method, the finite difference in time-domain (FDTD) method, the discrete dipole approximation (DDA) method, the finite element approach (FEM), and the Maxwell Stress Tensor (MST) method, have been adopted to calculate the optical force and torques in previous studies [126-130]. Because each method mentioned above has cons and pros, to take advantage of the complementary properties of different techniques, hybrid approaches [131, 132] have also been developed to calculate optical forces and torques on non-spherical particles. For example, a powerful dynamic simulation model is used to find plausible equilibrium orientation landscapes of micro-and nano-spheroids of varying size and aspect ratios based on a hybrid DDA and T-matrix method [132]. But it is difficult to calculate optical torques and forces via the hybrid method based on DDA and T-matrix method, when a non-spherical particle is levitated by a metalens-based LOMS with tailored trapping potential (e.g., a trapping potential with both SAM and OAM). Meanwhile, based on the application requirement, levitating nano- or micro-particles by a metalens-based LOMS [133-135] with tailored trapping potential has been a new research trend because of several advantages. For example, the optical tweezer based on SAM and spanner based on OAM has been integrated into one identical device by engineering a single layer metalens [39, 136]. Therefore, it is necessary to propose a new robust model to calculate the optical force and torque in a metalens-based LOMS.

9.1.2 Hybrid FDTD and DDA method

To accurately calculate the optical torques exerted on an aspherical particle trapped by a metalens-based LOMS, the FDTD method is adopted to calculate the electrical field distributions (\vec{E}) around the trapping centre based on the commercial Lumerical FDTD software. Then, the DDA method is adopted for the calculation of the optical forces (\vec{F}) and torques ($\vec{\tau}$) on the particle based on the \vec{E} distribution.

In FDTD simulation, as shown in Figure 9.1, the incident optical beam is set as a forward propagating (along Z-direction) plane wave with a circular polarisation (i.e., $\vec{E}_i = E_x + iE_y$) and has

a wavelength of $1.550\mu\text{m}$. To build an LCP beam, I set an x-polarized plane wave source E_x with a phase of 0 degrees and a y-polarized plane wave source E_y with a phase of 90 degrees. In addition, the amplitudes of both E_x and E_y are 1V/m . Then, the incident optical beam is focused by a high NA metalens. To effectively trap the nanoparticle, the centre of the nanoparticle is placed at the focal point. The origin O_2 is set at the focal point f (marked by a solid black dot on the Z-axis) in Figure 9.1(a). The nanoparticle is surrounded by a vacuum with the refractive index $n_1 = 1$. By taking the calculation time and accuracy into consideration, a cube area centred on the focal point (i.e., the f point on the Z-axis) is meshed into 5nm in three dimensions (3D), and other simulation areas are meshed into 155nm . Note that the particle should be fully covered by the cube area.

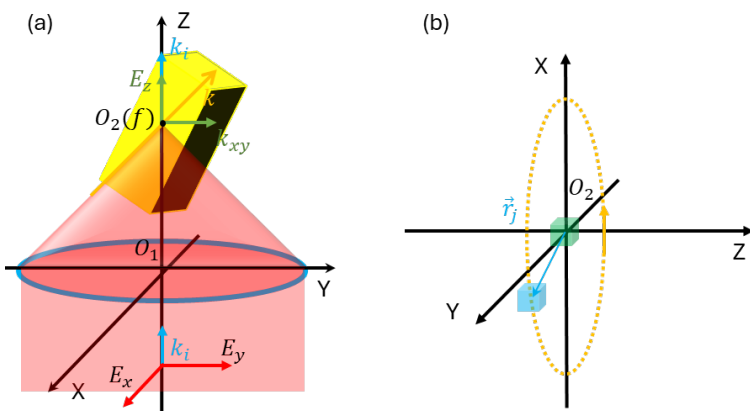


Figure 9.1 Schematic illustrating of a metalens-based LOMS.

An electrical field monitor is added to get the 3D field distribution in the cube area, that is, the electrical field distributions (\vec{E}) around and inside the nano-dumbbell. An index monitor is used to get the 3D spatial distribution of the refraction index (n), which will be used to calculate optical forces and torques based on the DDA method. It should be noted that the \vec{E} and n distributions are discrete databases in a 3D cubic array. According to Figure 9.1(a), for a given incident optical beam, the geometric parameters and spatial orientation angles of the nanoparticle will influence the \vec{E} and further result in different optical torques. Therefore, the parameter sweep function can be used to acquire the \vec{E} and n distributions for different morphological parameters of the nano-dumbbell. Then, they are imported into MATLAB for calculating the optical forces \vec{F} and torques $\vec{\tau}$ based on the DDA method.

Based on the principle of the DDA method, the nano-dumbbell should be presented by a 3D cubic array of N polarisable cells (i.e. the point dipoles) and the local electrical field $\vec{E}_j = (E_x^j, E_y^j, E_z^j)$ ($j = 1, 2, 3, \dots, N$) at each cell should be calculated based on the self-consistent equation at first. The nano-dumbbell is uniformly discretised by a mesh of 5nm used in FDTD calculation and the local electrical field \vec{E}_j could be acquired from the \vec{E} databases. It should be noted that, in the FDTD

method, the influence of the multiple scattering effects from the adjacent polarisable cells is contained for calculating each polarisable cell's local electrical field \vec{E}_j . Then, the dipole moment $\vec{p}_j = \alpha_j \vec{E}_j$ of each cell could be calculated, where the α_j is the polarizability of each cell, which could be expressed as Eq. (9.1) [129].

$$\alpha_j = \frac{\alpha_{CM,j}}{1 - i \frac{2}{3} k^3 \alpha_{CM,j}} \quad (9.1)$$

Where $k = 2\pi/\lambda$ ($\lambda = 1.55 \mu\text{m}$) is the wavenumber of the incident optical beam, $\alpha_{CM,j}$ is the Clausius-Mossotti polarizability of each cell and could be written as Eq. (9.2).

$$\alpha_{CM,j} = \frac{3d^3(\varepsilon_j - 1)}{4\pi(\varepsilon_j + 2)} \quad (9.2)$$

Where $d = 5\text{nm}$ is the period of the discretisation lattice, $\varepsilon_j = n_j^2$ is the relative permittivity of each cell of the nanorod and n_j is the refraction index, which has been acquired during the FDTD calculation.

Once the local electrical field \vec{E}_j and dipole moment \vec{p}_j are known, the time average of the optical force $\vec{F}_j = (F_x^j, F_y^j, F_z^j)$ [Eq. (9.3)] and torque $\vec{\tau}_j$ [Eq. (9.4)] exerting on each cell could be calculated as,

$$F_u^j = \frac{1}{2} \operatorname{Re} \left(\sum_{v=1}^3 p_v^j \frac{\partial (E_v^j)^*}{\partial u} \right) \quad (9.3)$$

$$\vec{\tau}_j = \vec{r}_j \times \vec{F}_j + \frac{1}{2} \operatorname{Re} \left[\vec{p}_j \times \left(\frac{\vec{p}_j}{\alpha_{CM,j}} \right)^* \right] \quad (9.4)$$

Where u and v stand for either x , y , or z , symbol $*$ denotes the complex conjugate, and \vec{r}_j is the position vector of the cell, as shown in Figure 9.1(b). The first term is usually called the extrinsic part of the optical torque (OAM), while the second term represents the intrinsic part of the optical torque (SAM). Here, it is necessary to clarify the difference between the OAM and SAM carried by the nano-dumbbell and the discretised cells. If only the SAM carried by the incident beam is transferred into the nanorod, the nanorod could spin around the Z-axis, as shown in Figure 9.1(b). However, the angular momentum carried by the cells [e.g., the blue cell in Figure 9.1(b)] which are not on the Z-axis is OAM expressed by the first term in Eq. (9.4), while that carried by the cells [e.g., the green cell in Figure 9.1(b)] on the Z-axis still is SAM expressed by the second term in Eq. (9.4). Therefore, both the SAM and OAM terms should be included in the calculation model [i.e., Eq. (9.4)] based on the DDA method.

Finally, total optical forces and torques applied on the nano-dumbbell could be obtained as the sum over all the cells of the individual forces and torques [Eq. (9.5)][137].

$$\vec{F} = \sum_{j=1}^N \vec{F}_j, \text{ and } \vec{\tau} = \sum_{j=1}^N \vec{\tau}_j \quad (9.5)$$

9.1.3 Accuracy validation

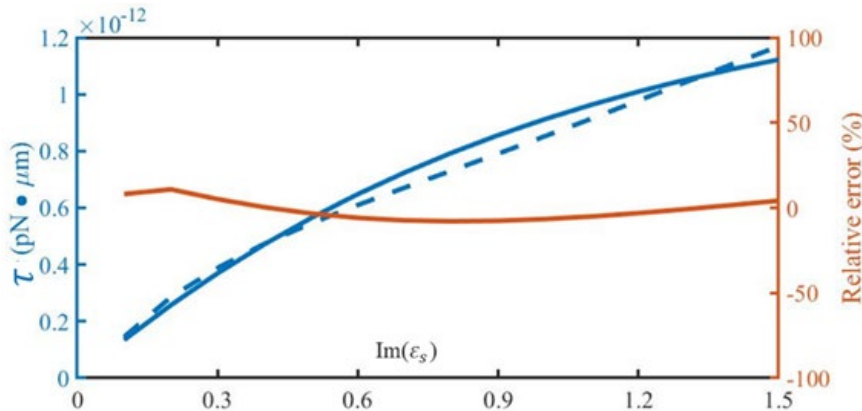


Figure 9.2 Optical torques vs $\text{Im}(\varepsilon_s)$ calculated by Mie-theory and the HFDM.

To validate the accuracy of the HFDM, this chapter first studied a particular case where an absorbing sphere is directly illuminated by an LCP plane wave, as an analytical solution of the optical torques on the absorbing sphere could be calculated by Mie-theory. The radius and real part of the permittivity ε_s of the sphere are set as 350nm and 2.25, respectively, and the absorbing property of the sphere is described by the imaginary part [$\text{Im}(\varepsilon_s)$] of the permittivity ε_s . Therefore, then the dependence of optical torques on the $\text{Im}(\varepsilon_s)$ is simulated. The simulation results are shown by the blue dashed line in Figure 9.2, while the solid blue line indicates the analytical values calculated by the Mie-theory [126]. The optical force and torque units are pN and $\text{pN} \cdot \mu\text{m}$, respectively.

It could be seen that the optical torques calculated by the HFDM and Mie-theory show identical dependency on the $\text{Im}(\varepsilon_s)$, and the absolute values of the relative errors are below 10% [i.e., the solid orange line, right y-axis in Figure 9.2]. In fact, an error below 10% is relatively small comparing the reported experiment's error of about 20%. For example, it is reported that an optical torque is theoretically predicted to be 2.0 $\text{pN} \cdot \mu\text{m}$ based on T-matrix method and is measured to be 2.4 $\text{pN} \cdot \mu\text{m}$ in the experiment [138]. It indicates that the HFDM could be utilised for the calculation of optical torques.

9.2 Invention of a metalens-based LOMS prototype

9.2.1 Introduction

Optical levitation of nanoparticles is a well-developed technique based on using force gradients induced by optical fields; this is the so-called optical tweezer approach. It is known that optically

levitated nanoparticles in vacuum can provide the basis for ultrasensitive sensors to measure physical parameters such as force, acceleration, and torque. For the avoidance of ambiguity of terminology between the field to be measured and the optical field used to trap a nanoparticle, in the following, field to be measured is referred as a physical field.

It is predicted that the mechanical quality factor (Q factor) of an optically levitated nanoparticle could be as high as 10^{12} and a Q factor of 10^{10} has been achieved experimentally [17], which is much higher than the Q factor ($\sim 10^6$) achieved using microelectromechanical system (MEMS) [139]. The extremely high Q factor and torque detection sensitivity make the precession motion of an optically levitated nanoparticle be suitable for detecting the gravity acceleration with high accuracy.

A drawback of known optical levitation systems is their bulk which makes them unsuitable for many practical applications. In addition, the spin direction of known optical levitation systems can't not be customized which makes the precession motion cannot be well controlled and not suitable for practical gravimeter.

In our invention, a metalens and its method of manufacture, the metalens being designed and fabricated to transform a laser beam into a pre-defined arbitrary optical field carrying spin angular momentum and/or orbital angular momentum in defined directions[140], which can be transferred to nanoparticles trapped by levitation in the optical field of the laser beam that has passed through the metalens [24], [137]. The metalens can be incorporated into an optical levitation system in which a nanoparticle can be trapped in the arbitrary optical field. Light intensity scattered from the trapped nanoparticle is then measured and used as a basis for measuring a physical field value.

9.2.2 Details on the prototype

As shown in Figure 9.3, the LOMS based on a dry particle launching method is mechanically constructed based on a vacuum chamber formed by the interior space inside a two-part housing 1, 2 comprising an upper part 1 and a lower part 2. (The labels upper and lower are arbitrary and made for ease of reference.) The upper and lower parts 1, 2 of the housing are connected to each other in a vacuum-tight manner by suitable clamping bolts 3 with the mating surfaces between the upper and lower parts 1, 2 of the vacuum chamber housing being provided with a suitable gasket or other sealing joint (not shown). Optical access to the vacuum chamber is provided by an optical fibre feedthrough 4 in the upper vacuum chamber housing part 1. Electrical access to the vacuum chamber is provided by an electrical feedthrough 5 in the lower vacuum chamber housing part 2. A non-evaporative getter (NEG) 6 is provided in the lower vacuum chamber housing part 2 to assist maintenance of the vacuum by removal of residual gas species from the

vacuum space. In use, the vacuum pressure is preferably better than 1E-6 mbar, which can be achieved by the NEG 6 which operates as a pump unit once the sensor is sealed. An external vacuum pump (not shown) may also be provided. The optical fibre feedthrough 4 is provided with a suitable collimator lens 7 for coupling into and/or out of an optical fibre (not shown) that may be attached, e.g., by a suitable ferrule, to the optical feedthrough 4.

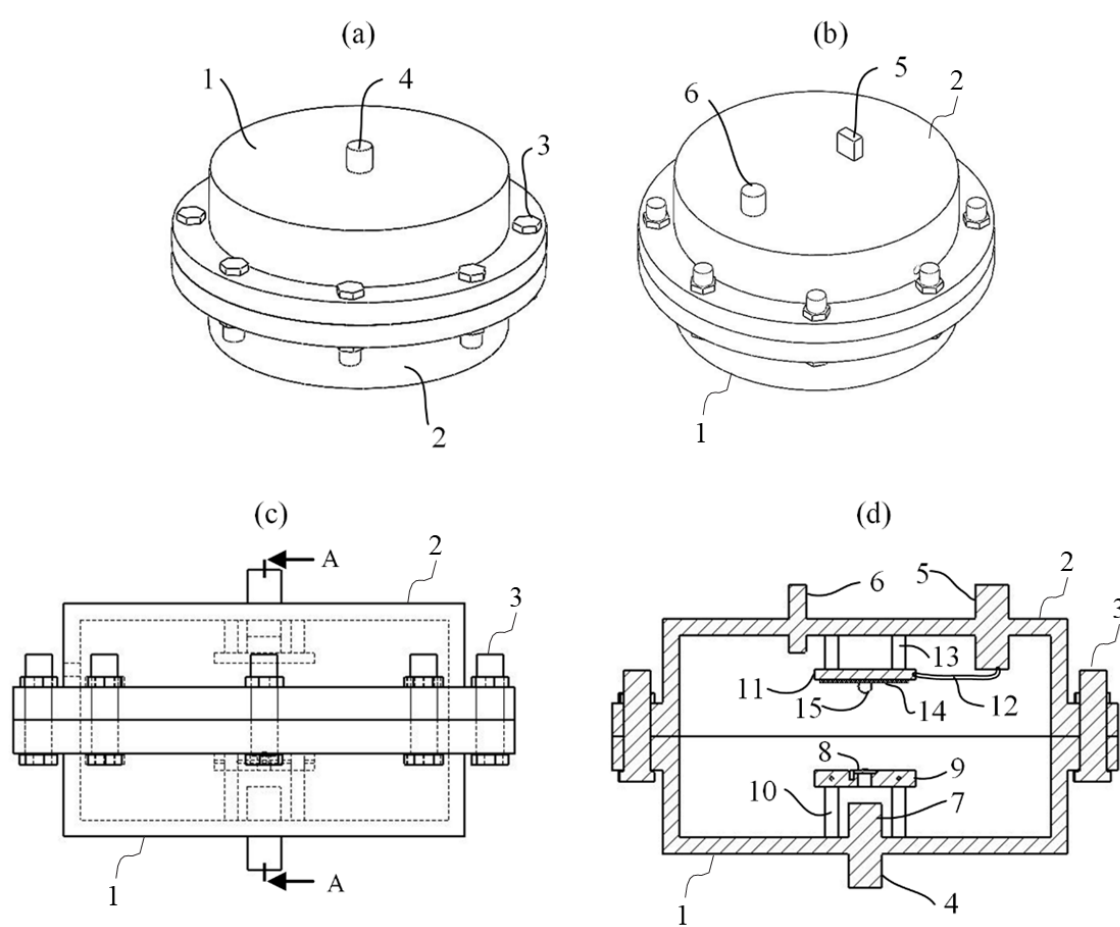


Figure 9.3 Prototype of the LOMS based on a dry particle launching method.

(a) and (b) are perspective views from below and above respectively, (c) is a side view, and (d) is a cross-section along line A-A of (c) showing internal details of the gravimeter

After the collimator lens 7, a continuous-wave, linearly polarized Gaussian laser beam (wavelength $\lambda=1550\text{nm}$) from the fibre laser source 21 is shaped to a collimated beam. A metalens 8 for manipulating the laser beam so that it functions to trap the nanoparticles is supported within the vacuum chamber via suitable holder parts 9, 10 (e.g., plinth 9 and legs 10) attached to an inside surface of the upper vacuum chamber housing part 1. A particle source 14, 15 for the nanoparticles to be optically levitated is arranged within the vacuum chamber mounted on a piezoelectric actuator 11, e.g. made of lead-zirconate-titanate (PZT), which in turn is supported by legs 13 (e.g. 4 of) that are secured by their distal ends to an interior surface of the lower vacuum chamber housing part 2 and whose proximal ends support the piezoelectric actuator 11. A typical particle source will contain of the order of 2000 x 2000 particles, with a

single nanoparticle being trapped for any given measurement. The piezoelectric actuator 11 is actuated with a suitable electrical control signal via an electrical wire connection 12 which is fed from an external controller (not shown) into the vacuum chamber via the electrical feedthrough 5. The particle source 14, 15 comprises an agglomeration of source nanoparticles which are embedded in a poly-fluoroethylene (PTFE) coated film 14 that acts as a substrate for holding the source particles prior to their release into the vacuum chamber. Embedding the nanoparticles to be levitated in the film 14 allows the nanoparticles to be directly loaded into the vacuum chamber and then released when needed by ultrasonic vibration of the piezoelectric actuator 11 on which the film 14 is mounted. The film 14 is inexpensive and easily replaceable.

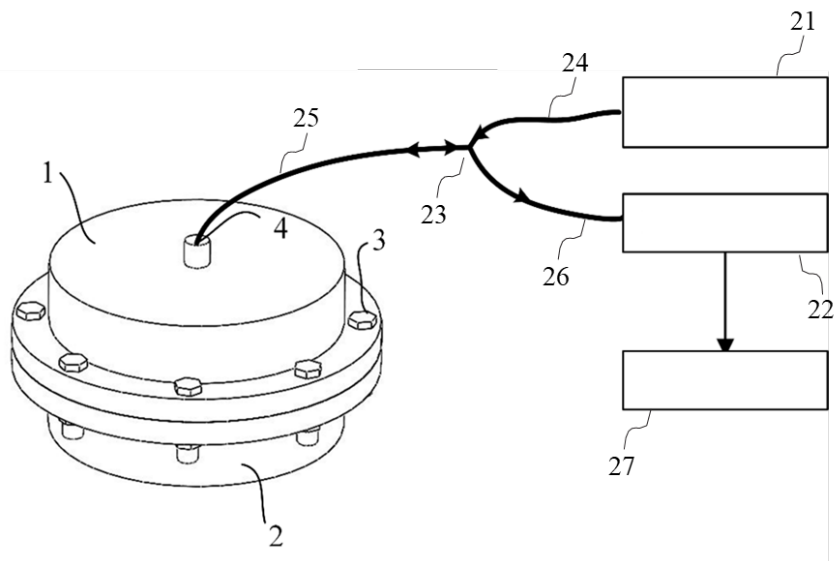


Figure 9.4 External components of the LOMS.

Figure 9.4 shows the external components connected to the LOMS in Figure 9.3 via the optical feedthrough 4. The output of a laser 21 is coupled to an optical fibre 24. The laser light is waveguided through the optical fibre 24 via an optical circulator 23 to another optical fibre 25 connected the optical feedthrough 4, so that the laser light provides an optical tweezer for trapping nanoparticles in the vacuum chamber. Light from the trapped nanoparticles is coupled out of the vacuum chamber via the optical feedthrough 4 and into the optical fibre 24. The coupled-out light is then routed via the optical circulator 23 to another optical fibre 26 and onto a photodetector 22. The photodetector 22 outputs an electrical signal for display and analysis on an oscilloscope 27.

Figure 9.5(a) is a perspective view of a LOMS according to an alternative embodiment based on the Laser-Induced Acoustic Desorption (LIAD) loading method; and Figure 9.5(b) is a cross-section showing internal details of the gravimeter. LIAD is a dry and vacuum compatible method for loading particles into optical traps. In the LIAD method, a pulsed laser beam is focused onto the back side of a substrate upon which particles are distributed. The pulse generates acoustic

shockwaves through thermo-mechanical stress to locally eject particles from the substrate. The particles are only ejected from the region of the laser focus. LIAD is suitable for launching dielectric particles of size from around 100 nm up to several micrometres at pressures down to 1 mbar. The gravimeter is mechanically constructed based on a vacuum chamber formed by the interior space inside a two-part housing 1, 2 comprising an upper part 1 and a lower part 2. (The labels upper and lower are arbitrary and made for ease of reference.) The upper and lower parts 1, 2 of the housing are connected to each other in a vacuum-tight manner by suitable clamping bolts 3 with the mating surfaces between the upper and lower parts 1, 2 of the vacuum chamber housing being provided with a suitable gasket or other sealing joint (not shown).

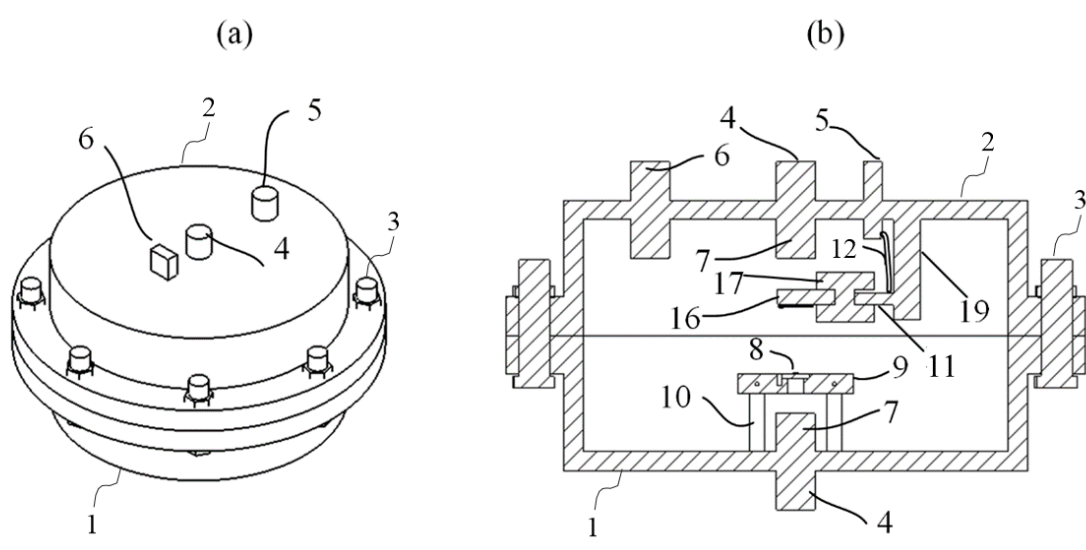


Figure 9.5 Prototype of the LOMS based on LIAD method.

Optical access to the vacuum chamber is provided by an optical fibre feedthrough 4 in the lower vacuum chamber housing part 2. Electrical access to the vacuum chamber is provided by an electrical feedthrough 5 in the lower vacuum chamber housing part 2. A non-evaporative getter (NEG) 6 is provided in the lower vacuum chamber housing part 2 to assist maintenance of the vacuum by removal of residual gas species from the vacuum space. In use, the vacuum pressure is preferably better than 1E-6 mbar, which can be achieved by the NEG 6 which operates as a pump unit once the sensor is sealed. An external vacuum pump (not shown) may also be provided. The optical fibre feedthrough 4 is provided with a suitable collimator lens 7 for coupling into and/or out of an optical fibre (not shown) that may be attached, e.g., by a suitable ferrule, to the optical feedthrough 4. A metalens 8 for manipulating the laser beam so that it functions to trap the nanoparticles is supported within the vacuum chamber via suitable holder parts 9, 10 (e.g., plinth 9 and legs 10) attached to an inside surface of the upper vacuum chamber housing part 1. The lower vacuum chamber housing part 2 accommodates the nanoparticle source components. A nanoparticle source chip 16 containing the nanoparticles is mounted on a linear translator 17 which in turn is actuated by a piezoelectric actuator 11 which receives control

signals from an external controller (not shown) via an electrical wire connection 12 that passes through the electrical feedthrough 5. A typical particle source will contain of the order of 2000 x 2000 particles, with a single nanoparticle being trapped for any given measurement. The piezoelectric actuator 11 may be made of lead-zirconate-titanate (PZT), for example.

A holder or mount 19 in the form of a spigot holds the PZT actuator 11 fixed in relation to the lower vacuum chamber housing part 2. The particle source 16 holds source nanoparticles prior to their release into the vacuum chamber. While the gravimeter of Figure 3 is based on the LIAD method, this is not the standard LIAD method. In a standard LIAD method, to align the laser beam relative to the nanoparticle source, the nanoparticle source chip 16 is mounted in a fixed position within the vacuum and the laser beam is movable by arranging the laser on a translation stage. In the gravimeter of Figure 3 on the other hand the nanoparticle source chip 16 is moved relative to a static laser beam since the nanoparticle source chip 16 is in direct or indirect contact to the piezoelectric element 11. The piezoelectric actuator 11 and linear translator 17 together form a translation stage that provides for linear motion to allow lateral displacement of the particle source 16 along a motion axis, optionally in two crossed motion axes for xy-motion. The translation stage of piezoelectric actuator 11 acts to change the relative position between the nanoparticle source chip 16 and the focal point of the static pulsed laser beam.

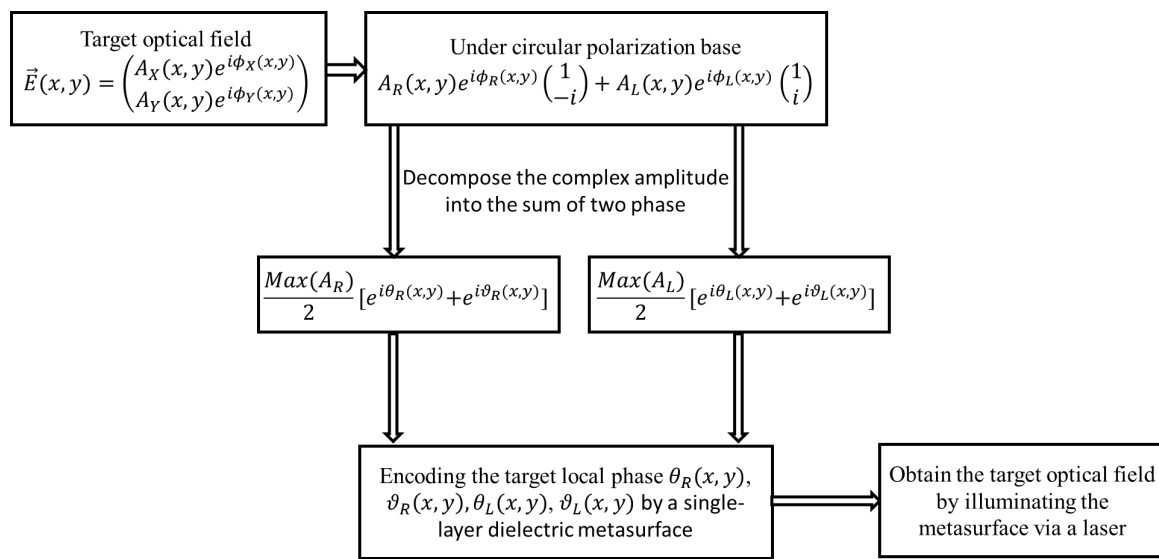


Figure 9.6 Design flow of a metasurface for generating arbitrary optical field.

A design method of the metasurface which is a key component in the invented prototypes (Figure 9.3 and Figure 9.5) is invented as well to generate an arbitrary optical field for flexibly defining the SAM direction of the trapping laser beam. As shown in Figure 9.6, both the complex amplitudes of the X- and Y-components of the target optical field are decomposed into circular polarization bases. As a result, the target optical field can be expressed by summing the complex amplitudes of the LCP and RCP components. Then, the complex amplitudes of the LCP and RCP are

reformulated as the sum of two phase terms. Finally, the target optical field is expressed by four phase terms θ_R , θ_L , ϑ_R , and ϑ_L . To encode the four phase terms into a single layer metasurface, we propose using one of two modulation methods as described below with reference to Figure 9.7 and Figure 9.8 respectively.

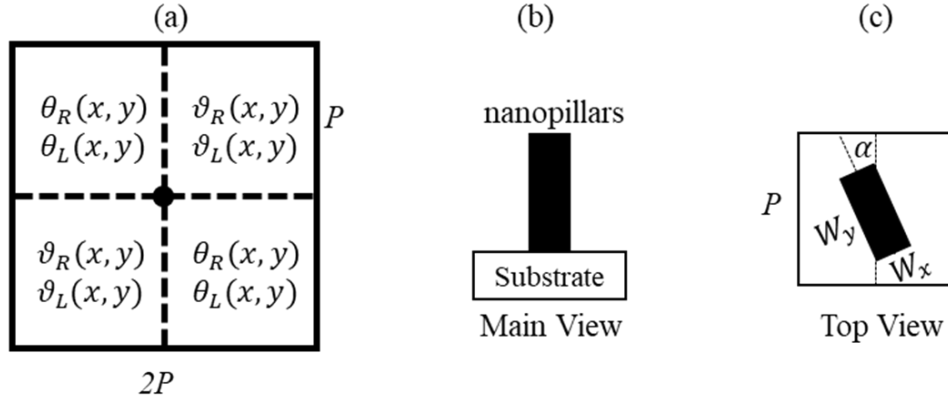


Figure 9.7 Space-multiplexing metasurface for generating arbitrary optical field.

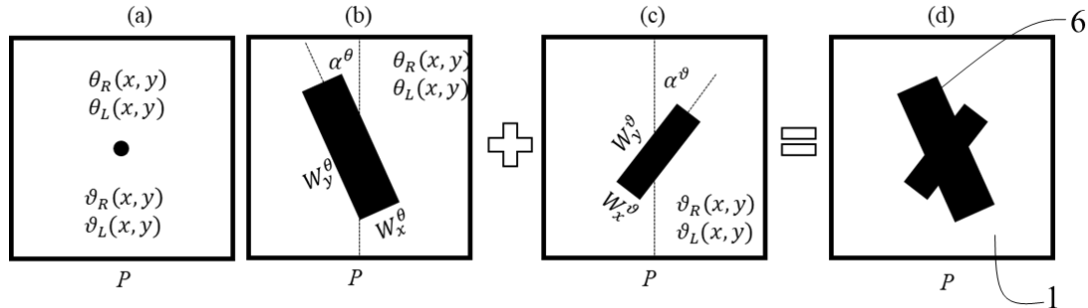


Figure 9.8 X-shaped meta-atoms for arbitrary optical field.

To simultaneously impose target phases on the LCP and RCP components, the meta-atoms used in Figure 9.7 and Figure 9.8 should be designed in the classical spin-multiplexing regime. Comparing the metasurface based on X-shape meta-atoms (Figure 9.8), a 4f filter system is required to be placed behind the spatial-multiplexing metasurface in Figure 9.7 for generating the target optical field.

9.2.3 Demonstration of generating arbitrary optical field

To verify the feasibility of the design method illustrated in Figure 9.6 and Figure 9.7, an a-Si metasurface sample is designed, fabricated (Figure 3.4), and measured in experiment. As shown in Figure 9.9(a), the metasurface sample targets at modulating laser intensity, as the phase and polarization modulation ability of a metasurface has been verified in chapters 3 – 8. Specifically, the metasurface sample aims at respectively generating the badge and logo of the University of Southampton for X- and Y-polarized incoming light. The ongoing light field from the metasurface is measured in the wavelength of 630nm and 520nm and demonstrated in Figure 9.9(b) and Figure

9.9(c). From the pictures shown in Figure 9.9, the metasurface can successfully generate the target optical field in a widely visible spectrum.

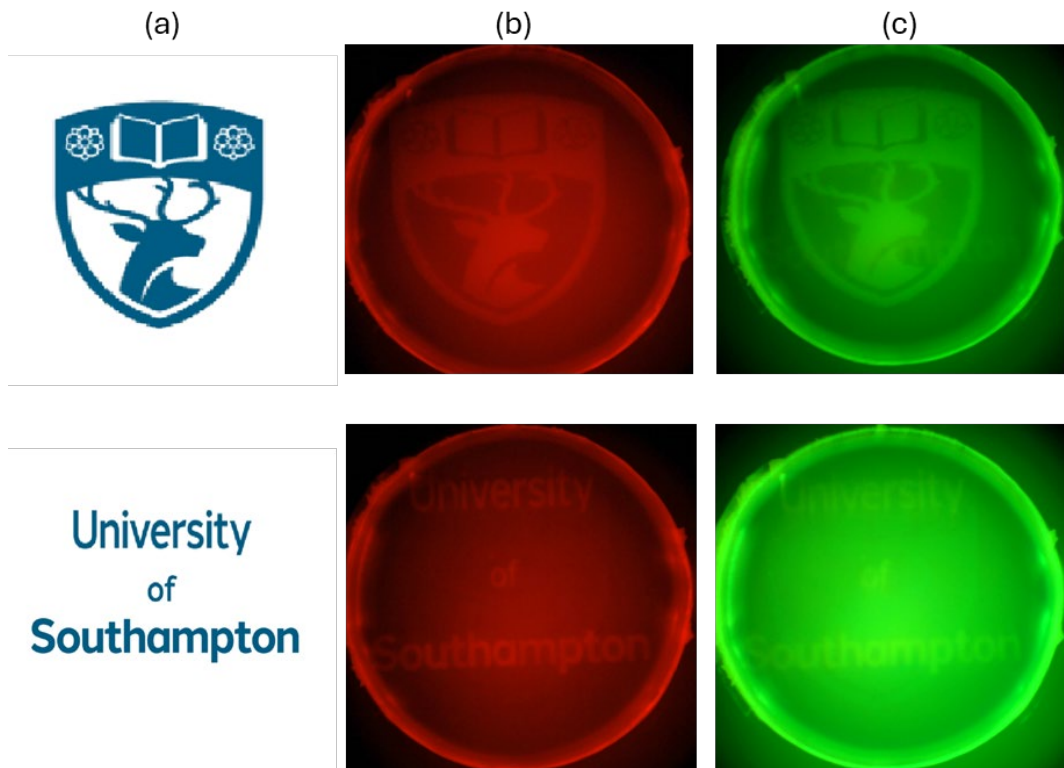


Figure 9.9 Demonstration of generating arbitrary optical field.

(a) The ground truth, (b) ongoing optical field in the wavelength of 630nm, (c) ongoing optical field in the wavelength of 520nm.

9.3 Conclusion

To accurately calculate the optical torques exerted on an aspherical particle levitated by a complexing optical field (e.g., the VVBs in chapter 6), a hybrid calculation method is proposed by combining the FDTD and DDA method. Then, to boost the commercialization of metasurface-based LOMS, two prototypes of a LOMS are invented in the second section where a metasurface design method of generating arbitrary optical field is proposed by combining the classical spin-multiplexing working mechanism and dual-phase holography. Based on the proposed method, the logo and badge of the University of Southampton can be dynamically generated in a widely visible spectrum.

Chapter 10 Summary and outlook

10.1 Summary

Following a short introduction of metasurface's research progress in chapter 1, the phase delay principle and light beam modulation mechanism of a subwavelength meta-atom is explored in chapter 2. Based on the phase difference between X-polarized and Y-polarized laser beam, the working regime of a metasurface is classified into three types: (1) polarization-independent regime where the phase difference equals to 0; (2) classical spin-multiplexing regime where the phase difference equals to π and the meta-atom serves as a half waveplate; (3) non-classical spin-multiplexing regime where the phase difference can be arbitrary value between 0 and π . Therefore, the design requirement of a metasurface in non-classical spin-multiplexing regime is lower than that of a metasurface in classical spin-multiplexing regime. However, it is theoretically figured out that the non-classical spin-multiplexing metasurface can achieve three working channels, while the polarization-independent and classical spin-multiplexing metasurface respectively has one and two working channels. The low design requirement and three working channels provide us with an opportunity of utilizing low-refraction-index material (e.g., Si_3N_4) to design multi-channel metasurface for achieving multi-functional imaging system. Starting from chapter 3, one application of polarization-independent metalens, three applications of classical spin-multiplexing metasurfaces, and two applications of non-classical spin-multiplexing metalens are experimentally explored, respectively.

In polarization-independent working regime, a near infrared (NIR) metalens with a high NA of 0.91 is experimentally demonstrated to tightly focus a 1550nm laser beam and levitate nanoparticles in a vacuum, because the optical levitated rotating particle has an ultrahigh quality factor which indicates a super higher sensitivity and dynamic range. Based on customized nanorod, the SAM carried by the circular polarized laser beam can be transferred to the levitated nanorod and led to a fast rotation at a speed of Mega-Hertz. It is experimentally illustrated that both the translational and rotational motions of the nanorod can be controlled by the laser beam's polarization and power, the rotational motion can be tuned by the vacuum pressure as well.

As the interaction between two optically coupled oscillators can provide a higher sensing sensitivity than single oscillator-based sensor, it is meaningful to levitated two particles at a close distance. To construct an on-chip optically coupled dynamics system, a NIR dual foci metalens is achieved in the classical spin-multiplexing working regime. Experiment results illustrate that the metalens can provide two precisely controlled optical potential wells. It is experimentally demonstrated that two nanoparticles can be stably levitated at a close distance. Theoretical

calculation figures out that multiple coupling modes can be achieved via the metalens-based optical traps system.

In classical spin-multiplexing working regime, two NIR metalens samples with polarization-controlled focal field are obtained as well. The first one sample has a high NA of 0.89, and the second sample has a NA of 0.25. Based on the high-NA sample, a dual-mode microscope is experimentally demonstrated to achieve a large magnification of 58X and a high resolution of (0.7λ) . The imaging mode of the microscope can be tuned to spiral phase contrast mode with an edge-enhancement effect from bright field mode via polarization control. Then, the high-NA sample is replaced by a 0.25-NA sample in the microscope system, which results in a low magnification of 7.8X but a large FOV of $600\mu\text{m} \times 800\mu\text{m}$. The dual-mode imaging ability and edge-enhancement effect is experimentally verified via USAF 1951 resolution target and an unstained onion epidermal sample. At last, a singlet microscope with a magnification of 4.8X is built via the 0.25-NA metalens sample to show the all-optics edge detection ability. These results could open new opportunities in applications of biological imaging, industrial machine vision, and semiconductor inspection.

In the classical spin-multiplexing regime, a general design frame of single-layer dielectric metasurface is proposed to generate arbitrary non-focused/focused vector vortex beams on a HOPS/HyOPS. Based on linear polarization basis, the simultaneous modulation of local polarization direction and phase is obtained for the first time to analyze the controlled generation of the CVVBs on the HOPS/HyOPS' equator. In proof-of-concept experiments working in the wavelength of 1550nm, 4 metasurface samples experimentally obtained to generate arbitrary beams on the 5th order HOPS (non-focused and tightly-focused), 0-2 order HyOPS, and 0-1 order HyOPS. The tightly-focusing difference between 0-2 order and 0-1 order HyOPS beams are figured out in experiment.

Benefiting from the low requirement on phase difference and more working channels of the non-classical spin-multiplexing metasurface, two tri-channel metalens samples based on low-refraction-index material (i.e., Si_3N_4) are obtained for the world first. To design the tri-channel metalens working in non-classical spin-multiplexing, the linear superposition property of hyperbolic phase profiles is derived.

Based on the modulation mechanism of non-classical spin-multiplexing regime and the linear superposition property of hyperbolic phase profiles, a longitudinal tri-foci Si_3N_4 metalens is obtained in the visible spectrum. In experiment, a commercial Nikon microscope could realize three magnifications without changing objective lens by introducing the longitudinal tri-foci Si_3N_4 metalens. The broadband imaging performance of the metalens sample is investigated, and the chromatic aberration's influence on imaging effect is analyzed. At last, by using the metalens

sample as an objective lens, an infinity-corrected microscope with three high magnifications of 9.5X, 20X, and 29X is integrated to a centimeter-scale device. The integrated microscope can achieve diffraction-limited resolution and large FOV at each magnification.

In addition, a lateral tri-foci Si_3N_4 metalens is obtained in the wavelength of 520nm as well. Two off-axis focal points are corresponding to the LCP and RCP beams, which can be used for chiral imaging. The on-axis focal point is polarization-independent, which can be used for achiral imaging. Therefore, a singlet microscope with a large magnification of 53X and a diffraction-limited resolution (NA = 0.1) of $3\mu\text{m}$ is built up to realize simultaneously achiral and chiral imaging. Based on a customized liquid crystal sample, fast identification of chemical and biological sample's chirality is experimentally demonstrated in an all-optics configuration and a light speed.

In the 9th chapter, a hybrid calculation method is proposed to calculate the optical forces and torques exerted on non-spherical particles levitated by a complexing optical field. Then, a prototype of metalens-based LOMS sensor is invented of the world first. In the invention, a design method is proposed to generate arbitrary optical field via a single-layer metasurface, which could effectively expand the manipulation degree of freedom of the levitated particles.

10.2 Outlook

While the metasurface has demonstrated powerful manipulation capabilities on optical field and some world-leading breakthrough applications have been experimentally achieved in this thesis, there are still a lot of points need to be explored in future.

10.2.1 Working efficiency vs high NA and broadband achromatic

The working efficiency of a metasurface is determined by three factors: transmission of the meta-atoms, the coupling efficiency [Eq. (2.8)], and the focusing efficiency. Both the transmission and coupling efficiency can be usually optimized to be higher than 90% and close to 100% for a single wavelength (i.e., monochromatic application). It indicates that the overall efficiency is general limited by the focusing efficiency. While a larger NA is desirable for optical manipulation and imaging applications, the focusing efficiency would inevitably go down with increasing the NA value, because the refraction angle of the light ray at the metalens edge increases with the NA, which requires a higher phase gradient in at the edge. To realize a higher phase gradient, the phase sampling points in a 2π period should be reduced, and the phase error due to the non-perfect periodical distribution and adjacent coupling will go up. Both the reduced sampling points

and increased phase error can result in a lower diffraction efficiency at the edge as well as a reduced focusing efficiency of the whole metalens.

It is believed that a higher refraction index and a higher aspect ratio of the meta-atoms benefit to achieve high NA metalens with high working efficiency. Therefore, the fabrication capability of nanostructures with high aspect ratio should be improved. In design phase, inverse design methods which significant extends the design space can be adopted and optimized, which will be discussed in next section.

In addition to the high NA, the achromatic metalens is in urgent demand for practical applications. While the chromatic aberration of a metalens can be eliminated for several discrete wavelength via spatial multiplexing method, the working efficiency of the metalens is general low because of the reduced sampling point. Meanwhile, it is theoretically figured out that broadband achromatic metalens is available by engineering the local dispersion relation. However, there are some challenges to be overcome. Firstly, the low transmission problem of multi-resonances based broadband achromatic metalens should be explored in physics and overcome in experiment; Secondly, while non-resonance based metalens (i.e., the one researched in this thesis) can achieve larger chromatic bandwidth, a broadband chromatic metalens requires a high aspect ratio and high refractive index contrast. The requirement on high aspect ratio means the fabrication capability should be improved, and the requirement on high refraction index contrast means more materials platform with high refraction index and negligible absorption should be explored.

There are three alternative ways could be explored as well. The first one is correcting the chromatic aberration via cascading a multiple metalenses or hybrid a metalens and a conventional lens. However, this method increases the complexity of a whole system and reduces the working efficiency. The second way is using an inverse design method to optimize the metalens structural parameters. However, the computer resource of inverse designing a broadband achromatic and large diameter metalens would be a huge challenge. The third way is to reconstruct the object from a chromatic image by using artificial intelligence algorithm, which has been seen as a most effective way of achieving broadband achromatic imaging via a metalens.

10.2.2 Inverse design of metasurface

From last section, we can see the inversely design method can be adopted to achieve high NA metalens with high focusing efficiency as well as to achieve broadband achromatic metalens with high efficiency. However, the current inversely design algorithms are time consuming and requires a huge computer memory. Therefore, innovative inverse design algorithms deserve to be studied to reduce the design time and required computer memory.

10.2.3 Large aperture metasurface

It is challenging to achieve large aperture metalens in both simulation and fabrication. As mentioned above, the phase error arising from the non-perfect periodical distribution and the adjacent coupling effect would be sever at the edge of a metasurface. Therefore, it is necessary to do a whole device simulation and optimization. However, simulation time and required computer memory scales approximately as $O(R^{2.4})$ for commonly adopted FDTD and FEM methods. As a result, the numerically simulated metasurface generally has a micrometre-level diameter, which is usually smaller than the experimental samples. However, in a lot of applications, the metasurface's performance highly depends on the diameter, like, the broadband achromatic metalens. In addition, the whole device simulation is a key role in global inverse design process. Therefore, the high-efficiency and low-memory simulation algorithm should be developed to optimize large-diameter metasurfaces in millimetre and centimetre scale.

The file size of the design layout is the main challenge in fabricating large aperture metasurface. In general, the layout file needs be transformed to an acceptable format (e.g., the V30 file) for the patterning tools (e.g., EBL tool) via a software (e.g., the Genlsys beamer). However, in my experience, the layout file is almost 10Gb for a 4mm metalens with 100 million meta-atoms, and the file size goes up exponentially with the metasurface's radius square. Therefore, it is in an urgent demand for minimizing the layout file. It should be figured out that the new realized Genlsys beam software embedded with python programming ability provides us with an alternative way of fabricating metasurface in centimetre scale. That is we can transfer our design to the EBL tool via python programming code to avoid the restrictions on layout file's size.

10.2.4 Mass production for commercialization

In past few years, the metasurface is mainly researched in lab and fabricated via EBL or FIB process. In recently two years, the metasurface attracts many attentions from consumer electronics field. However, the mass production ability of the metasurface heavily limits the commercialization of metasurface devices, because the typical EBL and FIB process is time-consuming and high costs to define high-resolution patterns in a large area. Up to now, the stepper lithography and nanoimprinting lithography are demonstrated to realize mass production. However, the patterning resolution of stepper lithography is limited to be above 100nm because the demonstrated stepper lithography works in the wavelength of 248nm, which would limit the metasurface's design space. In contrast, the nanoimprinting lithography can transfer the designed pattern to resist via direct contacting, which is a low-cost, high-resolution, and high-throughput patterning way. However, the nanoimprint lithography is not a mature

fabrication process and suffers from some problems, like the contact defects and the template wear. Therefore, the relationship between these lithography errors and metasurface performance should be thoroughly studied. In addition, evaluation standards of massively producing metasurface samples need to build up for guiding the industrial production.

10.2.5 Monolithic integration for structured illumination and manipulation

The monolithic integration of metasurface and light sources (e.g., vertical-external-cavity surface-emitting Laser, VCSEL; light-emitting diode, LED) is a promising trend because the structured illumination for super-resolution imaging and structured optical manipulation via on-chip device are in demand. In fact, two integration methods are attempted in my research.

The first one is passive integration where the light source chip and metasurface sample are separately fabricated and then manually bonded together by PMMA resist. Because the high requirement on the uniformity of the PMMA resist and the alignment of metasurface and the light source chip emission surface, a precisely bonding process and system should be developed. While the flip chip bonding is a mature process in semiconductor field, the light source chip and metasurface's bonding is still challenging because the front surface of the metasurface is too fragile to be damaged.

The second method is active integration where the metasurface is directly fabricated on the light source chip. Therefore, the process compatibility must be carefully considered. For example, the fabrication flow adopted in this thesis can not work for the active integration process, because the Cr etchant is strong acid and will damage the electrodes of the light source chip. Therefore, new fabrication flow should be developed to realize active integration.

Appendix A Dielectric material selection

As discussed above, a high refraction index and a low absorption index of the material would be beneficial to increase the metasurface design space for achieving high efficiency, high NA, and broadband achromatic. Therefore, the Si_3N_4 , GaN, and TiO_2 are widely used in visible spectrum, Si is commonly adopted for NIR and short wavelength mid-infrared applications, and Ge/Te can be used for long wavelength mid-infrared spectrum. To avoid severe absorption in UV spectrum, the dielectric material with a wide bandgap value ($E_g > 3.3\text{eV}$) is preferred. Therefore, the SiO_2 ($E_g \approx 9\text{eV}$), HfO_2 ($E_g \approx 5.7\text{eV}$), AlN ($E_g \approx 6\text{eV}$), Si_3N_4 ($E_g \approx 5\text{eV}$), Nb_2O_5 ($E_g \approx 3.65\text{eV}$) and GaN ($E_g \approx 3.4\text{eV}$) can be used for UV metasurface in theory. However, limited by the low refraction index (~ 1.48), the SiO_2 is usually used as substrate in UV, visible, and NIR spectrums. While the Nb_2O_5 ($E_g \approx 3.65\text{eV}$) and GaN ($E_g \approx 3.4\text{eV}$) metasurface can only high-efficiently work in near UV spectrum, the HfO_2 ($E_g \approx 5.7\text{eV}$), AlN ($E_g \approx 6\text{eV}$), and Si_3N_4 ($E_g \approx 5\text{eV}$) metasurface can work in deep UV spectrum with high efficiency. Recently, a new material platform Ta_2O_5 with a $E_g \approx 4\text{eV}$ is explored for high-performance metasurface in UV and visible spectrums.

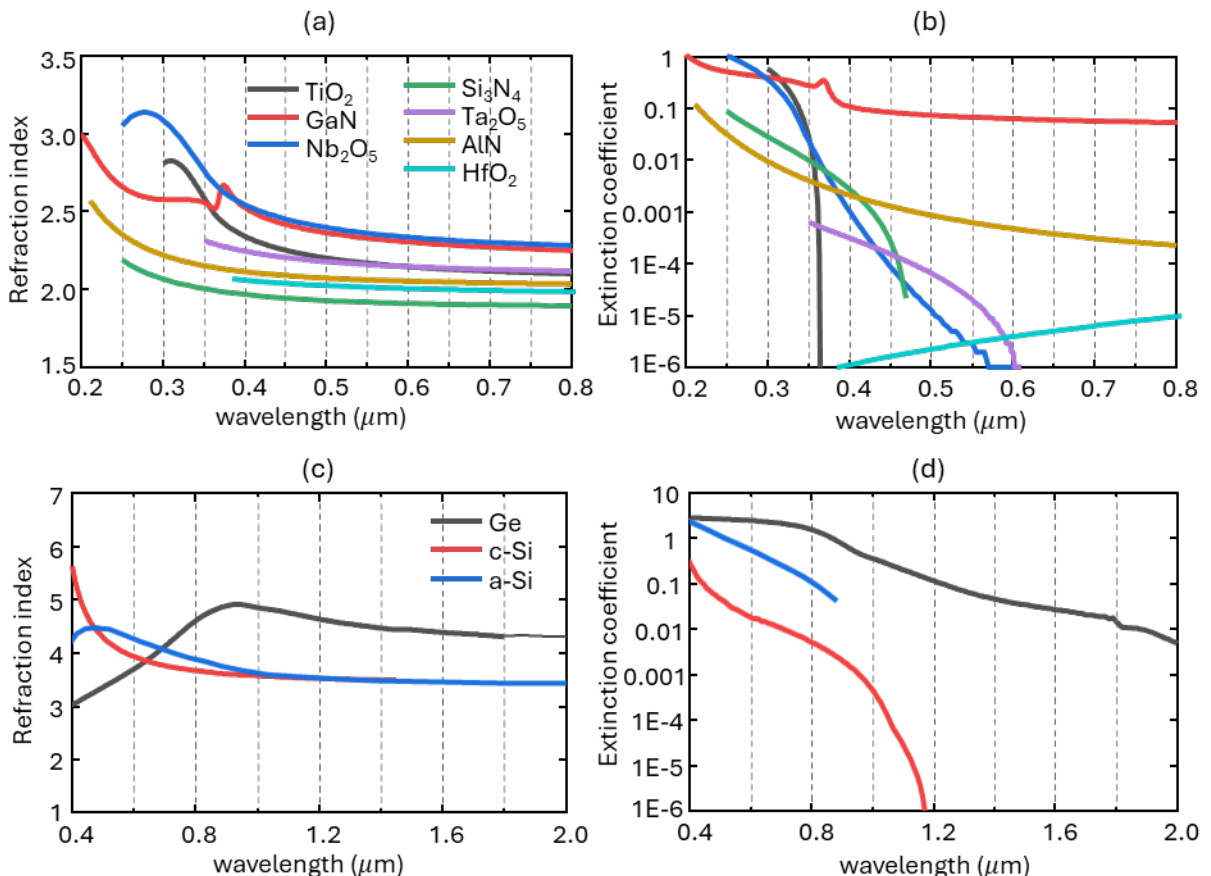


Figure A1. Refraction (a, c) and extinction (b, d) index of widely used dielectric materials.

(a) and (b) share a same legend, and (c) and (d) share a same one.

Appendix A

As shown in Figures A1(a) and A1(b), the Nb_2O_5 has a higher refraction index and lower absorption than TiO_2 and GaN in a wide spectrum ranging from 300nm to 800nm, which indicates the Nb_2O_5 is more suitable for near-UV and visible metasurfaces. However, it is challenging to achieve high-aspect-ratio Nb_2O_5 meta-atoms with small feature size and smooth side wall, which limits the development of Nb_2O_5 metasurfaces in visible spectrum. Benefiting from the wide bandgap and high refraction index, the Nb_2O_5 metasurface for near-UV applications attracts increasing interests in recent years. Meanwhile, the AlN's utilization is also restricted by the etching process.

From Figure A1(a), comparing with the other materials, the Si_3N_4 has a lowest refraction index from 250nm to 800nm, which heavily limits its applications in multifunctional metasurface, while the fabrication of Si_3N_4 devices is much easier and cheaper than fabricating than GaN and TiO_2 devices following a conventional CMOS process. To overcome the refraction index's restriction, this thesis developed a non-classical spin-multiplexing design regime, and experimentally demonstrated two tri-channel Si_3N_4 metalens samples for integrated microscope as well as simultaneously achiral and chiral microscope.

The Ta_2O_5 material can be used for high performance UV and visible metasurface because its refraction index is high enough, it is transparent from 350nm to 800nm, and its fabrication is totally CMOS-compatible.

Figures A1(c) and A1(d) respectively demonstrate the refraction index and extinction coefficient of Ge, a-Si, and c-Si in visible and NIR spectrums ranging from 400nm to 2000nm. It could be seen that the Ge will suffer from higher absorption than Si in visible and NIR region, while it has a higher refraction index. In addition, the cost of Ge material is much higher than Si. Therefore, researchers are trying to achieve high performance Si metasurface working in mid-infrared. In addition, we can see that the a-Si has a much larger extinction coefficient and a slightly larger refraction index than the c-Si in visible spectrum ranging from 400nm to 800nm. Therefore, c-Si is more widely adopted for visible metasurfaces than a-Si.

Appendix B Fabrication details and notes.

B.1 Temperature's influence on PECVD a-Si

The meta-atoms in a-Si metalens have a height of 800nm. An 800nm-thick a-Si film needs to be deposited on the cleaned SiO_2 wafer. Initially, the film is deposited at 200°C via the PECVD (DP02), but it peels off from the substrate in 24 hours. To improve the adhesive force between the a-Si and SiO_2 substrate, the deposition temperature is increased to 250°C, and the deposition rate is measured to be 16nm/s.

B.2 Optical property of PECVD Si_3N_4

To achieve 800nm-thick Si_3N_4 film on a SiO_2 substrate, the SiH_4 (12.5sccm), NH_3 (20sccm) and N_2 (500sccm) gases are used in our PECVD tool (DP01). The deposition temperature, RF power, and pressure are 350°C, 20W, and 750mTorr, respectively. A deposition rate of 25nm/min is achieved in experiment. The optical properties of the PECVD Si_3N_4 film are shown in Figure 7.7(b) which indicates the absorption does not equal to zero anymore for the wavelength shorter than 441nm.

B.3 RIE parameters for Si_3N_4

To try to obtain good side wall of the Si_3N_4 meta-atoms using RIE tool (EP02), the etching parameters are optimized to be 75W in RF power and 55mTorr in pressure. The flows of etching gas CHF_3 and O_2 are 18sccm and 2sccm, respectively. The fabricated Si_3N_4 meta-atoms are shown below.

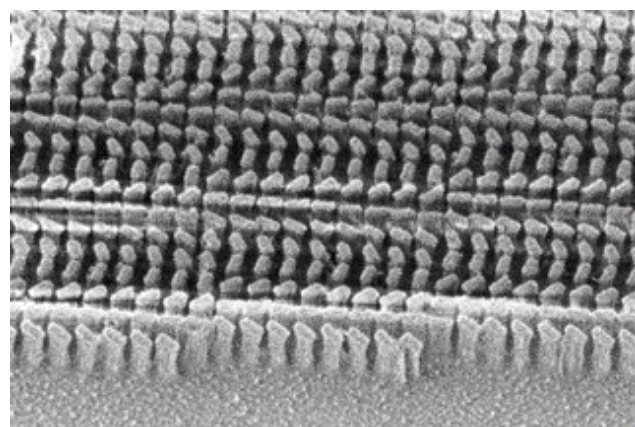


Figure A2. SEM image of Si_3N_4 meta-atoms.

B.4 E-spacer's influence on EBL

As shown in Figures. A3(a), there is always a bubble on the metalens region when a large-aperture metalens is patterned by EBL based on the free e-spacer (i.e., ESPACER 300Z from Showa Denko company), and the EBL patterned metalens array has a poor uniformity [Figure. A3(b)]. When a high-quality e-spacer is used as the conductive layer, the large aperture metalens sample can be fabricated without any bubbles [Figure. A3(c)], and a good uniformity can be achieved for the metalens array [Figure. A3(d)].

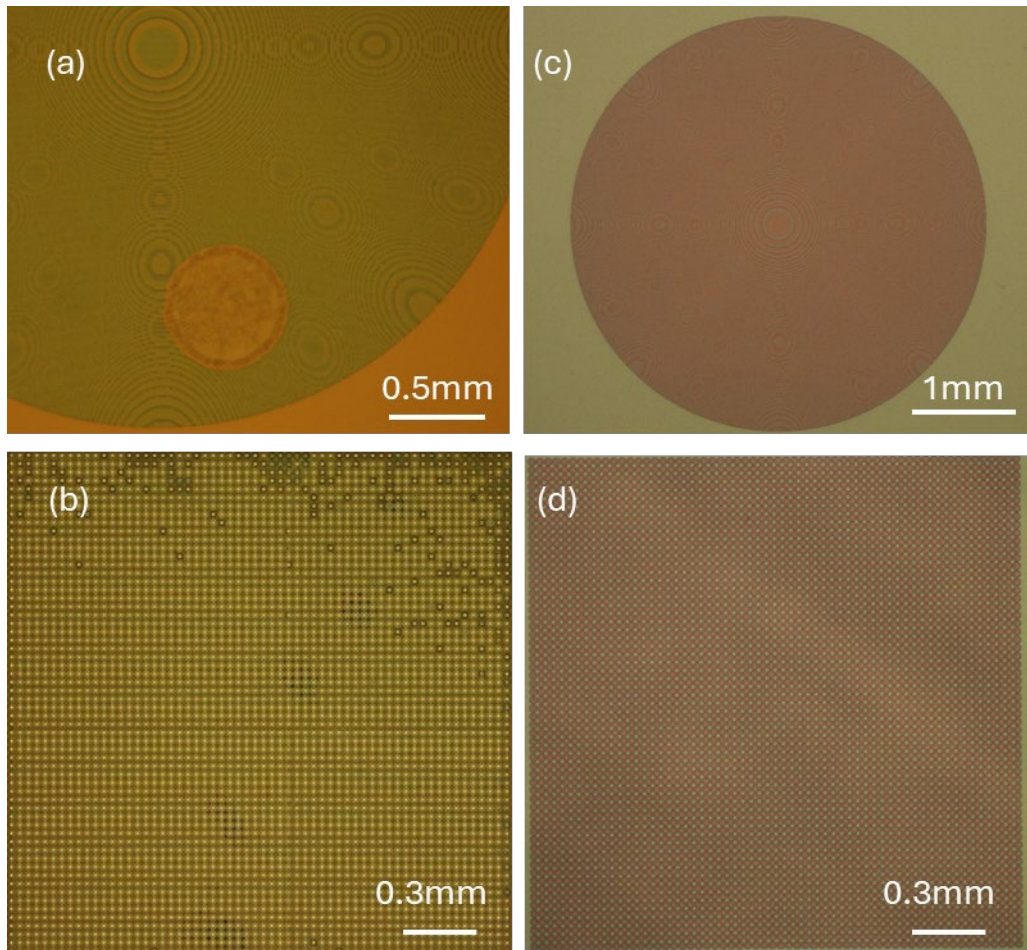


Figure A3. EBL pattern using (a)-(b) free e-spacer, and (c)-(d) charged e-spacer.

Appendix C Working mechanism in linear polarization basis.

The Jones matrix [Eq. (2.5)] of metasurface is adopted as the starter [Eq. (A.1)] to derive the working mechanism of a classical spin-multiplexing metasurface in linear polarization basis.

$$\begin{bmatrix} E_x^o \\ E_y^o \end{bmatrix} = e^{i\phi_x} \begin{bmatrix} \cos(2\theta) & \sin(2\theta) \\ \sin(2\theta) & -\cos(2\theta) \end{bmatrix} \times \begin{bmatrix} E_x \\ E_y \end{bmatrix} \quad (\text{A.1})$$

When the incident light beam is linear polarization (LP) (i.e., $\begin{bmatrix} E_x \\ E_y \end{bmatrix} = \begin{bmatrix} \cos(2\chi) \\ \sin(2\chi) \end{bmatrix}$), the ongoing optical field can be obtained as Eq. (A.2), which is an linearly polarized light beam with a phase profile of ϕ_x and a linearly polarized angle of $2\theta - 2\chi$. It means that, a classical spin-multiplexing meta-atom could simultaneously rotate the local polarization direction (from 2χ to $2\theta - 2\chi$) and impose a phase of ϕ_x for an incident LP beam.

$$\begin{bmatrix} E_x^o \\ E_y^o \end{bmatrix} = e^{\phi_x} \begin{bmatrix} \cos(2\theta - 2\chi) \\ \sin(2\theta - 2\chi) \end{bmatrix} \quad (\text{A.2})$$

Based on Eq. (A.2), a simple explanation of the orders and topological charges of the CVBs represented by HOPS/HyOPS' equator could be given as below. Based on the Eq. (6.6) and Eq. (6.7), the designed metasurface for generating arbitrary VVBs over a HOPS/HyOPS has a propagation phase profile of Eq. (A.3), and the meta-atoms array of the metasurface has a rotation distribution of Eq. (A.4).

$$\phi_x(\rho, \varphi) = \Phi(\rho) + \left(\frac{N+M}{2}\right)\varphi \quad (\text{A.3})$$

$$\theta(\rho, \varphi) = \left(\frac{N-M}{4}\right)\varphi \quad (\text{A.4})$$

Substituting Eq. (A.3) and Eq. (A.4) into the Eq. (A.2), the ongoing optical field from the metasurface can be obtained as Eq. (A.5), which denotes a serial of CVVBs with a vector order of $(N - M)/2$ and a topological charge of $(M + N)/2$ and can be tuned via the polarization angle 2χ .

$$\begin{bmatrix} E_x^o \\ E_y^o \end{bmatrix} = e^{[\Phi(\rho) + \left(\frac{N+M}{2}\right)\varphi]} \begin{bmatrix} \cos \left[\left(\frac{N-M}{2}\right)\varphi - 2\chi\right] \\ \sin \left[\left(\frac{N-M}{2}\right)\varphi - 2\chi\right] \end{bmatrix} \quad (\text{A.5})$$

Appendix C

Glossary of Terms

List of References

- [1] N. Yu *et al.*, ‘Light Propagation with Phase Discontinuities: Generalized Laws of Reflection and Refraction’, *Science* (1979), vol. 334, no. 6054, pp. 333–337, Oct. 2011, doi: 10.1126/science.1210713.
- [2] J. Zhang, X. Wei, I. D. Rukhlenko, H.-T. Chen, and W. Zhu, ‘Electrically Tunable Metasurface with Independent Frequency and Amplitude Modulations’, *ACS Photonics*, vol. 7, no. 1, pp. 265–271, Jan. 2020, doi: 10.1021/acsphotonics.9b01532.
- [3] J. Liao, S. Guo, L. Yuan, C. Ji, C. Huang, and X. Luo, ‘Independent Manipulation of Reflection Amplitude and Phase by a Single-Layer Reconfigurable Metasurface’, *Adv Opt Mater*, vol. 10, no. 4, Feb. 2022, doi: 10.1002/adom.202101551.
- [4] X. Zeng *et al.*, ‘Arbitrary manipulations of focused higher-order Poincaré beams by a Fresnel zone metasurface with alternate binary geometric and propagation phases’, *Photonics Res*, vol. 10, no. 4, p. 1117, Apr. 2022, doi: 10.1364/PRJ.451637.
- [5] Y. Kim, G. Lee, J. Sung, J. Jang, and B. Lee, ‘Spiral Metalens for Phase Contrast Imaging’, *Adv Funct Mater*, vol. 32, no. 5, Jan. 2022, doi: 10.1002/adfm.202106050.
- [6] Y. Intaravanne and X. Chen, ‘Recent advances in optical metasurfaces for polarization detection and engineered polarization profiles’, *Nanophotonics*, vol. 9, no. 5, pp. 1003–1014, May 2020, doi: 10.1515/nanoph-2019-0479.
- [7] A. H. Dorrah, N. A. Rubin, A. Zaidi, M. Tamagnone, and F. Capasso, ‘Metasurface optics for on-demand polarization transformations along the optical path’, *Nat Photonics*, vol. 15, no. 4, pp. 287–296, Apr. 2021, doi: 10.1038/s41566-020-00750-2.
- [8] J. C. Ke *et al.*, ‘Frequency-modulated continuous waves controlled by space-time-coding metasurface with nonlinearly periodic phases’, *Light Sci Appl*, vol. 11, no. 1, p. 273, Sep. 2022, doi: 10.1038/s41377-022-00973-8.
- [9] M. K. Chen *et al.*, ‘Principles, Functions, and Applications of Optical Meta-Lens’, *Adv Opt Mater*, vol. 9, no. 4, Feb. 2021, doi: 10.1002/adom.202001414.
- [10] T. Chung, H. Wang, and H. Cai, ‘Dielectric metasurfaces for next-generation optical biosensing: a comparison with plasmonic sensing’, *Nanotechnology*, vol. 34, no. 40, p. 402001, Oct. 2023, doi: 10.1088/1361-6528/ace117.

List of References

- [11] D. Jeon, K. Shin, S.-W. Moon, and J. Rho, ‘Recent advancements of metalenses for functional imaging’, *Nano Converg*, vol. 10, no. 1, p. 24, May 2023, doi: 10.1186/s40580-023-00372-8.
- [12] A. Arbabi and A. Faraon, ‘Advances in optical metalenses’, *Nat Photonics*, vol. 17, no. 1, pp. 16–25, Jan. 2023, doi: 10.1038/s41566-022-01108-6.
- [13] M. Pan *et al.*, ‘Dielectric metalens for miniaturized imaging systems: progress and challenges’, *Light Sci Appl*, vol. 11, no. 1, p. 195, Jun. 2022, doi: 10.1038/s41377-022-00885-7.
- [14] G. R. Kumar, ‘The 2018 Nobel Prize in Physics: A Gripping and Extremely Exciting Tale of Light’, *Curr Sci*, vol. 115, no. 10, p. 1844, 2018.
- [15] A. Ashkin and J. M. Dziedzic, ‘Optical Trapping and Manipulation of Viruses and Bacteria’, *Science (1979)*, vol. 235, no. 4795, pp. 1517–1520, Mar. 1987, doi: 10.1126/science.3547653.
- [16] M. J. Lang, P. M. Fordyce, A. M. Engh, K. C. Neuman, and S. M. Block, ‘Simultaneous, coincident optical trapping and single-molecule fluorescence’, *Nat Methods*, vol. 1, no. 2, pp. 133–139, Nov. 2004, doi: 10.1038/nmeth714.
- [17] J. Millen, T. S. Monteiro, R. Pettit, and A. N. Vamivakas, ‘Optomechanics with levitated particles’, *Reports on Progress in Physics*, vol. 83, no. 2, p. 026401, Feb. 2020, doi: 10.1088/1361-6633/ab6100.
- [18] U. Delić *et al.*, ‘Cooling of a levitated nanoparticle to the motional quantum ground state’, *Science (1979)*, vol. 367, no. 6480, pp. 892–895, Feb. 2020, doi: 10.1126/science.aba3993.
- [19] J. A. Vovrosh, ‘Parametric feedback cooling and squeezing of optically levitated particles’, University of Southampton, 2018.
- [20] E. Otte and C. Denz, ‘Optical trapping gets structure: Structured light for advanced optical manipulation’, *Appl Phys Rev*, vol. 7, no. 4, Dec. 2020, doi: 10.1063/5.0013276.
- [21] Y. Shi *et al.*, ‘Optical manipulation with metamaterial structures’, *Appl Phys Rev*, vol. 9, no. 3, Sep. 2022, doi: 10.1063/5.0091280.
- [22] C. He, Y. Shen, and A. Forbes, ‘Towards higher-dimensional structured light’, *Light Sci Appl*, vol. 11, no. 1, p. 205, Jul. 2022, doi: 10.1038/s41377-022-00897-3.

List of References

- [23] K. Shen *et al.*, ‘On-chip optical levitation with a metalens in vacuum’, *Optica*, vol. 8, no. 11, p. 1359, Nov. 2021, doi: 10.1364/OPTICA.438410.
- [24] R. Reimann *et al.*, ‘GHz Rotation of an Optically Trapped Nanoparticle in Vacuum’, *Phys Rev Lett*, vol. 121, no. 3, p. 033602, Jul. 2018, doi: 10.1103/PhysRevLett.121.033602.
- [25] Y. Jin, J. Yan, S. J. Rahman, J. Li, X. Yu, and J. Zhang, ‘6 GHz hyperfast rotation of an optically levitated nanoparticle in vacuum’, *Photonics Res*, vol. 9, no. 7, p. 1344, Jul. 2021, doi: 10.1364/PRJ.422975.
- [26] R. C. Devlin, A. Ambrosio, N. A. Rubin, J. P. B. Mueller, and F. Capasso, ‘Arbitrary spin-to-orbital angular momentum conversion of light’, *Science* (1979), vol. 358, no. 6365, pp. 896–901, Nov. 2017, doi: 10.1126/science.aoa5392.
- [27] Y. Arita, E. M. Wright, and K. Dholakia, ‘Optical binding of two cooled micro-gyroscopes levitated in vacuum’, *Optica*, vol. 5, no. 8, p. 910, Aug. 2018, doi: 10.1364/OPTICA.5.000910.
- [28] J. Rieser *et al.*, ‘Tunable light-induced dipole-dipole interaction between optically levitated nanoparticles’, *Science* (1979), vol. 377, no. 6609, pp. 987–990, Aug. 2022, doi: 10.1126/science.abp9941.
- [29] F. Ricci *et al.*, ‘Optically levitated nanoparticle as a model system for stochastic bistable dynamics’, *Nat Commun*, vol. 8, no. 1, p. 15141, May 2017, doi: 10.1038/ncomms15141.
- [30] A. Militaru, M. Innerbichler, M. Frimmer, F. Tebbenjohanns, L. Novotny, and C. Dellago, ‘Escape dynamics of active particles in multistable potentials’, *Nat Commun*, vol. 12, no. 1, p. 2446, Apr. 2021, doi: 10.1038/s41467-021-22647-6.
- [31] P. Thiruvenkatanathan, J. Yan, J. Woodhouse, A. Aziz, and A. A. Seshia, ‘Ultrasensitive mode-localized mass sensor with electrically tunable parametric sensitivity’, *Appl Phys Lett*, vol. 96, no. 8, Feb. 2010, doi: 10.1063/1.3315877.
- [32] C. Gonzalez-Ballester, M. Aspelmeyer, L. Novotny, R. Quidant, and O. Romero-Isart, ‘Levitodynamics: Levitation and control of microscopic objects in vacuum’, *Science* (1979), vol. 374, no. 6564, Oct. 2021, doi: 10.1126/science.abg3027.
- [33] H. Rudolph, U. Delić, M. Aspelmeyer, K. Hornberger, and B. A. Stickler, ‘Force-Gradient Sensing and Entanglement via Feedback Cooling of Interacting Nanoparticles’, *Phys Rev Lett*, vol. 129, no. 19, p. 193602, Nov. 2022, doi: 10.1103/PhysRevLett.129.193602.

List of References

- [34] T. M. Grzegorczyk, B. A. Kemp, and J. A. Kong, ‘Stable Optical Trapping Based on Optical Binding Forces’, *Phys Rev Lett*, vol. 96, no. 11, p. 113903, Mar. 2006, doi: 10.1103/PhysRevLett.96.113903.
- [35] V. Karásek, T. Čižmár, O. Brzobohatý, P. Zemánek, V. Garcés-Chávez, and K. Dholakia, ‘Long-Range One-Dimensional Longitudinal Optical Binding’, *Phys Rev Lett*, vol. 101, no. 14, p. 143601, Oct. 2008, doi: 10.1103/PhysRevLett.101.143601.
- [36] Y. Arita, M. Mazilu, T. Vettenburg, E. M. Wright, and K. Dholakia, ‘Rotation of two trapped microparticles in vacuum: observation of optically mediated parametric resonances’, *Opt Lett*, vol. 40, no. 20, p. 4751, Oct. 2015, doi: 10.1364/OL.40.004751.
- [37] G. Volpe *et al.*, ‘Roadmap for Optical Tweezers’, Jun. 2022.
- [38] K. Y. Bliokh, F. J. Rodríguez-Fortuño, F. Nori, and A. V. Zayats, ‘Spin–orbit interactions of light’, *Nat Photonics*, vol. 9, no. 12, pp. 796–808, Dec. 2015, doi: 10.1038/nphoton.2015.201.
- [39] Z. Shen, Z. Xiang, Z. Wang, Y. Shen, and B. Zhang, ‘Optical spanner for nanoparticle rotation with focused optical vortex generated through a Pancharatnam–Berry phase metasurface’, *Appl Opt*, vol. 60, no. 16, p. 4820, Jun. 2021, doi: 10.1364/AO.425892.
- [40] G. Milione, H. I. Sztul, D. A. Nolan, and R. R. Alfano, ‘Higher-Order Poincaré Sphere, Stokes Parameters, and the Angular Momentum of Light’, *Phys Rev Lett*, vol. 107, no. 5, p. 053601, Jul. 2011, doi: 10.1103/PhysRevLett.107.053601.
- [41] X. Yi *et al.*, ‘Hybrid-order Poincaré sphere’, *Phys Rev A (Coll Park)*, vol. 91, no. 2, p. 023801, Feb. 2015, doi: 10.1103/PhysRevA.91.023801.
- [42] Y. Bao, J. Ni, and C. Qiu, ‘A Minimalist Single-Layer Metasurface for Arbitrary and Full Control of Vector Vortex Beams’, *Advanced Materials*, vol. 32, no. 6, Feb. 2020, doi: 10.1002/adma.201905659.
- [43] S. Wang, S. Wen, Z.-L. Deng, X. Li, and Y. Yang, ‘Metasurface-Based Solid Poincaré Sphere Polarizer’, *Phys Rev Lett*, vol. 130, no. 12, p. 123801, Mar. 2023, doi: 10.1103/PhysRevLett.130.123801.
- [44] H. Sroor *et al.*, ‘Generation of arbitrary higher order Poincaré beams from a visible metasurface laser’, in *Laser Resonators, Microresonators, and Beam Control XXII*, A. M. Armani, A. V. Kudryashov, A. H. Paxton, and V. S. Ilchenko, Eds., SPIE, Mar. 2020, p. 19. doi: 10.1117/12.2546267.

List of References

[45] J. Ji *et al.*, ‘Metasurface-Enabled On-Chip Manipulation of Higher-Order Poincaré Sphere Beams’, *Nano Lett*, vol. 23, no. 7, pp. 2750–2757, Apr. 2023, doi: 10.1021/acs.nanolett.3c00021.

[46] S. Wang *et al.*, ‘Arbitrary polarization conversion dichroism metasurfaces for all-in-one full Poincaré sphere polarizers’, *Light Sci Appl*, vol. 10, no. 1, p. 24, Jan. 2021, doi: 10.1038/s41377-021-00468-y.

[47] J. Yang, T. K. Hakala, and A. T. Friberg, ‘Generation of arbitrary vector Bessel beams on higher-order Poincaré spheres with an all-dielectric metasurface’, *Phys Rev A (Coll Park)*, vol. 106, no. 2, p. 023520, Aug. 2022, doi: 10.1103/PhysRevA.106.023520.

[48] I. Nape *et al.*, ‘Revealing the invariance of vectorial structured light in complex media’, *Nat Photonics*, vol. 16, no. 7, pp. 538–546, Jul. 2022, doi: 10.1038/s41566-022-01023-w.

[49] M. Liu *et al.*, ‘Super-resolution optical microscopy using cylindrical vector beams’, *Nanophotonics*, vol. 11, no. 15, pp. 3395–3420, Aug. 2022, doi: 10.1515/nanoph-2022-0241.

[50] G. Kontenis, D. Gailevičius, N. Jiménez, and K. Staliunas, ‘Optical Drills by Dynamic High-Order Bessel Beam Mixing’, *Phys Rev Appl*, vol. 17, no. 3, p. 034059, Mar. 2022, doi: 10.1103/PhysRevApplied.17.034059.

[51] Q. Zhan, ‘Cylindrical vector beams: from mathematical concepts to applications’, *Adv Opt Photonics*, vol. 1, no. 1, p. 1, Jan. 2009, doi: 10.1364/AOP.1.000001.

[52] T. Li, C. Chen, X. Xiao, J. Chen, S. Hu, and S. Zhu, ‘Revolutionary meta-imaging: from superlens to metalens’, *Photonics Insights*, vol. 2, no. 1, p. R01, 2023, doi: 10.3788/PI.2023.R01.

[53] X. Zou *et al.*, ‘Imaging based on metalenses’, *PhotoniX*, vol. 1, no. 1, p. 2, Dec. 2020, doi: 10.1186/s43074-020-00007-9.

[54] T. Badloe *et al.*, ‘Bright-Field and Edge-Enhanced Imaging Using an Electrically Tunable Dual-Mode Metalens’, *ACS Nano*, vol. 17, no. 15, pp. 14678–14685, Aug. 2023, doi: 10.1021/acs.nanolett.3c02471.

[55] S. Wang *et al.*, ‘Metalens for Accelerated Optoelectronic Edge Detection under Ambient Illumination’, *Nano Lett*, vol. 24, no. 1, pp. 356–361, Jan. 2024, doi: 10.1021/acs.nanolett.3c04112.

List of References

- [56] J. C. Zhang *et al.*, ‘Nanoimprint Meta-Device for Chiral Imaging’, *Adv Funct Mater*, vol. 33, no. 49, Dec. 2023, doi: 10.1002/adfm.202306422.
- [57] M. Khorasaninejad *et al.*, ‘Multispectral Chiral Imaging with a Metalens’, *Nano Lett*, vol. 16, no. 7, pp. 4595–4600, Jul. 2016, doi: 10.1021/acs.nanolett.6b01897.
- [58] S. Fürhapter, A. Jesacher, S. Bernet, and M. Ritsch-Marte, ‘Spiral phase contrast imaging in microscopy’, *Opt Express*, vol. 13, no. 3, p. 689, Feb. 2005, doi: 10.1364/OPEX.13.000689.
- [59] C. Chen *et al.*, ‘Parallel Polarization Illumination with a Multifocal Axicon Metalens for Improved Polarization Imaging’, *Nano Lett*, vol. 20, no. 7, pp. 5428–5434, Jul. 2020, doi: 10.1021/acs.nanolett.0c01877.
- [60] Z. Shen, F. Zhao, C. Jin, S. Wang, L. Cao, and Y. Yang, ‘Monocular metasurface camera for passive single-shot 4D imaging’, *Nat Commun*, vol. 14, no. 1, p. 1035, Feb. 2023, doi: 10.1038/s41467-023-36812-6.
- [61] C. Zou, J. Sautter, F. Setzpfandt, and I. Staude, ‘Resonant dielectric metasurfaces: active tuning and nonlinear effects’, *J Phys D Appl Phys*, vol. 52, no. 37, p. 373002, Sep. 2019, doi: 10.1088/1361-6463/ab25ff.
- [62] M. Kang, T. Liu, C. T. Chan, and M. Xiao, ‘Applications of bound states in the continuum in photonics’, *Nature Reviews Physics*, vol. 5, no. 11, pp. 659–678, Oct. 2023, doi: 10.1038/s42254-023-00642-8.
- [63] H. S. Khaliq, A. Nauman, J. Lee, and H. Kim, ‘Recent Progress on Plasmonic and Dielectric Chiral Metasurfaces: Fundamentals, Design Strategies, and Implementation’, *Adv Opt Mater*, vol. 11, no. 16, Aug. 2023, doi: 10.1002/adom.202300644.
- [64] M. Khorasaninejad *et al.*, ‘Visible Wavelength Planar Metalenses Based on Titanium Dioxide’, *IEEE Journal of Selected Topics in Quantum Electronics*, vol. 23, no. 3, pp. 43–58, May 2017, doi: 10.1109/JSTQE.2016.2616447.
- [65] P. Qiao, W. Yang, and C. J. Chang-Hasnain, ‘Recent advances in high-contrast metastructures, metasurfaces, and photonic crystals’, *Adv Opt Photonics*, vol. 10, no. 1, p. 180, Mar. 2018, doi: 10.1364/AOP.10.000180.
- [66] A. C. Overvig *et al.*, ‘Dielectric metasurfaces for complete and independent control of the optical amplitude and phase’, *Light Sci Appl*, vol. 8, no. 1, p. 92, Oct. 2019, doi: 10.1038/s41377-019-0201-7.

List of References

- [67] W. Liu, Z. Li, H. Cheng, and S. Chen, ‘Dielectric Resonance-Based Optical Metasurfaces: From Fundamentals to Applications’, *iScience*, vol. 23, no. 12, p. 101868, Dec. 2020, doi: 10.1016/j.isci.2020.101868.
- [68] D. Lin, P. Fan, E. Hasman, and M. L. Brongersma, ‘Dielectric gradient metasurface optical elements’, *Science* (1979), vol. 345, no. 6194, pp. 298–302, Jul. 2014, doi: 10.1126/science.1253213.
- [69] P. Huo *et al.*, ‘Photonic Spin-Multiplexing Metasurface for Switchable Spiral Phase Contrast Imaging’, *Nano Lett*, vol. 20, no. 4, pp. 2791–2798, Apr. 2020, doi: 10.1021/acs.nanolett.0c00471.
- [70] B. Yao *et al.*, ‘Spin-decoupled metalens with intensity-tunable multiple focal points’, *Photonics Res*, vol. 9, no. 6, p. 1019, Jun. 2021, doi: 10.1364/PRJ.420665.
- [71] W. T. Chen, A. Y. Zhu, and F. Capasso, ‘Flat optics with dispersion-engineered metasurfaces’, *Nat Rev Mater*, vol. 5, no. 8, pp. 604–620, Jun. 2020, doi: 10.1038/s41578-020-0203-3.
- [72] D. Zhao *et al.*, ‘Recent advances in ultraviolet nanophotonics: from plasmonics and metamaterials to metasurfaces’, *Nanophotonics*, vol. 10, no. 9, pp. 2283–2308, Jul. 2021, doi: 10.1515/nanoph-2021-0083.
- [73] A. A. Geraci, S. B. Papp, and J. Kitching, ‘Short-Range Force Detection Using Optically Cooled Levitated Microspheres’, *Phys Rev Lett*, vol. 105, no. 10, p. 101101, Aug. 2010, doi: 10.1103/PhysRevLett.105.101101.
- [74] H. Ulbricht, ‘Testing Fundamental Physics by Using Levitated Mechanical Systems’, in *Molecular Beams in Physics and Chemistry*, Cham: Springer International Publishing, 2021, pp. 303–332. doi: 10.1007/978-3-030-63963-1_15.
- [75] J. Ahn, Z. Xu, J. Bang, P. Ju, X. Gao, and T. Li, ‘Ultrasensitive torque detection with an optically levitated nanorotor’, *Nat Nanotechnol*, vol. 15, no. 2, pp. 89–93, Feb. 2020, doi: 10.1038/s41565-019-0605-9.
- [76] J. Gieseler, L. Novotny, and R. Quidant, ‘Thermal nonlinearities in a nanomechanical oscillator’, *Nat Phys*, vol. 9, no. 12, pp. 806–810, Dec. 2013, doi: 10.1038/nphys2798.
- [77] J. Gieseler *et al.*, ‘Optical tweezers — from calibration to applications: a tutorial’, *Adv Opt Photonics*, vol. 13, no. 1, p. 74, Mar. 2021, doi: 10.1364/AOP.394888.

List of References

[78] D. C. Moore and A. A. Geraci, ‘Searching for new physics using optically levitated sensors’, *Quantum Sci Technol*, vol. 6, no. 1, p. 014008, Jan. 2021, doi: 10.1088/2058-9565/abcf8a.

[79] Z.-B. Fan *et al.*, ‘Silicon Nitride Metalenses for Close-to-One Numerical Aperture and Wide-Angle Visible Imaging’, *Phys Rev Appl*, vol. 10, no. 1, p. 014005, Jul. 2018, doi: 10.1103/PhysRevApplied.10.014005.

[80] J. Piotrowski *et al.*, ‘Simultaneous ground-state cooling of two mechanical modes of a levitated nanoparticle’, Sep. 2022, doi: 10.1038/s41567-023-01956-1.

[81] J. Yan, X. Yu, Z. V. Han, T. Li, and J. Zhang, ‘On-demand assembly of optically levitated nanoparticle arrays in vacuum’, *Photonics Res*, vol. 11, no. 4, p. 600, Apr. 2023, doi: 10.1364/PRJ.471547.

[82] hamamatsu, ‘LCOS-SLM (optical phase modulator) X15213 series’, <https://www.hamamatsu.com/jp/en/product/lasers/laser-related-products/lcos-slm/for-research-and-development.html>.

[83] J. Vijayan *et al.*, ‘Scalable all-optical cold damping of levitated nanoparticles’, *Nat Nanotechnol*, vol. 18, no. 1, pp. 49–54, Jan. 2023, doi: 10.1038/s41565-022-01254-6.

[84] D. Castelvecchi, “Levitating” nanoparticles could push the limits of quantum entanglement’, *Nature*, Aug. 2022, doi: 10.1038/d41586-022-02322-6.

[85] A. Ashkin and J. M. Dziedzic, ‘Optical Levitation by Radiation Pressure’, *Appl Phys Lett*, vol. 19, no. 8, pp. 283–285, Oct. 1971, doi: 10.1063/1.1653919.

[86] A. Ashkin and J. M. Dziedzic, ‘Optical levitation in high vacuum’, *Appl Phys Lett*, vol. 28, no. 6, pp. 333–335, Mar. 1976, doi: 10.1063/1.88748.

[87] V. N. Mahajan, ‘Strehl ratio for primary aberrations in terms of their aberration variance’, *J Opt Soc Am*, vol. 73, no. 6, p. 860, Jun. 1983, doi: 10.1364/JOSA.73.000860.

[88] Y. Zhou *et al.*, ‘Observation of high-order imaginary Poynting momentum optomechanics in structured light’, *Proceedings of the National Academy of Sciences*, vol. 119, no. 44, Nov. 2022, doi: 10.1073/pnas.2209721119.

[89] M. Nieto-Vesperinas and X. Xu, ‘The complex Maxwell stress tensor theorem: The imaginary stress tensor and the reactive strength of orbital momentum. A novel scenery underlying electromagnetic optical forces’, *Light Sci Appl*, vol. 11, no. 1, p. 297, Oct. 2022, doi: 10.1038/s41377-022-00979-2.

List of References

- [90] Ansys/Optics, ‘Optical force on a particle (3D)’, <https://optics.ansys.com/hc/en-us/articles/360042214434-Optical-force-on-a-particle-3D>.
- [91] F. Monteiro, W. Li, G. Afek, C. Li, M. Mossman, and D. C. Moore, ‘Force and acceleration sensing with optically levitated nanogram masses at microkelvin temperatures’, *Phys Rev A (Coll Park)*, vol. 101, no. 5, p. 053835, May 2020, doi: 10.1103/PhysRevA.101.053835.
- [92] H. Li, Z. Zhang, L. Zu, Y. Hao, and H. Chang, ‘Micromechanical mode-localized electric current sensor’, *Microsyst Nanoeng*, vol. 8, no. 1, p. 42, Apr. 2022, doi: 10.1038/s41378-022-00375-1.
- [93] F. Zernike, ‘How I Discovered Phase Contrast’, *Science* (1979), vol. 121, no. 3141, pp. 345–349, Mar. 1955, doi: 10.1126/science.121.3141.345.
- [94] C. R. Bagnell, ‘Differential Interference Contrast Microscopy’, *Pathology*, pp. 1–9, 2012.
- [95] J. Wang, W. Zhang, Q. Qi, S. Zheng, and L. Chen, ‘Gradual edge enhancement in spiral phase contrast imaging with fractional vortex filters’, *Sci Rep*, vol. 5, no. 1, p. 15826, Oct. 2015, doi: 10.1038/srep15826.
- [96] S. Banerji, M. Meem, A. Majumder, F. G. Vasquez, B. Sensale-Rodriguez, and R. Menon, ‘Imaging with flat optics: metalenses or diffractive lenses?’, *Optica*, vol. 6, no. 6, p. 805, Jun. 2019, doi: 10.1364/OPTICA.6.000805.
- [97] T. Zhu *et al.*, ‘Plasmonic computing of spatial differentiation’, *Nat Commun*, vol. 8, no. 1, p. 15391, May 2017, doi: 10.1038/ncomms15391.
- [98] T. Zhu *et al.*, ‘Topological optical differentiator’, *Nat Commun*, vol. 12, no. 1, p. 680, Jan. 2021, doi: 10.1038/s41467-021-20972-4.
- [99] Y. Zhang *et al.*, ‘Dielectric Metasurface for Synchronously Spiral Phase Contrast and Bright-Field Imaging’, *Nano Lett*, vol. 23, no. 7, pp. 2991–2997, Apr. 2023, doi: 10.1021/acs.nanolett.3c00388.
- [100] X.-X. Peng, X.-F. Zhu, and J.-L. Zhang, ‘Near Infrared (NIR) imaging: Exploring biologically relevant chemical space for lanthanide complexes’, *J Inorg Biochem*, vol. 209, p. 111118, Aug. 2020, doi: 10.1016/j.jinorgbio.2020.111118.
- [101] Z. Feng *et al.*, ‘Perfecting and extending the near-infrared imaging window’, *Light Sci Appl*, vol. 10, no. 1, p. 197, Sep. 2021, doi: 10.1038/s41377-021-00628-0.

List of References

- [102] D. Lin *et al.*, ‘Reconfigurable structured light generation in a multicore fibre amplifier’, *Nat Commun*, vol. 11, no. 1, p. 3986, Aug. 2020, doi: 10.1038/s41467-020-17809-x.
- [103] D. Wen *et al.*, ‘Broadband Multichannel Cylindrical Vector Beam Generation by a Single Metasurface’, *Laser Photon Rev*, vol. 16, no. 10, Oct. 2022, doi: 10.1002/lpor.202200206.
- [104] G. Li *et al.*, ‘Spin-Enabled Plasmonic Metasurfaces for Manipulating Orbital Angular Momentum of Light’, *Nano Lett*, vol. 13, no. 9, pp. 4148–4151, Sep. 2013, doi: 10.1021/nl401734r.
- [105] H. Li *et al.*, ‘Polarization Detection of Terahertz Waves using All-Silicon Metasurfaces with Tightly Focusing Behavior’, *Laser Photon Rev*, vol. 17, no. 12, Dec. 2023, doi: 10.1002/lpor.202300428.
- [106] J. Liu *et al.*, ‘Generation of arbitrary cylindrical vector vortex beams with cross-polarized modulation’, *Results Phys*, vol. 19, p. 103455, Dec. 2020, doi: 10.1016/j.rinp.2020.103455.
- [107] G. Cao *et al.*, ‘Infrared metasurface-enabled compact polarization nanodevices’, *Materials Today*, vol. 50, pp. 499–515, Nov. 2021, doi: 10.1016/j.mattod.2021.06.014.
- [108] D. Wen and K. B. Crozier, ‘Metasurfaces 2.0: Laser-integrated and with vector field control’, *APL Photonics*, vol. 6, no. 8, p. 080902, Aug. 2021, doi: 10.1063/5.0057904.
- [109] K. Khare, ‘The Angular Spectrum Method’, in *Fourier Optics and Computational Imaging*, Wiley, 2015, pp. 145–151. doi: 10.1002/9781118900352.ch10.
- [110] Y. Miao *et al.*, ‘Tight-focusing properties of propagable fractional-order vector vortex beams’, *Journal of the Optical Society of America B*, vol. 40, no. 5, p. 1113, May 2023, doi: 10.1364/JOSAB.485509.
- [111] X. Zang *et al.*, ‘A Multi-Foci Metalens with Polarization-Rotated Focal Points’, *Laser Photon Rev*, vol. 13, no. 12, Dec. 2019, doi: 10.1002/lpor.201900182.
- [112] S. Gao, C. Park, C. Zhou, S. Lee, and D. Choi, ‘Twofold Polarization-Selective All-Dielectric Trifoci Metalens for Linearly Polarized Visible Light’, *Adv Opt Mater*, vol. 7, no. 21, Nov. 2019, doi: 10.1002/adom.201900883.
- [113] G.-H. Go, C. H. Park, K. Y. Woo, M. Choi, and Y.-H. Cho, ‘Scannable Dual-Focus Metalens with Hybrid Phase’, *Nano Lett*, vol. 23, no. 8, pp. 3152–3158, Apr. 2023, doi: 10.1021/acs.nanolett.2c04696.

List of References

[114] Volodymyr Nechyporuk-Zloy, *Principles of Light Microscopy: From Basic to Advanced*. Cham: Springer International Publishing, 2022. doi: 10.1007/978-3-031-04477-9.

[115] V. Prelog, 'Chirality in Chemistry', *Science* (1979), vol. 193, no. 4247, pp. 17–24, Jul. 1976, doi: 10.1126/science.935852.

[116] R. Corradini, S. Sforza, T. Tedeschi, and R. Marchelli, 'Chirality as a tool in nucleic acid recognition: Principles and relevance in biotechnology and in medicinal chemistry', *Chirality*, vol. 19, no. 4, pp. 269–294, May 2007, doi: 10.1002/chir.20372.

[117] From Wikipedia, 'Chirality', <https://en.wikipedia.org/wiki/Chirality>.

[118] L. A. Nguyen, H. He, and C. Pham-Huy, 'Chiral drugs: an overview.', *Int J Biomed Sci*, vol. 2, no. 2, pp. 85–100, Jun. 2006.

[119] Q. Zhu, Z. Cai, P. Zhou, X. Sun, and J. Xu, 'Recent progress of membrane technology for chiral separation: A comprehensive review', *Sep Purif Technol*, vol. 309, p. 123077, Mar. 2023, doi: 10.1016/j.seppur.2022.123077.

[120] S. Zhang *et al.*, 'Metasurfaces for biomedical applications: imaging and sensing from a nanophotonics perspective', *Nanophotonics*, vol. 10, no. 1, pp. 259–293, Sep. 2020, doi: 10.1515/nanoph-2020-0373.

[121] S.-J. Kim *et al.*, 'Reconfigurable all-dielectric Fano metasurfaces for strong full-space intensity modulation of visible light', *Nanoscale Horiz*, vol. 5, no. 7, pp. 1088–1095, 2020, doi: 10.1039/D0NH00139B.

[122] Q. Yuan *et al.*, 'Recent advanced applications of metasurfaces in multi-dimensions', *Nanophotonics*, vol. 12, no. 13, pp. 2295–2315, Jun. 2023, doi: 10.1515/nanoph-2022-0803.

[123] T. Badloe, J. Seong, and J. Rho, 'Trichannel Spin-Selective Metalenses', *Nano Lett*, vol. 23, no. 15, pp. 6958–6965, Aug. 2023, doi: 10.1021/acs.nanolett.3c01588.

[124] T. Sun, X. Yang, F. Xu, and C. Wang, 'Single chip simultaneous chiral and achiral imaging based on high efficiency 3D plasmonic metalens', *Nanophotonics*, vol. 12, no. 16, pp. 3243–3255, Aug. 2023, doi: 10.1515/nanoph-2023-0142.

[125] Z. Wang *et al.*, 'Bifunctional Manipulation of Terahertz Waves with High-Efficiency Transmissive Dielectric Metasurfaces', *Advanced Science*, vol. 10, no. 4, Feb. 2023, doi: 10.1002/advs.202205499.

[126] T. Wriedt, 'Mie Theory: A Review', 2012, pp. 53–71. doi: 10.1007/978-3-642-28738-1_2.

List of References

- [127] T. A. Nieminen, V. L. Y. Loke, A. B. Stilgoe, N. R. Heckenberg, and H. Rubinsztein-Dunlop, ‘T-matrix method for modelling optical tweezers’, *J Mod Opt*, vol. 58, no. 5–6, pp. 528–544, Mar. 2011, doi: 10.1080/09500340.2010.528565.
- [128] R. C. Gauthier, ‘Computation of the optical trapping force using an FDTD based technique’, *Opt Express*, vol. 13, no. 10, p. 3707, 2005, doi: 10.1364/OPEX.13.003707.
- [129] P. C. Chaumet and C. Billaudeau, ‘Coupled dipole method to compute optical torque: Application to a micropropeller’, *J Appl Phys*, vol. 101, no. 2, Jan. 2007, doi: 10.1063/1.2409490.
- [130] M. A. Yurkin and A. G. Hoekstra, ‘The discrete dipole approximation: An overview and recent developments’, *J Quant Spectrosc Radiat Transf*, vol. 106, no. 1–3, pp. 558–589, Jul. 2007, doi: 10.1016/j.jqsrt.2007.01.034.
- [131] V. L. Y. Loke, T. A. Nieminen, S. J. Parkin, N. R. Heckenberg, and H. Rubinsztein-Dunlop, ‘FDFD/T-matrix hybrid method’, *J Quant Spectrosc Radiat Transf*, vol. 106, no. 1–3, pp. 274–284, Jul. 2007, doi: 10.1016/j.jqsrt.2007.01.040.
- [132] Y. Cao, W. Song, W. Ding, F. Sun, and T. Zhu, ‘Equilibrium orientations of oblate spheroidal particles in single tightly focused Gaussian beams’, *Opt Express*, vol. 22, no. 15, p. 18113, Jul. 2014, doi: 10.1364/OE.22.018113.
- [133] M. Plidschun, H. Ren, J. Kim, R. Förster, S. A. Maier, and M. A. Schmidt, ‘Ultrahigh numerical aperture meta-fibre for flexible optical trapping’, *Light Sci Appl*, vol. 10, no. 1, p. 57, Mar. 2021, doi: 10.1038/s41377-021-00491-z.
- [134] H. Y. Kuo *et al.*, ‘Cubic-Phase Metasurface for Three-Dimensional Optical Manipulation’, *Nanomaterials*, vol. 11, no. 7, p. 1730, Jun. 2021, doi: 10.3390/nano11071730.
- [135] T. Chantakit *et al.*, ‘All-dielectric silicon metasurface for two-dimensional particle manipulation in optical tweezers’, *Photonics Res*, vol. 8, no. 9, p. 1435, Sep. 2020, doi: 10.1364/PRJ.389200.
- [136] T. Li *et al.*, ‘Integrating the optical tweezers and spanner onto an individual single-layer metasurface’, *Photonics Res*, vol. 9, no. 6, p. 1062, Jun. 2021, doi: 10.1364/PRJ.421121.
- [137] M. Mazilu, Y. Arita, T. Vettenburg, J. M. Auñón, E. M. Wright, and K. Dholakia, ‘Orbital-angular-momentum transfer to optically levitated microparticles in vacuum’, *Phys Rev A (Coll Park)*, vol. 94, no. 5, p. 053821, Nov. 2016, doi: 10.1103/PhysRevA.94.053821.

List of References

- [138] A. I. Bishop, T. A. Nieminen, N. R. Heckenberg, and H. Rubinsztein-Dunlop, 'Optical application and measurement of torque on microparticles of isotropic nonabsorbing material', *Phys Rev A (Coll Park)*, vol. 68, no. 3, p. 033802, Sep. 2003, doi: 10.1103/PhysRevA.68.033802.
- [139] M. H. Asadian, S. Askari, and A. M. Shkel, 'An Ultrahigh Vacuum Packaging Process Demonstrating Over 2 Million Q-Factor in MEMS Vibratory Gyroscopes', *IEEE Sens Lett*, vol. 1, no. 6, pp. 1–4, Dec. 2017, doi: 10.1109/LSENS.2017.2762287.
- [140] V. Arrizón and D. Sánchez-de-la-Llave, 'Double-phase holograms implemented with phase-only spatial light modulators: performance evaluation and improvement', *Appl Opt*, vol. 41, no. 17, p. 3436, Jun. 2002, doi: 10.1364/AO.41.003436.

List of References